Two-Dimensional Crystals for Novel Nanoelectronics

Dissertation

zur Erlangung des Doktorgrades

des Fachbereichs Physik

der Universität Hamburg

vorgelegt von
Burkhard Sachs
aus München

Hamburg
2014

Gutachter der Dissertation	Prof. Dr. Alexander Lichtenstein
	Prof. Dr. Mikhail Katsnelson
Gutachter der Disputation	Prof. Dr. Tim Wehling
Datum der Disputation	07.07.2014
Vorsitzender des Prüfungsausschusses	Prof. Dr. Michael Thorwart
Vorsitzende des Promotionsausschusses	Prof. Dr. Daniela Pfannkuche
Dekan des Fachbereichs Physik	Prof. Dr. Heinrich Graener

Abstract

The discovery of graphene and other two-dimensional crystals opens up new perspectives for the performance of future nanoelectronics. Graphene-based nanosystems of atomic thickness reveal unknown physical phenomena and hold out the prospect for a multitude of applications. Recently, research focus has been extended towards other two-dimensional crystals and their combinations into atomically thin heterostructures.

This thesis is devoted to a theoretical investigation of realistic nanoelectronic systems based on two-dimensional crystals. To this end, density functional theory and related techniques are applied to take into account correlation effects such as van der Waals interactions or local Coulomb repulsions. Complemented by effective tight-binding models and continuum mechanics, the electronic and structural properties of graphene/boron nitride heterostructures are in this way comprehensively studied. It turns out that interactions and potentials on multiple length scales coexist in such compounds. Due to lattice mismatch, moiré superstructures are formed, which reduce the spectral band gap. In graphene/molybdenum disulfide hybrids, doping mechanisms can be exploited for photovoltaic applications. By considering realistic disorder effects from impurities to structural distortions, a multifaceted picture of the physics of heterostructures is obtained.

The impact of graphene on the properties of metallic substrates is a further integral part of this thesis. Graphene drastically modifies the surface states of weakly and strongly bound metal substrates. It is demonstrated that metal substrates reduce the visibility of graphene states in scanning tunneling microscopy experiments. In the case of nickel substrates, a spin contrast inversion is induced in the vacuum. Magnetic impurities, such as nickel clusters on graphene, exhibit a characteristic multipeak structure in x-ray absorption spectra, which explains why the magnetization and correlation effects within the clusters are tunable in a controlled manner.

Finally, the feasibility of two-dimensional magnetic materials will be discussed. A material (K_2CuF_4) is proposed which fulfills all criteria for the first-time fabrication and investigation of a truly two-dimensional ferromagnetic crystal. This would not only yield fundamental insights into the physics of magnetic two-dimensional systems, but also facilitate numerous applications, such as spin-polarized electrodes in heterostructures.

Zusammenfassung

Die Entdeckung Graphens und anderer zweidimensionaler Kristalle eröffnet neue Perspektiven für die Leistungsfähigkeit zukünftiger Nanoelektronik. Graphenbasierte Nanosysteme atomarer Dicke bringen unbekannte physikalische Phänomene zu Tage und stellen dank Graphens einzigartigen elektronischen und mechanischen Eigenschaften eine Vielzahl an Anwendungen in Aussicht. In jüngster Zeit sind auch andere zweidimensionale Kristalle und deren Kombinationen in atomar dünnen Heterostrukturen ins Forschungsinteresse gerückt.

Diese Arbeit widmet sich einer theoretischen Untersuchung realistischer nanoelektronischer Systeme, welche auf zweidimensionalen Kristallen basieren. Zu diesem Zweck werden neben Dichtefunktionaltheorie verschiedene (verwandte) Techniken angewandt, um Korrelationseffekte wie van-der-Waals-Wechselwirkungen oder lokale Coulomb-Abstoßungen zu berücksichtigen. Ergänzt durch effektive Tight-Binding-Modelle und Kontinuumsmechanik werden so die strukturellen und elektronischen Eigenschaften von Graphen-Bornitrid-Heterostrukturen umfassend untersucht. Dabei zeigt sich eine Koexistenz an Wechselwirkungen und Potentialen auf unterschiedlichsten Längenskalen. Aufgrund von Gitterfehlanpassung werden Superstrukturen ausgebildet, die die spektrale Bandlücke reduzieren. In Graphen-Molybdändisulfid-Hybriden ermöglichen verschiedene Dotiereffekte eine Photovoltaikanwendung. Durch die Berücksichtigung realistischer Unordnungseffekte von Störstellen bis Gitterverzerrungen ergibt sich ein facettenreiches Bild der Physik in Heterostrukturen.

Der Einfluss von Graphen auf die Eigenschaften metallischer Substrate ist ein weiterer Bestandteil dieser Untersuchung. Graphen modifiziert sowohl auf schwach als auch auf stark bindenden Metallsubstraten deren Oberflächenzustände drastisch. Außerdem wird gezeigt, dass Metallsubstrate die Sichtbarkeit von Graphen-Zuständen in Rastertunnelmikroskopie-Experimenten reduzieren. Im Falle von Nickel-Substraten wird eine Spinkontrastumkehr im Vakuum erzeugt. Magnetische Störstellen, wie z.B. Nickel-Cluster auf Graphen, weisen charakteristische Spitzen in Röntgenabsorptionsspektren auf, die erklären, warum magnetische Momente und Korrelationseffekte in den Clustern kontrolliert manipuliert werden können.

Abschließend wird die Möglichkeit zur Realisierung von magnetischen zweidimensionalen Materialien diskutiert. Es wird ein Material (K_2CuF_4) vorgeschlagen, das alle Eigenschaften aufweist, um zum ersten Mal einen wirklich zweidimensionalen ferromagnetischen Kristall herzustellen und zu untersuchen. Dadurch ergäben sich nicht nur fundamentale Einsichten in die Physik magnetischer zweidimensionaler Systeme, sondern auch zahlreiche Anwendungen, beispielsweise als spin-polarisierte Elektroden in Heterostrukturen.

Contents

1

Introduction

The continuous miniaturization of electronic devices within the past five decades has great impact on everyday life. To date, the industrial fabrication of even smaller, yet faster devices has been advancing on the basis of silicon transistors. The limits, however, of silicon devices, technologically and fundamentally [1], will inevitably be reached in the foreseeable future, which calls for essential changes in the development of next-generation electronics. Progress in this field can be achieved in unimaginably many ways, from the integration of new materials into existing electrical devices up to the design of entirely novel architectures on the nanoscale.

As a consequence of electric device miniaturization below the millimeter scale, nanomaterials[1] have gained in importance. Therefore, it is not surprising that the 2004 discovery of graphene [2], the thinnest possible material with exceptional properties, gave rise to a new "gold rush" in condensed matter research. Graphene, an atomically thin carbon layer, and many other two-dimensional atomic crystals [3], which were reported shortly after, might herald a new era for nanoelectronics. Huge efforts were taken by experimentalists and theorists to explore graphene's intrinsic properties in the past decade, and, according to graphene discoverer A. Geim, "most of the low-hanging graphene fruits have already been harvested" [4]. Indeed, to exploit the technological potential of graphene and other two-dimensional materials, the next big step is to create the conditions suitable for the fabrication of novel electronic devices, such as transistors or photovoltaic cells, and to develop nanostructures with the goal to push the

[1] Materials between 10^{-6} and 10^{-9}m in size

current performance limits. The development of nanodevices with novel 2D materials makes high demands on theoretical physicists: material-specific studies on multiple length scales, unusual quantum phenomena to deal with, and predictions of useful material combinations.

In fact, research focus has already started to go beyond graphene as a consequence of tremendous experimental progress in sample preparation. Besides the nowadays possible growth of graphene on an industrial scale [5, 6], a turning point came in 2011 with the first reports on heterostructures constituted solely by 2D crystals [4]. This initiated wide research interest in 2D crystals beyond graphene and in 2D-based heterostructures, with some seminal achievements within just few years, such as graphene-based tunneling transistors [7] and photovoltaic devices [8]. Importantly, the experimental progress led to a drastic improvement of the quality of graphene samples. As a result of ultra-high quality, some intrinsic properties of graphene arising from many-body effects can now be observed in experiments, which led to renewed efforts to study the complex many-body behavior of graphene electrons. Therefore, the recent development gives 2D crystals and their combinations remarkable prospects for novel applications, and, simultaneously, turns these materials into exciting playgrounds to discover unknown phenomena and to study fundamental properties of 2D electron systems.

The goal of this thesis is a theoretical investigation of realistic nanoelectronic systems based on two-dimensional crystals, with an emphasis on the word "realistic". This does not only comprise calculations of intrinsic material properties. Moreover, realistic nanostructures are subject to environmental effects, such as substrates, defects and strains, for which different techniques will be connected with first-principles density functional theory. In this way, phenomena on various length and energy scales can be captured, from classical continuum theory on the mesoscale, over van der Waals interactions up to strong local correlations in impurities. The considered nanosystems range from graphene/metal interfaces and impurity-contaminated graphene over 2D-based heterostructures to a prediction of a magnetic 2D crystal.

The thesis is organized as follows: In chapter 2, a brief methodical overview will be given, with an emphasis on density functional theory and extensions, such as van der Waals methods and techniques for the treatment of strong Coulomb interactions. Chapter 3 will be a short review on 2D crystal properties with a special focus on graphene, which is the most frequently investigated material in

this thesis.

In the main part, beginning with chapter 4, two different graphene heterostructures will be discussed in detail: graphene/boron nitride and graphene/MoS_2 hybrids. For the first system, the intricate consequences of moiré superstructures for graphene's electrons will be discussed. In order to judge stability properties of these systems, an accurate treatment of van der Waals interactions is required, which will be the basis of elasticity calculations. At the same time, physics on scales above 10 nm require usage of tight-binding models, which will be employed as well. Based on this setup, in addition defects in graphene/boron nitride interfaces will be investigated.

The same chapter will furthermore address applications and properties of graphene/MoS_2 interfaces in a joint experimental and theoretical investigation. The impact of MoS_2 edges on graphene's electrons will be illuminated as well as impurity effects. Importantly, the investigated device has an application as a photodetector.

Interfaces between graphene and metal surfaces will be studied in chapter 5. For graphene on magnetic Ni(111) and non-magnetic Ir(111), considerable modifications of the surface properties upon graphene adsorption will be revealed. A detailed study of graphene states in local probe scanning tunneling microscopy (STM) experiments will be presented as well. It turns out that STM spectra of graphene on metals require a careful interpretation due to invisibility of graphene states in the vacuum. Local probe experiments are also the topic of chapter 6, where Ni adatoms and clusters on graphene will be investigated. Simulations of x-ray absorption spectra (XAS) will be carried out to analyze the magnetic and electronic configurations of Ni clusters on graphene. It will be demonstrated that magnetism and correlations are tunable in these clusters and depend on the cluster size.

Finally, a prediction will be made about magnetism in 2D crystals (chapter 7). Ferromagnetism in 2D crystals has not been achieved so far. The motivation of this chapter is to demonstrate the feasibility of 2D magnetic crystals with the example of the perovskite material K_2CuF_4. It will be reasoned why 2D K_2CuF_4 fulfills all criteria to produce a 2D magnetic crystal: the bulk material exhibits sufficiently low cleavage energies, which enables exfoliation down to the monolayer. Also, the chemical stability of 2D K_2CuF_4 will be shown to be sufficient. The ferromagnetic coupling is high within the layer, with the consequence of a

ferromagnetic ordering below 8 K. This seems to be in contrast to the Mermin-Wagner theorem; however, the magnetic transition observable in 2D K_2CuF_4 is not a second order transition, but a quasi-long range ordering effect due to the so-called Kosterlitz-Thouless transition. Therefore, the material offers, besides many possible applications in heterostructures, a promising way to study for the first time a truly 2D magnetic system in experiments. The exciting prospects of magnetic 2D crystals and the consequences of the Kosterlitz-Thouless transition will be discussed as well.

List of publications

Some of the results in chapters 4 - 7 have previously been published as articles in scientific journals. In many cases, figures shown in these chapters have been copied from the original publications listed below. However, all chapters have been rewritten and elaborate in detail the results, computational details, and their interpretation. Therefore, all chapters can be understood without further reading the papers of the following list.

- B. Sachs, L. Britnell, T. O. Wehling, A. Eckmann, R. Jalil, B. D. Belle, A. I. Lichtenstein, M. I. Katsnelson, and K. S. Novoselov. *Doping mechanisms in graphene-MoS_2 hybrids*, Appl. Phys. Lett. **103**, 251607 (2013)
- B. Sachs, T. O. Wehling, K. S. Novoselov, A. I. Lichtenstein, and M. I. Katsnelson. *Ferromagnetic two-dimensional crystals: Single layers of K_2CuF_4*, Phys. Rev. B (Rapid Comm.) **88**, 201402(R) (2013)
- T. Eelbo, M. Wasniowska, P. Thakur, M. Gyamfi, B. Sachs, T. O. Wehling, S. Forti, U. Starke, C. Tieg, A. I. Lichtenstein, and R. Wiesendanger. *Adatoms and Clusters of 3d Transition Metals on Graphene: Electronic and Magnetic Configurations*, Phys. Rev. Lett. **110**, 136804 (2013)
- S. J. Altenburg, J. Kröger, T. O. Wehling, B. Sachs, A. I. Lichtenstein, and R. Berndt. *Local Gating of an Ir(111) Surface Resonance by Graphene Islands*, Phys. Rev. Lett. **108**, 206805 (2012)
- L. V. Dzemiantsova, M. Karolak, F. Lofink, A. Kubetzka, B. Sachs, K. von Bergmann, S. Hankemeier, T. O. Wehling, R. Frömter, H. P. Oepen, A. I. Lichtenstein, and R. Wiesendanger. *Multiscale magnetic study of Ni(111) and graphene on Ni(111)*, Phys. Rev. B **84**, 205431 (2011)
- B. Sachs, T. O. Wehling, M. I. Katsnelson, and A. I. Lichtenstein. *Adhesion and electronic structure of graphene on hexagonal boron nitride substrates*, Phys. Rev. B **84**, 195414 (2011)
- B. Sachs, T. O. Wehling, A. I. Lichtenstein, and M. I. Katsnelson. Chapter in *Physics and Applications of Graphene - Theory* (InTech, 2011)

2

Electronic structure for real materials

2.1 Fundamentals

Before we dwell on different concepts for electronic structure calculations, we briefly revise the underlying basic formulation of the quantum many-body problem in solid state physics. The derivations given throughout this chapter follow (if not marked otherwise) the books of Fulde [9], Martin [10], Parr & Yang [11], Pavarini *et al.* [12] and the review article by Jones and Gunnarsson [13]. The fundamental equation of quantum systems in the non-relativistic limit is the Schrödinger equation [14]

$$i\hbar\frac{\partial}{\partial t}\Psi = H\Psi, \tag{2.1}$$

where $\hbar$ is the Planck constant, H the Hamiltonian and $\Psi = \Psi(\vec{r}_1, \vec{r}_2, ..., \vec{r}_{N_{tot}}, t)$ the full many-body quantum wave function of N_{tot} particles as a function of all particle positions $\vec{r}_i$ and the time t (the spin is included in the index i). Our theoretical understanding of electronic states in matter, thus, atoms, molecules, and solids is commonly based upon solutions of this equation, and the particles involved in these problems comprise nuclei (protons and neutrons) and electrons. The kinetic part T of the Hamiltonian

$$H = T + V \tag{2.2}$$

is defined as

$$T = -\frac{1}{2}\sum_i \vec{\nabla}_i^2 - \frac{1}{2}\sum_i \frac{\vec{\nabla}_I^2}{M_I}, \tag{2.3}$$

which is the sum of the kinetic energy terms of electrons i at positions $\vec{r}_i$ and nuclei I at positions $\vec{R}_I$ (we will use in the following Hartree atomic units $\hbar = m_e = e = 4\pi/\epsilon_0 = 1$). $M_I \approx 1836$ is the nuclei mass. The second part of the Hamiltonian, the total potential acting on all particles, is composed of three parts, namely the nucleus-nucleus repulsion $V_{\text{nuc}-\text{nuc}}$, the electron-nuclei interaction $V_{\text{nuc}-\text{e}}$ and the electron-electron repulsion $V_{\text{e}-\text{e}}$:

$$V = V_{\text{nuc}-\text{nuc}} + V_{\text{nuc}-\text{e}} + V_{\text{e}-\text{e}} = \frac{1}{2}\sum_{I\neq J}\frac{Z_I Z_J}{|\vec{R}_I - \vec{R}_J|} - \sum_{I,j}\frac{Z_I}{|\vec{R}_I - \vec{r}_j|} + \frac{1}{2}\sum_{i\neq j}\frac{1}{|\vec{r}_i - \vec{r}_j|}. \tag{2.4}$$

Thus, in contrast to high-energy physics, for any system the fundamental Hamiltonian is well-known; the remaining challenge for realistic systems is however the solution of the resulting many-body problem. In the Hamiltonian, it is the potential term of Eq. 2.4 that in general renders invalid a wave function representation in terms of Slater determinants. Despite the simplicity of the Hamiltonian, the resulting many-body problem is impossible to solve exactly for the overwhelming majority of realistic solids, molecules and even atoms, since the Hilbert space dimension grows exponentially. Only systems with a few particles are possible to compute exactly using "brute force" methods. In order to achieve a satisfying description of materials, further approximations have to be applied in the solution of Eq. 2.1, and we present in the following some suitable techniques for the efficient computation of material properties.

First, the many-body problem can be simplified by restricting to ground state properties in the calculations. For the Hamiltonian 2.2, the eigenstates of Eq. 2.1 can be rewritten in terms of stationary solutions as $\Psi(\vec{r}_1, \vec{r}_2, ..., \vec{r}_{N_{tot}}, t) = \Psi(\vec{r}_1, \vec{r}_2, ..., \vec{r}_{N_{tot}}) \exp^{-i(E/\hbar)t}$, and the ground state of the system is the lowest-energy solution of the time-independent Schrödinger equation [10]:

$$H\,|\Psi\rangle = E\,|\Psi\rangle\,, \tag{2.5}$$

with $|\Psi\rangle$ the wavevector in Hilbert space (in bra-ket notation) and E the energy eigenvalues of the Hamiltonian. This equation is frequently the starting point for material simulations referred to as "electronic structure" calculations.

The tremendous efforts needed to solve Eq. 2.5 can be reduced by assessing the role of individual terms in the Hamiltonian 2.2. One can see easily that the second term of the kinetic part 2.3, which describes the kinetic energy of nuclei, is small compared to the electronic term due to the factor $1/M_I$. In the

Hamiltonian, this allows for a perturbation expansion around the small nuclear kinetic term, and, based on this, effects such as electron-phonon coupling can be effectively taken into account. For instance, electron-phonon interactions can be of particular importance for the understanding of superconductivity in BCS theory, or electron transport in metals [10]. For many systems, however, electron-phonon coupling is small and we can apply the Born-Oppenheimer approximation [15], which assumes that electrons rearrange quasi-instantaneously around the ions, or, in other words, cores are considered as frozen. Technically, the kinetic energy of nuclei is set to zero ($M_I \to \infty$) in the Hamiltonian and the full wave function can be rewritten as a product of the electron and core wave function. In the end, one considers a Hamiltonian restricted to electrons in an environment of frozen ions,

$$H = -\frac{1}{2}\sum_i \vec{\nabla}_i^2 - \sum_{I,j} \frac{Z_I}{|\vec{R}_I - \vec{r}_j|} + \frac{1}{2}\sum_{i \neq j} \frac{1}{|\vec{r}_i - \vec{r}_j|}, \tag{2.6}$$

with eigenenergies E dependent on the positions of the nuclei. The Hamiltonian 2.6 usually defines the central problem to solve in electronic structure theory. Note that the Born-Oppenheimer approximation still allows taking interaction between nuclei into account: in a second step, one can finally compute the total energy of the system as $E_{\text{tot}} = E + E_I$, with E_I the classical interaction of ions.

Despite the alleviation through the Born-Oppenheimer approximation, the Hamiltonian 2.6 is still by far too difficult to diagonalize exactly for any real material of interest.

2.2 Density functional theory

An efficient scheme for the solution of the electron problem is the density functional theory (DFT), which has become the work horse of computational condensed matter theory. In the following, some foundations and basics of DFT will be presented. Before discussing commonly used implementations of density functional theory, it is instructive to review the historical development of this method, beginning with the pioneering work of Thomas [16] and Fermi [17] from the 1920's. In their independent works, Thomas and Fermi developed a concept for calculations of ground state properties of atoms without incorporating the full many-body wave function of the Hamiltonian 2.6. Typical ground state

properties of atoms, molecules and solids comprise equilibrium positions of atoms, magnetic moments, and total energies, for instance. Instead of calculating the wave function, Thomas-Fermi theory is a variational method for calculating the ground state electron density $\rho(\vec{r})$. It is based on the minimization of an energy, which is written as a functional of $\rho(\vec{r})$ as

$$\begin{aligned} E_{\mathrm{TF}}[\rho] = C_{\mathrm{F}} \int \rho^{5/3}(\vec{r}) d^3r + \int d^3r V_{\mathrm{ext}}(\vec{r})\rho(\vec{r}) \\ + \frac{1}{2}\int d^3r \rho(\vec{r}) V_{\mathrm{H}} + C_x \int d^3r \rho(\vec{r})^{4/3}. \end{aligned} \tag{2.7}$$

The first term with $C_{\mathrm{F}} = \frac{3}{10}(3\pi^2)^{2/3}$ denotes the kinetic energy part and can be derived from the kinetic energy of a classical homogeneous electron gas, where the space-dependent Fermi momentum is given by

$$k_{\mathrm{F}}(\rho) = (3\pi^2\rho)^{1/3}, \tag{2.8}$$

and, as a consequence, the local kinetic energy follows

$$T \sim k_{\mathrm{F}}^5. \tag{2.9}$$

Hence, the kinetic energy of the actually inhomogeneous atom is approximated by a quasi-classical expression for a uniform system of particles. This is one major drawback of the Thomas-Fermi method compared to DFT, where the kinetic energy of an auxiliary system is treated exactly. Obviously, this local approximation works well only in case of a smooth spatial variation of $\rho(\vec{r})$. The idea behind, however, that an electronic quantity is expressed by a density functional with local relations of the homogeneous particle system, constitutes the fundament of modern DFT and will be discussed again in this chapter.

The second term in Eq. 2.7 incorporates the nuclei-electron interaction classically via $V_{\mathrm{ext}} = \sum_I -\frac{Z_I}{r}$ (without any other external perturbation), and the third term is an approximative expression for the electron-electron repulsion, the classical Hartree energy, which determines the density ρ in the potential of all other electrons. The Hartree potential reads as

$$V_{\mathrm{H}}(\vec{r}) = \int d^3r' \frac{\rho(\vec{r}')}{|\vec{r} - \vec{r}'|} \tag{2.10}$$

and can be directly derived from the solution of the Poisson equation $\nabla^2 V_{\mathrm{H}}(\vec{r}) = -4\pi\rho(\vec{r})$. The fourth term in Eq. 2.7 was not present in the original Thomas-Fermi theory, but later complemented by Dirac [18] and captures an additional local exchange interaction in the atom in the unpolarized case ($C_x = -\frac{3}{4}(\frac{3}{\pi})^{1/3}$).

The ground state density $\rho_0(\vec{r})$ is now obtained via variation of the functional 2.7,

$$\delta \left\{ E_{\mathrm{TF}}[\rho] - \mu_{\mathrm{TF}} \left(\int d^3 r \rho(\vec{r}) - N \right) \right\} = 0, \tag{2.11}$$

whereby the Fermi energy μ_{TF} plays the role of a Lagrange multiplier, and N originates from the constraint that the particle number remains fixed:

$$\int d^3 r \rho(\vec{r}) = N. \tag{2.12}$$

Finally, introducing the total potential $V(\vec{r}) = V_{ext}(\vec{r}) + V_H(\vec{r}) + C_x \rho(\vec{r})^{4/3}$, we end up with an Euler-Lagrange equation

$$\frac{1}{2}(3\pi^2)^{(2/3)} \rho(\vec{r})^{2/3} + V(\vec{r}) - \mu_{\mathrm{TF}} = 0. \tag{2.13}$$

Two major shortcomings are responsible for the failure of Thomas-Fermi theory in calculations of real materials: First, as mentioned above, the approximative treatment of the kinetic energy, which breaks down in inhomogeneous atoms and molecules, and furthermore, the insufficient inclusion of correlation effects despite the local exchange correction of Dirac, which is still in use today in modern DFT.

However, conceptually, Thomas-Fermi theory comes close to DFT: The problem of calculating the ground-state wave function is avoided by reformulating the problem in terms of the electron density, and a local approximation is used for the unknown kinetic energy functional. In this fashion, the problem of computing a wave function with $3N$ degrees of freedom is now, remarkably, reduced to the calculation of the density $\rho(\vec{r})$, which depends on only 3 spatial coordinates.

2.3 Ground states from density functionals

Thomas-Fermi theory, the predecessor of DFT, is an approximative method to compute the ground state density. Modern DFT is established by the seminal work of Hohenberg and Kohn [19], who proved that the many-body problem can be reformulated in an *exact* theory in terms of density functionals. Later, Levy and Lieb found a general search formulation for the ground state density [20, 21].

Hohenberg and Kohn derived two theorems that establish a one-to-one correspondence between the ground-state density and the ground-state wave function and argued that all ground state properties may be considered as functionals of

the basic variable, the density. Their theorems apply for any system of interacting particles in an external potential $v(\vec{r})$ which includes nuclei-electron interaction, but is generally unknown:

$$H = T + V + V_{e-e} = -\frac{1}{2}\sum_i \nabla_i^2 + \sum_i v(\vec{r}_i) + \frac{1}{2}\sum_{i \neq j} \frac{1}{|\vec{r}_i - \vec{r}_j|}. \tag{2.14}$$

In short, the first Hohenberg-Kohn theorem states that the external potential v in the Hamiltonian is uniquely determined by the ground state density $\rho_0(\vec{r})$. This allows rewriting the ground state energy, which is a functional of ρ and v, as

$$E_v[\rho] = \langle \Psi | H | \Psi \rangle = \int \rho(\vec{r}) v(\vec{r}) d^3r + F[\rho], \tag{2.15}$$

where

$$F[\rho] = T[\rho] + V_{\mathrm{e-e}} \tag{2.16}$$

is a universal functional of ρ and independent of the external potential. It contains the density functionals of the kinetic energy $T[\rho]$, and the electron interaction $V_{\mathrm{e-e}}$ of a so far unknown form. A definition of this term will be given later.

The second Hohenberg-Kohn theorem ensures the energy variation principle, meaning that the minimum of $E_v[\rho]$ is given by the ground state density $\rho_0(\vec{r})$:

$$E_v[\rho] \geq E_v[\rho_0]. \tag{2.17}$$

Both theorems can easily be proven (see, e.g., [10, 11]). Practically, however, one gets into difficulties with the implementation of the variation principle. The energy functional $E_v[\rho]$, and in particular the universal functional $F[\rho]$, are only defined in terms of particle densities associated with the wave function of Hamiltonian 2.14, including some external potential v of any form. In this case, ρ is named *v-representable* and the validity of the Hohenberg-Kohn theorem is restricted to *v-representable* densities. This means, in practice, that only *v-representable* trial densities are applicable, but the conditions for *v-representability* are unknown. Even examples of single-particle densities were found [22] that cannot be associated with states of Hamiltonian 2.14.

This problem was solved by the aforementioned Levy and Lieb [20, 21], who proved both theorems without restriction to a *v-representable* density and developed a method to calculate the ground state wave function from a given density. While the density is easily calculated as the square of the wave function, the

inverse search for Ψ is less simple. This problem is solved by reformulating the density functional theory such that the theorems are also valid in terms of *N-representability*, which is a weaker condition. *N-representable* densities are all densities obtained from anti-symmetric wave functions, fulfilling the mathematical conditions [11]

$$\rho(\vec{r}) \geq 0, \quad \int \rho(\vec{r}) d^3r = N, \quad \int |\vec{\nabla}\rho(\vec{r})^{1/2}|^2 d^3r < \infty. \tag{2.18}$$

Now, it is necessary to distinguish the true ground state wave function Ψ_0 from all other wave functions Ψ_{ρ_0}, which reproduce the same density as Ψ_0, but do not represent the ground state of the system. This is achieved by making use of the minimum-energy principle

$$\langle \Psi_{\rho_0} | H | \Psi_{\rho_0} \rangle \geq \langle \Psi_0 | H | \Psi_0 \rangle = E_0, \tag{2.19}$$

which can be rewritten as

$$\langle \Psi_{\rho_0} | T + V_{e-e} | \Psi_{\rho_0} \rangle + \int v(\vec{r}) \rho_0(\vec{r}) d^3r \geq \langle \Psi_0 | T + V_{e-e} | \Psi_0 \rangle + \int v(\vec{r}) \rho_0(\vec{r}) d^3r. \tag{2.20}$$

It follows directly that

$$\langle \Psi_{\rho_0} | T + V_{e-e} | \Psi_{\rho_0} \rangle \geq \langle \Psi_0 | T + V_{e-e} | \Psi_0 \rangle . \tag{2.21}$$

Thus, the ground state wave function minimizes the energy, which also proves the Hohenberg-Kohn theorem for *N-representable* densities, since the right term of the above equation can be identified with the functional $F[\rho]$ (Eq. 2.15). Stated differently, this reveals a constrained-search definition,

$$F[\rho_0] = \langle \Psi_0 | T + V_{e-e} | \Psi_0 \rangle = \min_{\Psi \to \rho_0} \langle \Psi | T + V_{\mathrm{e-e}} | \Psi \rangle , \tag{2.22}$$

meaning that the minimum of the functional $F[\rho]$ is found by varying over all wave functions associated with the *N-representable* input density ρ_0. Practically, the ground state energy is then determined in a second step as a variation over all trial densities:

$$E_0 = \min_{\rho} \left\{ \min_{\Psi \to \rho_0} \left[\langle \Psi | T + V_{\mathrm{e-e}} | \Psi \rangle + \int v(\vec{r}) \rho(\vec{r}) d^3r \right] \right\} . \tag{2.23}$$

This constrained-search formulation can be generalized in a way that allows determining equilibrium states in statistical ensembles considering finite temperatures.

2.4 Kohn-Sham formalism

So far, we have shown that the many-electron problem can be dramatically reduced by introducing a universal energy functional of the density (Eq. 2.15), which becomes minimal for the ground state density ρ_0. Then, Thomas-Fermi theory might be applied to calculate the ground state by varying this functional with respect to the density. However, this incorporates the deficiencies of strong approximations on the kinetic energy, which eventually lead to a failure of the method for molecules and solids. In contrast, the constrained-search formulation of the last section justifies the viability of density functional theory and offers in principle a way to find the ground state by variation of all wave functions that reproduce the same density. However, practically, how should one choose the kinetic energy term $T[\rho]$ and the interaction $V_{\mathrm{e-e}}$? This question was ingeniously answered by Kohn and Sham [23], who introduced an auxiliary system of non-interacting particles to the problem, which allows in principle for an exact theory of the ground state.

The Kohn-Sham (KS) auxiliary system is a reference system of independent particles in a so far undefined external potential. In this system, electrons do not interact with each other, which allows for an easy evaluation of the kinetic energy as

$$T_s[\rho] = \sum_i^N \langle\psi_i| - \frac{1}{2}\nabla^2|\psi_i\rangle\,, \tag{2.24}$$

with ψ_i the orbital of the i-th particle in the auxiliary system. In this special case of non-interacting particles, the ground-state wave function has determinantal character and the density can be calculated as

$$\rho_s(\vec{r}) = \sum_i^N |\psi_i(\vec{r})|^2. \tag{2.25}$$

Thus, the system consists of N orbitals with a filling of one electron in each orbital. The wave function determinant reads as

$$\Psi_s = \frac{1}{\sqrt{N!}} \det[\psi_1\psi_2 \ldots \psi_N]\,. \tag{2.26}$$

Having introduced the auxiliary system, it must still be connected with the energy functional $F[\rho]$ (2.16), as it is defined by the Hohenberg-Kohn theorem. The exactly evaluable kinetic energy of the auxiliary system 2.24 is not equal to the

kinetic energy of the interacting system. Therefore, we introduce an exchange-correlation potential

$$E_{\mathrm{xc}}\left[\rho\right] = T\left[\rho\right] - T_s\left[\rho\right] + V_{\mathrm{e-e}}\left[\rho\right] - V_{\mathrm{H}}\left[\rho\right], \tag{2.27}$$

with the first two terms being the kinetic energy difference between the auxiliary and the "true" system, and the last two terms the general electron-electron interaction reduced by the classical electron repulsion, the Hartree energy

$$V_{\mathrm{H}}\left[\rho\right] = \frac{1}{2}\int d^3r d^3r' \frac{\rho(\vec{r})\rho(\vec{r}')}{|\vec{r}-\vec{r}'|}, \tag{2.28}$$

which is equivalent to the third term in the Thomas-Fermi energy 2.7. In this fashion, the functional applied to Levy's constrained-search formalism (Eq. 2.15) can be rewritten as

$$F\left[\rho\right] = T_s\left[\rho\right] + V_{\mathrm{H}}\left[\rho\right] + E_{\mathrm{xc}}\left[\rho\right]. \tag{2.29}$$

Only the exchange-correlation functional E_{xc} is undetermined here and must be, as will be shown later, suitably approximated. Applying the variational principle to the total energy

$$E\left[\rho\right] = V_{\mathrm{ext}}\left[\rho\right] + F\left[\rho\right] = \int \rho(\vec{r}) v_{\mathrm{ext}}(\vec{r}) d^3r + F\left[\rho\right] \tag{2.30}$$

leads to

$$\frac{\delta E\left[\rho\right]}{\delta\rho(\vec{r})} = v_{\mathrm{ext}} + \frac{\delta T_s\left[\rho\right]}{\delta\rho(\vec{r})} + \frac{\delta V_{\mathrm{H}}\left[\rho\right]}{\delta\rho(\vec{r})} + \frac{\delta E_{\mathrm{xc}}\left[\rho\right]}{\delta\rho(\vec{r})} = \mu, \tag{2.31}$$

with the Lagrange multiplier μ originating from the constraint of a fixed particle number ($\int \rho(\vec{r}) d^3r = N$). We introduce the exchange correlation potential and the Hartree potential,

$$v_{\mathrm{xc}} = \frac{\delta E_{\mathrm{xc}}\left[\rho\right]}{\delta\rho(\vec{r})}, \qquad v_{\mathrm{H}} = \frac{\delta V_{\mathrm{H}}\left[\rho\right]}{\delta\rho(\vec{r})} = \int \frac{\rho(\vec{r}')}{|\vec{r}-\vec{r}'|} d^3r', \tag{2.32}$$

and finally merge the potential terms into an effective potential

$$v_{\mathrm{KS}}(\vec{r}) = v_{\mathrm{ext}}(\vec{r}) + v_{\mathrm{H}}(\vec{r}) + v_{\mathrm{xc}}(\vec{r}). \tag{2.33}$$

Thus, we obtain in the end N Schrödinger equations for N non-interacting particles

$$\left[-\frac{1}{2}\nabla^2 + v_{\mathrm{eff}}(\vec{r})\right]\psi_i = \epsilon_i \psi_i, \tag{2.34}$$

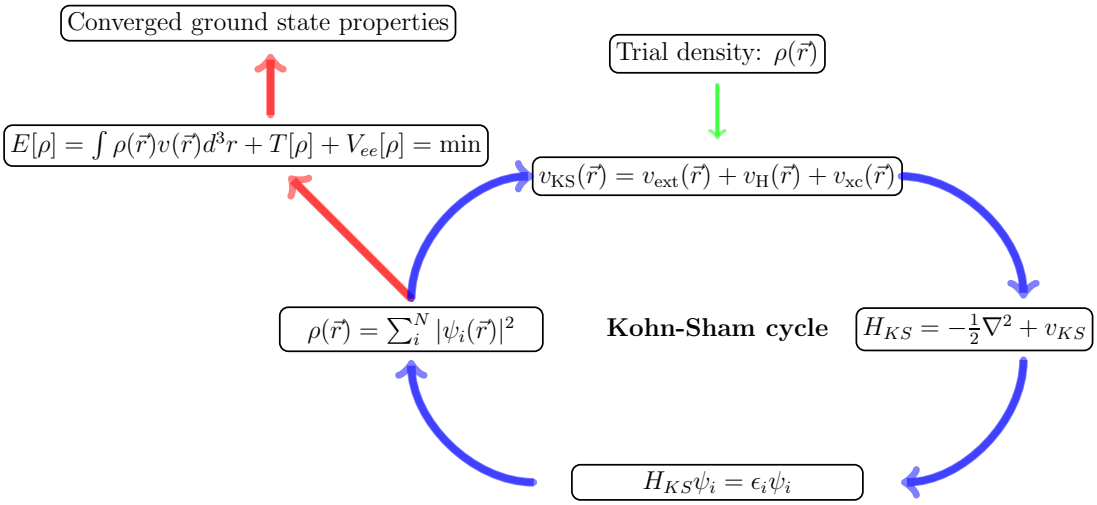

Figure 2.1: Scheme of the Kohn-Sham cycle. A trial density $\rho(\vec{r})$ is used to calculate the *effective* Kohn-Sham potential v_{KS}, and the calculation procedure is repeated (blue arrows) until the density, which minimizes the total energy, is found (red arrows).

which are exact, although now in a Hartree form. This allows for a very efficient numerical treatment of the problem. After solution of Eq. 2.34, one can recalculate the density of the auxiliary system according to Eq. 2.25, which is equal to the density of the interacting system, as long as all potential terms in Eq. 2.33 are well-known. To determine the effective potential v_{KS}, again a density is required, and therefore, the problem is treated self-consistently by repeated solution of Eqs. 2.33, 2.34 and 2.25. This is illustrated in Fig. 2.1. The only quantity that has to be approximated is the exchange-correlation potential, whose contribution to the total energy is rather small. If it is approximated in a local form, the entire effective potential becomes local, and the numerical efforts required to solve Eq. 2.34 are the same as for a Hartree system. The theory can be generalized to account for spin-polarized systems w.l.o.g.

2.5 Local approximations to the exchange-correlation potential

The lack of an exact exchange-correlation functional triggered huge research efforts in the past decades. In their original work, Kohn and Sham [23] casually delivered an approximation to the exchange correlation functional, which is today

widely used and, albeit simple, surprisingly well-performing. It basically follows the concept of employing properties of the homogeneous electron gas to the energy functional, which we presented for Thomas-Fermi theory (Sec. 2.2). Here, however, it will be applied to the exchange-correlation potential instead of the kinetic energy, now expressed as

$$E_{\mathrm{xc}}\left[\rho\right] = \int \rho(\vec{r})\epsilon_{\mathrm{xc}}\left[\rho\right] d^3r, \tag{2.35}$$

with ϵ_{xc} the exchange-correlation energy per particle in a homogeneous gas of particles with density $\rho(\vec{r})$. This functional is not uniquely defined, but its physical motivation can be deduced from the concept of the exchange-correlation hole and the adiabatic connection, which we discuss in Sec. 2.7.1. In the case of an uncorrelated system (independent-particle approximation), only exchange energy enters in ϵ_{xc}, which can be approximated in a local, analytical form:

$$\epsilon_{\mathrm{x}}(\rho) = -\frac{3}{4}\left(\frac{3}{\pi}\right)^{1/3} \rho(\vec{r})^{1/3}. \tag{2.36}$$

Applied in this non-interacting limit, the method equals (up to a constant factor of $\alpha = 2/3$ in 2.36) the so-called X_α method, which is a method for determining Hartree-Fock eigenstates in inhomogeneous electron systems [24] by a local approximation to the exchange energy. For further processing, Eq. 2.36 is used to calculate the exchange-correlation potential

$$v_{\mathrm{xc}}^{\mathrm{LDA}}(\vec{r}) = \frac{\delta E_{\mathrm{xc}}^{LDA}}{\delta\rho(\vec{r})} = \epsilon_{\mathrm{xc}}\left[\rho\right] + \rho(\vec{r})\frac{\delta\epsilon_{\mathrm{xc}}^{\mathrm{LDA}}}{\delta\rho}, \tag{2.37}$$

which in the non-interacting system becomes

$$v_{\mathrm{x}}^{\mathrm{LDA}}(\vec{r}) = -\left(\frac{3}{\pi}\rho(\vec{r})\right)^{1/3}. \tag{2.38}$$

The more convenient form

$$\epsilon_{\mathrm{xc}}\left[\rho\right] = \epsilon_{\mathrm{x}}\left[\rho\right] + \epsilon_{\mathrm{c}}\left[\rho\right] \tag{2.39}$$

takes correlation of particles into account. The correlation part in the local density approximation (LDA) cannot be analytically evaluated, but is has been precisely determined using quantum Monte Carlo (QMC) techniques [25] and interpolation [26]. The approximation to the exchange-correlation energy by means

of the homogeneous electron gas completes the Kohn-Sham cycle from a technical point of view. It is clear how all terms in the Kohn-Sham equation have to be evaluated, and the only approximation required for determination of the ground state is absorbed in the exchange-correlation part of the total energy.

The LDA offers a high-quality description of solids, but naturally runs into difficulties with strongly correlated systems. Typical examples are, for instance, transition metal oxides and a long list of perovskite materials. Another deficiency of the LDA is the low performance in chemical applications. Mostly, LDA overestimates bonding energies dramatically (on the order of 1 eV), which makes it difficult to obtain energetics of molecule formation in chemistry. Ionization potentials are also not reproduced in LDA. Due to all these deficiencies, many exchange-correlation functionals have been developed to this date. Some of them rely on the original LDA, such as the local spin density approximation (LSDA), which includes spin-polarization and is superior to LDA. An instructive overview over all functionals is the "Jacob's ladder" [27], which depicts the development of the "zoo" of density functionals, including different flavors and parametrizations.

A first step upwards in Jacob's ladder and a natural extension of the LDA is a less local form of the exchange-correlation functional. A today widely used semi-local approximation is the generalized gradient approximation (GGA), which widened the range of applications drastically, in particular in chemistry. The GGA is a concrete form of the gradient expansion approximation (GEA) [23]. First implementations of the GEA tried to take higher order terms of a Taylor series in density gradients into account [28]. This ansatz, however, was shown to yield unreliable results. The reason can be found from a comparison between the fully interacting and the non-interacting auxiliary system. From the fully interacting Hamiltonian as defined in Eq. 2.14, we easily derive that the exchange-correlation potential $v_{\mathrm{xc}}(\vec{r})$ is given by the difference between the full interaction potential $v_{\mathrm{int}}(\vec{r})$ and the classical electron-electron repulsion, the Hartree potential $v_{\mathrm{H}}(\vec{r})$. In analogy to v_{H} (Eq. 2.10), we can define the potential energy $v_{\mathrm{int}}(\vec{r})$ (per electron) via $E_{\mathrm{int}} = \int v_{\mathrm{int}}(\vec{r})\rho(\vec{r})d^3r$. It seems intuitive to grasp v_{int} again as a density-dependent quantity [29] since it describes the interaction between an electron and the surrounding charge cloud. Here, however, one should bear in mind that the electron itself strongly interferes with the electron distributions around it due to quantum effects. Thus, there is a conditional density for an

electron at position $\vec{r}$, $\rho(\vec{r}'|\vec{r})$ [29], that defines the interaction potential

$$v_{\text{int}}(\vec{r}) = \frac{1}{2}\int d^3r' \frac{\rho(\vec{r}'|\vec{r})}{|\vec{r}-\vec{r}'|}. \tag{2.40}$$

The conditional probability is defined as

$$\rho(\vec{r}'|\vec{r}) = \frac{N(N-1)\int d^3r_3 ... \int d^3r_N \Psi^*(\vec{r},\vec{r}',\vec{r}_3,...\vec{r}_N)\Psi(\vec{r},\vec{r}',\vec{r}_3,...\vec{r}_N)}{N\int d^3r_2 \int d^3r_3 ... \int d^3r_N \Psi^*(\vec{r},\vec{r}_2,\vec{r}_3,...\vec{r}_N)\Psi(\vec{r},\vec{r}_2,\vec{r}_3,...\vec{r}_N)} = \frac{\rho(\vec{r},\vec{r}')}{\rho(\vec{r})}, \tag{2.41}$$

where the electron pair density constitutes the enumerator and the electron density the denominator. Then, we can write the exchange-correlation potential as

$$v_{\text{xc}}(\vec{r}) = v_{\text{int}}(\vec{r}) - v_{\text{H}}(\vec{r}) = \frac{1}{2}\int d^3r' \frac{\rho(\vec{r}'|\vec{r}) - \rho(\vec{r}')}{|\vec{r}-\vec{r}'|}, \tag{2.42}$$

and define the exchange-correlation hole

$$\rho_{\text{xc}}(\vec{r},\vec{r}') = \rho(\vec{r}'|\vec{r}) - \rho(\vec{r}') \tag{2.43}$$

to obtain an integral form for $v_{\text{xc}}(\vec{r})$ similar as for v_{int} and v_{H}. Physically, the exchange-correlation hole takes into account the simple fact that a classical picture is not valid any more for electrons. For example, due to the Pauli exclusion principle, an electron at position $\vec{r}$ does not allow for a second electron located at the same position (with the same spin) and affects electrons at $\vec{r}'$. In other words, each electron creates a depletion (hole) around it. Integration over the exchange-correlation hole yields a relation, which is referred to as sum rule,

$$\int \rho_{\text{xc}}(\vec{r},\vec{r}')d^3r' = -1. \tag{2.44}$$

From a further coupling constant integration, the exchange-correlation hole can be directly related with the Kohn-Sham exchange-correlation functional (see Sec. 2.4). This has important implications on the performance of the proposed GEA functionals. It turns out that the original realization of the GEA violates the sum rule for the exchange-correlation hole [30], while the LDA and Hartree-Fock fulfill these by definition.

This drawback could later be overcome by introducing a cutoff for higher order gradient contributions [31], which established the nowadays widely used generalized gradient approximation (GGA). For all flavors of GGA functionals, their general form is assumed as

$$E_{\text{xc}}^{\text{GGA}}[\rho] = \int f(\rho(\vec{r}), \nabla\rho(\vec{r}))d^3r, \tag{2.45}$$

with $f(\rho(\vec{r}, \nabla\rho(\vec{r}))$ to be defined suitably. The today most commonly used GGA implementation is the one developed by Perdew, Burke, and Ernzerhof (PBE-GGA) [32], which will be utilized for some calculations in this thesis. Another approach employed later will be the one by Perdew and Wang (PW91) [33], and many more GGA flavors might be listed here (e.g., B88 [34], rPBE [35]). The main difference between the schemes lies in the slightly different calculation of the exchange energy. For chemical purposes, such as calculations of atomization energies, all GGA flavors are superior to the LDA. This is because the GGA exchange-correlation energy per electron decays proportionally to the inverse distance at large distances, while it falls off exponentially in the LDA [12]. Hence, GGA cures LDA's affinity to overbind atoms in molecules, and is better suitable to reproduce binding energies in chemistry.

Higher-order derivative GEA methods, such as the meta-GGA [36], contain the second derivative of the density as well. There exist furthermore so-called hybrid functionals, which combine the exact exchange from Hartree-Fock theory with an exchange and correlation functional as GGA/LDA (e.g., B3LYP [37, 38]). The relative weight of terms is then determined by fits to the experiments. Going further upwards in Jacob's ladder leads finally to computationally demanding techniques, which are not based at all on homogeneous electron gas properties.

2.6 DFT in practice

The Kohn-Sham formalism, together with a suitable approximation to the exchange-correlation functional, such as the LDA or GGA, eventually enables calculating the ground state density of a real material. In practice, there are some more factors to bear in mind. First of all, an appropriate choice of the basis set has to be made. The basis set in a solid should meet various demands at once [12, 39]: near the core of an ion, the core potential is large and varies rapidly, and consequently, the wave function oscillates as well. The sensitivity to the chemical environment is weak in the core region, and the oscillations are due to large kinetic energies. In solids, bonds are formed between ions, and the nature of the bond formations determines the structure, stability and electronic properties. In the interstitial regions, thus, between ions and far away from the cores, the wave function is rather smooth and very responsive to the environment. Thus, large basis sets are required in the core region, while a small number of, e.g.,

plane waves, is sufficient between the ions. Some basis set implementations will be discussed in this section[1].

Local basis sets are widely used in quantum chemistry. A classic example is the linear combinations of atomic orbitals (LCAO) method [40], which provides an intuitive access to the wave function. The opposite ansatz is to choose a plane wave basis set, which is completely delocalized in space. Due to Bloch's theorem [41], it is ensured that the Kohn-Sham orbitals in reciprocal space can be expanded in plane waves

$$\psi_{\vec{k}}(\vec{r}) = \sum_{\vec{G}} c_{\vec{k}+\vec{G}} e^{i(\vec{k}+\vec{G})\vec{r}}, \tag{2.46}$$

with $\vec{G}$ the reciprocal lattice vector and the Fourier coefficients $c_{\vec{k}+\vec{G}}$. In practice, the infinite sum over $\vec{G}$ must be truncated in order to keep the basis set finite, thus, a kinetic energy cutoff is introduced,

$$\frac{\hbar^2}{2m}|\vec{k}+\vec{G}|^2 < E_{\text{cut}}, \tag{2.47}$$

which is justified by the fact that the coefficients $c_{\vec{k}+\vec{G}}$ decrease in weight for large $\vec{G}$. Furthermore, for numerical implementation, the wave function 2.46 is computed for a discrete set of $\vec{k}$ points. The finite number of plane waves and $\vec{k}$ points requires a careful convergence with respect to both in calculations. Especially in proximity to the nuclei, a large number of plane waves is needed due to the rapid oscillation of the core potential. A plane wave basis allows for the evaluation of the KS equation 2.34 in reciprocal space, leading eventually to a matrix equation

$$\sum_{G'} \left[\frac{1}{2}|\vec{k}+\vec{G}|^2\delta_{\vec{G}\vec{G}'} + v(\vec{G}-\vec{G}') + v_H(\vec{G}-\vec{G}') + v_{xc}(\vec{G}-\vec{G}')\right] c_{n,\vec{k}+\vec{G}'} = \epsilon_n c_{n,\vec{k}+\vec{G}} \tag{2.48}$$

being solvable via diagonalization.

2.6.1 Augmented Waves

Plane waves as such are not the ideal choice to capture the core wave function, and already in 1937 Slater proposed a method to overcome this issue, known as

[1] In this section and included subsections, derivations follow the books by Pavarini *et al.* [12] and Martin [10].

the augmented plane-wave method (APW) [42]. It is based on the idea of a space decomposition into the interstitial and the core region and the distinct definition of the wave function in both regions. Thereby, the core region around each atom is constituted by a sphere with a given radius, and a model potential is chosen, mostly a spherical muffin-tin potential, which is constant in the interstitial region. The partial waves within the sphere are energy-dependent in the original formulation by Slater, but this obstacle was later overcome by Andersen [43] through a linearization of the waves with respect to the energy. With this progress, APW schemes become computationally reachable for realistic materials. In the original formulation of the APW, the wave function was defined as [44]

$$\Phi_{\vec{G}}(\vec{r}) = \begin{cases} \sum_L a_L^{\alpha\vec{G}} u_l^\alpha(r', \epsilon) Y_L(\vec{r}'), & r' < R_\alpha \\ \Omega^{-1/2} \exp\left(i(\vec{k}+\vec{G})\vec{r}\right), & r \in I \end{cases}, \tag{2.49}$$

thus, as a plane-wave in the interstitial regions I, while within the sphere consisting of two factors: the radial-symmetric function $u_l^\alpha(r', \epsilon)$, which is a solution of the radial Schrödinger equation at a given energy ϵ, and an angular-dependent part, simply constituted by spherical harmonics (r and r' are spherical coordinates). Ω denotes the unit cell volume, and L includes the angular (l) and magnetic (m) quantum numbers; the vector $\vec{r}' = \vec{r} - \vec{r}_\alpha$ gives the position within a sphere α of radius R_α. The coefficients $a_L^{\alpha\vec{G}}$ ensure the matching of the augmented and the plane wave part at the sphere boundary. Inside the sphere, the above-mentioned problem of energy-dependent wave functions impedes straightforward computation of the solution. This is because the energy ϵ must equal the eigenvalue of the Kohn-Sham orbital, leading eventually to a non-linear eigenvalue problem.

The resulting computational efforts can be massively reduced by the following linearization,

$$\Phi_{\vec{G}}(\vec{r}) = \begin{cases} \sum_L \left[a_L^{\alpha\vec{G}} u_l^\alpha(r') + b_L^{\alpha\vec{G}} \dot{u}_l^\alpha(r')\right] Y_L(\vec{r}'), & r' < R_\alpha \\ \Omega^{-1/2} \exp\left(i(\vec{k}+\vec{G})\vec{r}\right), & r \in I \end{cases}, \tag{2.50}$$

thus, a linear combination of the radial function and its derivative $\dot{u}_l^\alpha = \partial u_l^\alpha / \partial \epsilon$ evaluated at a fixed energy ϵ_i. The linear coefficients are adjusted such that the basis function values and their derivatives are matched. In this way, the linearized augmented plane waves (LAPW) method offers evaluation of the eigenstates within one diagonalization. It is nowadays widely used in the solid-state

community and provides several remarkable benefits [45], among them the possibility to go behind the muffin-tin approximation to a full-potential treatment. A widely used LAPW code is the WIEN2k package [46], which will be utilized for simulations presented in Sec. 6.1. It should be noted that the linearization procedure facilitates another method, the linear muffin-tin orbital (LMTO) method, by employment of a basis of Hankel and Neumann functions [43]. Another "byproduct" of the original APW method is a Green's function technique based on scattering-theory, today known as KKR method [47, 48].

2.6.2 Pseudopotentials

An entirely different ansatz to the basis set problem of wave functions is a rather restricted treatment of the core potential. Due to the potential's rapidly oscillating nature around the nuclei, usually a large or complex basis set is needed. However, the chemistry of solids is, in many cases, only marginally affected by the core potential. The idea of the pseudopotential method is to replace the complicated core potential, which encompasses large Coulomb interactions between nuclei and electrons, by an effective, smoother ion potential. In this way, not only large basis sets are avoided, but also the number of electrons to be treated is reduced effectively. The potential is designed such that it accounts for the reduced electrostatic attraction by the protons through Pauli repulsion. In its most general form, the spherical pseudopotential reads as [49]

$$V_{\mathrm{PP}} = \sum_{lm} |lm\rangle \, V_l(r) \, \langle lm| \,, \tag{2.51}$$

with $\langle lm|$ denoting spherical harmonics and V_l the l-dependent pseudopotential. The operator is called semi-local, as it is non-local in l and m but local in r. Yet there exist local pseudopotentials that only depend on r.

The first *ab initio* construction of pseudopotentials based on atomic all-electron wave function calculations was proposed in the late 70's [50]. The so-called "norm-conserving pseudopotentials" provide nodeless eigenfunctions in the core region and reproduce scattering properties of isolated atoms to first order in energy. Furthermore, the norm-conservation ensures that the charge within the atomic sphere equals the charge of the corresponding atomic all-electron wave function. The sphere boundary is determined by a cutoff radius, and the pseudo wave function is constructed such that the augmented part and the interstitial part coincide at the cutoff radius. Thereby, the smooth pseudopotential makes a plane

wave expansion appropriate and a much lower plane-wave energy cutoff is needed, which reduces computational efforts drastically. More details on the construction of pseudopotentials can be found in, e.g., Ref. [10].

In many cases, pseudopotentials provide an adequate description of molecules and solids at reduced computational costs. This rendered possible the combination of molecular dynamics with electronic structure methods: *ab initio* molecular dynamics [51] allow for simulations of dynamics and temperature effects beyond the usual pair-potential approximation and offer ground state property calculations of large, disordered systems. This is achieved by an implementation of a combined electronic and ionic Lagrange formalism, where electron dynamics are included in a fictitious form.

Unfortunately, severe problems are faced with pseudopotentials for a large number of systems, related to issues with the underlying construction scheme. This is due to the problematic transferability of potentials of reference atoms to a system of bound atoms in a solid or molecule. Energy transferability is only viable in a finite energy window, in which the scattering properties of the reference atom are reproduced by the potential. This issue can be improved by a nonlinear core correction [52]. Another serious problem is about charge transferability, meaning that the potential of an isolated atom can be a bad choice to calculate the ground state wave function of atoms embedded in a molcecule or crystal. For instance, systems with first-row elements or $3d$ transition metals have strong pseudopotentials and require large basis sets, and it is hard to find balance between computational costs and accuracy for these materials. A progress was made by Vanderbilt [53], who released the norm-conservation constraint in his pseudopotential construction scheme for an improved convergence with respect to the basis set. This so-called "ultrasoft pseudopotential" method has some relations with the PAW method [54], that is discussed in the next section.

2.6.3 Projector augmented waves

So far, we have introduced two distinct methods to implement core-electron interaction: the augmented waves method, which aims to find a suitable basis set for an unmodified Hamiltonian, and the pseudopotentials method, which is based on reliable adaptions of the operators in the Hamiltonian. Blöchl showed that one can unify the "best of both worlds" into the method of projector augmented waves (PAW) [55]. Similar as Vanderbilts's ultrasoft pseudopotential method, it

is based on a combination of projectors and localized smooth auxiliary functions. The main idea is a linear transformation between the true wave function and a pseudo wave function[1],

$$|\psi\rangle = \mathcal{T}\,|\tilde{\psi}\rangle\,. \tag{2.52}$$

The pseudo wave functions $\tilde{\psi}$ must thereby reproduce the true wave function everywhere except in the core region that is represented by an augmentation sphere around the nucleus (with index R):

$$\mathcal{T} = 1 + \sum_R \mathcal{T}_R. \tag{2.53}$$

The local transformation operators $\mathcal{T}_R$ motivate an expansion of the wave function in all-electron (AE) partial waves $|\phi_i\rangle$ within each augmentation sphere, which we define in terms of pseudo (PS) partial waves $|\tilde{\phi}_i\rangle$ as

$$|\phi_i\rangle = (1 + \mathcal{T}_R)\,|\tilde{\phi}_i\rangle\,. \tag{2.54}$$

Then, the true wave function can be rewritten as

$$|\psi\rangle = \mathcal{T}\,|\tilde{\psi}\rangle = \sum_{i\in R} c_i\,|\phi_i\rangle\,, \tag{2.55}$$

with c_i the expansion coefficients and the index i representing the atomic site R and angular momentum quantum number (l, m). The pseudo partial waves $|\tilde{\phi}_i\rangle$ are claimed to coincide with the AE partial waves $|\phi_i\rangle$ beyond a core radius r_c and ought to be complete within the augmentation area, thus,

$$|\tilde{\psi}\rangle = \sum_{i\in R} c_i\,|\tilde{\phi}_i\rangle\,, \tag{2.56}$$

with the same coefficients c_i as given for the full wave function 2.55. They can be calculated using projection operators $\tilde{p}_i$ and the scalar product with the PS wave function:

$$c_i = \langle \tilde{p}_i | \tilde{\psi}\rangle\,. \tag{2.57}$$

The projector functions can be deduced from the condition $\sum_i |\tilde{\phi}_i\rangle\,\langle\tilde{p}_i| = 1$ since a one-center expansion of the PS wave function must equal the full pseudo wave function $|\tilde{\psi}\rangle$ within the augmentation sphere. This leads to the orthonormal relation

$$\langle \tilde{p}_i | \tilde{\phi}_j\rangle = \delta_{ij}. \tag{2.58}$$

[1] We closely follow Blöchl's original work [55] throughout this subsection.

Finally, we can rewrite the AE wave function in terms of the PS wave function by joining Eqs. 2.55, 2.56 and 2.57 to

$$|\psi\rangle = |\tilde{\psi}\rangle + \sum_i \left(|\phi_i\rangle - |\tilde{\phi}_i\rangle\right) \langle \tilde{p}_i|\tilde{\psi}\rangle = |\tilde{\psi}\rangle + \sum_R \left(|\tilde{\psi}^1_R\rangle - |\psi^1_R\rangle\right), \tag{2.59}$$

with a summation only over augmentation spheres in the last step, made possible through the one-center wave function on site R,

$$|\psi^1_R\rangle = \sum_{i\in R} |\phi_i\rangle \langle \tilde{p}_i|\tilde{\psi}_i\rangle, \tag{2.60}$$

$$|\tilde{\psi}^1_R\rangle = \sum_{i\in R} |\tilde{\phi}_i\rangle \langle \tilde{p}_i|\tilde{\psi}_i\rangle. \tag{2.61}$$

This is the central result of the PAW formalism with the transformation operator correspondingly reading as

$$\mathcal{T} = 1 + \sum_i \left(|\phi_i\rangle - |\tilde{\phi}_i\rangle\right) \langle \tilde{p}_i|. \tag{2.62}$$

The three important components of the transformation operator are (1) a set of AE partial waves $|\psi\rangle$, which can be obtained from the radial Schrödinger equation of the free atom, the corresponding partial pseudo wave functions $|\tilde{\psi}\rangle$ (2), and the projectors given above (3). These and the partial waves are computed as the product of real functions and spherical harmonics. A convenient expansion of the partial wave is done in plane waves.

Operators need to be transformed as well when it comes to practical application of the PAW method, since, then, the PS wave functions are the variational parameters and not the AE wave functions. An expectation value of an operator $\langle A\rangle = \sum_n f_n \langle \psi_n|A|\psi_n\rangle$ (n is the band index and f_n the occupation) is thus given in terms of a "pseudo" operator

$$\langle A\rangle = \sum_n f_n \langle \tilde{\psi}_n|\mathcal{T}^\dagger A \mathcal{T}|\tilde{\psi}_n\rangle, \tag{2.63}$$

which can be simplified for sufficiently local operators, such as the kinetic energy operator, as

$$\tilde{A} = \mathcal{T}^\dagger A \mathcal{T} = A + \sum_{i,j} |\tilde{p}_i\rangle \left(\langle \phi_i|A|\phi_j\rangle - \langle \tilde{\phi}_i|A|\tilde{\phi}_j\rangle\right) \langle \tilde{p}_j|. \tag{2.64}$$

This leads to a simplified expectation value (neglecting any contributions from core states),

$$\langle A \rangle = \sum_n f_n \langle \tilde{\psi}_n | A | \tilde{\psi}_n \rangle + \sum_{ij} D_{ij} \left(\langle \phi_j | A | \phi_i \rangle - \langle \tilde{\phi}_j | A | \tilde{\phi}_i \rangle \right), \tag{2.65}$$

with the one-center density matrix

$$D_{ij} = \sum_n f_n \langle \tilde{\psi}_n | \tilde{p}_j \rangle \langle \tilde{p}_i | \tilde{\psi}_n \rangle . \tag{2.66}$$

In order to apply the PAW method to DFT, the Kohn-Sham equations must be transformed accordingly. To this end, one has to vary the DFT energy functional with respect to the auxiliary wave functions. Since $\mathcal{T}$ is independent of the density, one obtains a PAW Schrödinger equation with the transformed Hamilton operator

$$\mathcal{T}^\dagger H_{KS} \mathcal{T} | \tilde{\psi}_n \rangle = \epsilon_n \mathcal{T} \mathcal{T}^\dagger | \tilde{\psi}_n \rangle \tag{2.67}$$

with H_{KS} the Kohn-Sham Hamiltonian as given in Fig. 2.1.

The electron density as the central quantity in DFT can accordingly be decomposed into three terms, similar to the wave function (Eq. 2.59),

$$\rho(\vec{r}) = \tilde{\rho}(\vec{r}) + \sum_R \left(\rho_R^1(\vec{r}) - \tilde{\rho}_R^1(\vec{r}) \right), \tag{2.68}$$

as a sum over one-center densities inside augmentation regions R, with

$$\tilde{\rho}(\vec{r}) = \sum_n f_n \langle \tilde{\psi}_n | \tilde{\psi}_n \rangle , \tag{2.69}$$

$$\rho_R^1(\vec{r}) = \sum_{ij \in R} D_{ij} \langle \phi_j | \phi_i \rangle , \tag{2.70}$$

$$\tilde{\rho}_R^1(\vec{r}) = \sum_{i,j \in R} D_{ij} \langle \tilde{\phi}_j | \tilde{\phi}_i \rangle . \tag{2.71}$$

The total energy is equally decomposed of three summands, and its precise form can be found in the original work by Blöchl [55]. Thus, in a nutshell, the PAW method is an all-electron method with a computational efficiency close to the pseudopotential method, and there is no need to construct the full wave function. The method allows for a relatively simple implementation in existing pseudopotential codes (as it is done in the VASP code). The PAW approach offers an accuracy close to the full-potential all-electron LAPW method [54]; also, PAW is superior to pseudopotentials for calculations of magnetic energies. For this reason, it is nowadays widely used in DFT packages, such as VASP (see below).

2.6.4 DFT packages

Most of the first-principles calculations presented in this thesis were performed with the Vienna *ab initio* simulation package (VASP). It features both the PAW and Vanderbilts' ultrasoft pseudopotential method, and the wave function is expanded using a plane-wave basis set. The plane waves allow for easy control of convergence with respect to the basis set. Moreover, atomic forces and stresses can be easily evaluated, which facilitates *ab initio* molecular dynamics calculations [56].

The Kohn-Sham problem is solved by means of an iterative minimization of a residual vector

$$|R_n\rangle = (H - E)\,|\tilde{\Psi}_n\rangle \tag{2.72}$$

with the energy

$$E = \frac{\langle\tilde{\Psi}_n|H|\tilde{\Psi}_n\rangle}{\langle\tilde{\Psi}_n|\tilde{\Psi}_n\rangle}, \tag{2.73}$$

where $\tilde{\Psi}_n$ is a trial wave function, that gets refined by adding a small amount of the residual vector in each iteration:

$$|\tilde{\Psi}_n\rangle \rightarrow |\tilde{\Psi}_n\rangle + \lambda\,|R_n\rangle\,. \tag{2.74}$$

The minimzation of a residual vector instead of the eigenvalues is computationally efficient and does not involve orthogonality constraints. The trial wave vectors span a subspace, in which the Kohn-Sham Hamiltonian is diagonalized. For this purpose, the *blocked Davidson* (DAV) algorithm, the *direct inversion in the iterative subspace* (DIIS) algorithm, and the *conjugate gradient* (CG) algorithm are employed. The Davidson algorithm is, although slower than the DIIS algorithm, mostly a good choice due to stable convergence. For ionic optimization, VASP features different techniques to relax ion positions, namely, a DIIS, a CG, and damped molecular dynamics algorithm. Detailed information on the algorithms, the code implementation and the rich functionality of the VASP package can be found elsewhere [54, 56, 57].

Another widely used DFT package[1] is the full potential all-electron code WIEN2k [46], which is based on the LAPW method. It is implemented in the computationally efficient flavor "LAPW+local orbitals" (LAPW+lo) [58] with

[1] In this thesis, the WIEN2k package was used for XAS simulations of Ni adatoms on graphene, see Sec. 6.1

augmentations similar to the original LAPW scheme, but with a fixed linearization energy in order to prevent non-linearity of the eigenvalue problem. Recommendable reviews on the WIEN2k package are given in Refs. [44, 59].

2.7 van der Waals interaction in density functional theory

A major deficiency of the exchange-correlation functionals presented in Sec. 2.5 is their failure in the description of van der Waals interaction, an ubiquitous phenomenon of long-range correlation in matter. The random phase approximation (RPA) to the correlation energy provides a natural inclusion of long-range correlation [60] and can be seen as a many-body perturbation theory "on top" of DFT. Evaluated in the framework of the "adiabatic connection-fluctuation dissipation theorem" (ACFDT), the correlation energies offer a computationally efficient description of structural properties of solids, including lattice constants and atomization energies [61]. The ACFDT-RPA method "handles ionic, metallic, and van der Waals bonded systems equally well" [60] and yields an excellent description of (weak) molecular binding on metallic surfaces [62] and binding energies in weakly bound layered systems, such as bulk graphite [63] and h-BN [64]. Other methods will be briefly discussed in this section, too, such as van der Waals-corrected functionals and (semi-)empirical van der Waals correction techniques.

2.7.1 ACFDT-RPA total energies

We shortly reflect the idea behind the ACFDT and the computational implementation. The derivations follow Refs. [65] and [66]. Our starting point is the following Hamiltonian, which looks similar to the Hamiltonian used in standard KS-DFT, but exhibits some important coupling parameter $0 \leq \lambda \leq 1$:

$$H(\lambda) = T + V(\lambda) + \lambda V_{\mathrm{ee}}, \tag{2.75}$$

with $V_{\mathrm{ee}} = \sum_{i<j} e^2/|\vec{r}_i - \vec{r}_j|$ the electron-electron interaction and $V(\lambda) = \sum_i v_\lambda(\vec{r}_i)$ a sum of local potential terms. For $\lambda = 0$ (non-interacting), we set $V(0) = v_0(\vec{r}_i) = v_{\mathrm{KS}}(\vec{r}_i)$, and the (non-interacting) KS-Hamiltonian is restored since the electron-electron term V_{ee} vanishes. Remember that, provided the exchange-correlation energy is precisely known, the ground state of the KS-Hamiltonian can be determined exactly. However, the exact form of the exchange-correlation

energy for most realistic systems is unknown and must be approximated, e.g., by local approximations (such as LDA/GGA) which imply systematic errors including self-interaction errors and a wrong description of long-range dispersions [61]. The framework of ACFDT provides an alternative, yet exact, access to the exchange-correlation energy. By switching the electron-electron interaction on ($\lambda > 0$), we reformulate the Hamiltonian in a way that assures the density of the interacting system to be the same as for the KS system ($\lambda = 0$). Therefore, we require that $V(\lambda)$ be conveniently chosen. Obviously, for the fully interacting case ($\lambda = 1$), $V(1) = \sum_i v_{\text{ext}}(\vec{r}_i)$ (cf. Eq. 2.30).

For structural properties, we want to evaluate the total energy of the system, which is the expectation value of the Hamiltonian:

$$E = \langle \Psi(\lambda) | H(\lambda) | \Psi(\lambda) \rangle , \tag{2.76}$$

with $\Psi(\lambda)$ being the eigenstate of $H(\lambda)$. For $\lambda = 0$, we end up with the KS total energy,

$$E = T_s + E_{\text{H}} + E_{\text{ext}} + E_{\text{xc}} \tag{2.77}$$

while $\lambda = 1$ yields

$$E = \langle \Psi(1) | T + V_{\text{ee}} | \Psi(1) \rangle + E_{\text{ext}}. \tag{2.78}$$

The combination of Eq. 2.78 and 2.77 together with the Hellmann-Feynman theorem yields (after some algebra) the Hartree exchange correlation energy [66]

$$E_{\text{Hxc}} = \int_0^1 d\lambda \, \langle \Psi(\lambda) | V_{\text{ee}} | \Psi(\lambda) \rangle , \tag{2.79}$$

for which we can evaluate the total energy of the system (without the need to explicitly construct the entire density matrix):

$$E = T_{\text{KS}} + E_{\text{ion-el}} + E_{\text{Hxc}}. \tag{2.80}$$

Here, T_{KS} denotes the Kohn-Sham kinetic energy and $E_{\text{ion-el}}$ the core-electron interaction. After the adiabatic connection, we apply the fluctuation-dissipation theorem [67], which we use to reformulate the Hartree exchange-correlation energy by expressing the correlation part as a function of the density-density response function

$$E_{\text{Hxc}} = E_{\text{H}}[n] + E_{\text{x}}\left[\left\{\psi_i^{\text{KS}}\right\}\right] - E_{\text{c}} \tag{2.81}$$

with

$$E_{\text{c}} = \int_0^1 d\lambda \int_0^\infty \frac{d\omega}{2\pi} \text{Tr}\left\{\nu\left[\chi^\lambda(i\omega) - \chi^{\text{KS}}(i\omega)\right]\right\}, \tag{2.82}$$

whereby χ^{KS} and χ^{λ} are the response functions of the non-interacting Kohn-Sham system and of the interacting system, respectively. $\nu(\vec{r}-\vec{r}\,') = \frac{e^2}{|\vec{r}-\vec{r}\,'|}$ is the Coulomb interaction. Both response functions can be related by a Dyson-like equation, which reads in reciprocal space

$$\left[\chi^{\lambda}\left(\vec{q}, i\omega\right)\right]^{-1} = \left[\chi^{\mathrm{KS}}\left(\vec{q}, i\omega\right)\right]^{-1} - \left[\lambda\nu(\vec{q}) + f_{\mathrm{xc}}^{\lambda}\left(\vec{q}, i\omega\right)\right], \tag{2.83}$$

with $f_{\mathrm{xc}}^{\lambda}$ being the exchange-correlation kernel. This leads to an exact expression for the correlation energy and therefore, the total ACFDT energy can then, at least in principle, be evaluated exactly. Practically, however, we apply the *random phase approximation* (RPA) by setting $f_{\mathrm{xc}}^{\lambda} = 0$. After this approximation, the integration over λ can be performed analytically, leading after some algebra to

$$E_{\mathrm{c}}^{\mathrm{RPA}} = \int_0^{\infty} \frac{d\omega}{2\pi} \mathrm{Tr}\{\ln\left[1 - \nu\chi^{\mathrm{KS}}(\mathrm{i}\omega)\right] + \nu\chi^{\mathrm{KS}}(\mathrm{i}\omega)\}. \tag{2.84}$$

In practice, the total energy calculation is now divided into two parts: First, the KS/Hartree-Fock total energy is calculated according to the energy definitions of Eqs. 2.80 and 2.81, with all terms included except for the correlation energy. Finally, the total energy results from adding E_{c} (Eq. 2.84), which is calculated using the response functions constructed from KS orbitals (for a definition of the response function and more details, cf. again [65] and [66]).

2.7.2 Other methods for van der Waals interaction

The van der Waals density functional method (vdW-DF) [68] provides an inclusion of non-local interactions directly in the exchange-correlation functional, in contrast to the ACFDT-RPA method. The vdW-DF is based on a redefinition of E_{xc} in three terms [69],

$$E_{\mathrm{xc}} = E_{\mathrm{x}}^{\mathrm{GGA/EXX}} + E_{\mathrm{c}}^{\mathrm{LDA/GGA}} + E_{\mathrm{c}}^{\mathrm{nl}}, \tag{2.85}$$

where the first term is the exchange part either from GGA or in the "exact" form, the second part the correlation treated locally within LDA or GGA, and, most importantly, the last term, which includes non-local interactions in an approximate form [70]:

$$E_{\mathrm{c}}^{\mathrm{nl}}\left[\rho\right] = \int d^3r \int d^3r' \rho(\vec{r})\phi(\vec{r}, \vec{r}\,')\rho(\vec{r}\,'). \tag{2.86}$$

It can be derived from a local approximation to the response function in the framework of the adiabatic connection (Eq. 2.82, see [68]). The kernel ϕ is a

general function of the density and its gradient. Different flavors of vdW-DF have been proposed and proven to be a substantial improvement over LDA/GGA for van der Waals dispersion in solids [70, 71] at low computational cost.

An alternative are interatomic vdW methods that have empirical character to a certain degree. Typically, such methods are implemented in DFT codes for simple, effective post-processing usage. An empirical method widely used is the DFT-D method [72], which simply adds to the total Kohn-Sham energy a damped potential term of interatomic long-range interactions:

$$E_{\text{total}} = E_{\text{KS}} + E_{\text{vdW}}. \tag{2.87}$$

The potential term in the formulation of Grimme [73] reads as

$$E_{\text{vdW}} = -s_6 \sum_{i=1}^{N_{\text{at}}-1} \sum_{j=i+1}^{N_{\text{at}}} \frac{C_6^{ij}}{R_{ij}^6} f_{\text{dmp}}(R_{ij}), \tag{2.88}$$

which is referred to as the DFT-D2 method. The DFT-D2 method will be used for calculations of Sec. 5.3 and is implemented in the VASP code together with the vdW-DF method. The double sum over N_{at} atoms contains two empirical parameters for each atomic pair with the distance R_{ij}. The first one is the dispersion coefficient C_6^{ij}. The damping function, which avoids near-singularities for small R_{ij},

$$f_{\text{dmp}}(R_{ij}) = \frac{1}{1 + e^{-d(R_{ij}/R_r - 1)}}, \tag{2.89}$$

contains the other empirical parameter R_r, which is the sum of the atomic van der Waals radii. Grimme [73] determined empirical parameters from experiments and Hartree-Fock binding energies, but parameters can also be obtained from different ground state theories to reduce the degree of empiricism [74, 75, 76]. The global scaling parameter s_6 is optimized for the individual approximation on the exchange-correlation functional (mostly LDA or GGA). Typically, the correction is applied after convergence of the Kohn-Sham cycle (Fig. 2.1); from the corrected total energy, interatomic forces are then calculated, such that the geometry of the system can be optimized at very low computational costs and accuracy similar to vdW-DF methods. However, compared to RPA, DFT-D2 is inferior in performance due to the highly empirical character and the simplicity of the method.

2.8 Coulomb interactions in DFT

Another well-known failure of standard density functional theory occurs for strongly correlated systems, thus, any type of electron interactions behind the Hartree-Fock level. For real materials, this concerns usually open d and f shell systems, i.e., transition metals, rare earth and actinide elements. In a correlated material, electrons normally behave very differently than one-particle methods predict (see, e.g., [77]). Some electrons, usually those from the s and p shells, exhibit a wave-like character and are well-described in an independent-particle picture. Such weakly correlated particles are rather delocalized over the solid and accurately described within the flavors of density functional theory presented above. In contrast, states from the d and f shell tend to localize around atoms and are strongly affected by each other, e.g., through Coulomb repulsion. In this case, electrons behave rather like particles, and methods such as LDA fail to describe the effect of such strong correlations. In band structure theory, the small kinetic energy of the states leads to narrow bands, and for open shell systems, these states are present near the Fermi level. Thus, electronic correlations have important implications on fundamental material properties, such as electrical and heat transport or optical properties. A classic example for the collapse of LDA/GGA is the emergence of the famous Mott insulating phase for transition metal oxides such as NiO [78]. LDA/GGA and simpler band theories predict a purely metallic phase of NiO in disagreement with the experiment. In the following, we briefly discuss some methods suitable to take correlations in a real material simulation into account, as far as this is possible.

2.8.1 DFT+U

The problems of DFT with strong correlations are not related with the general scheme, but rather a consequence of an inadequate approximation to the exchange-correlation energy, such as is done in the LDA or the GGA. A computationally efficient correction to the energy functional is given by the DFT+U method [79, 80, 81]. Thereby, the total Kohn-Sham energy is complemented by two additional terms. Let us consider a system with localized d or f orbitals with occupancy n_i. Then, the Coulomb interaction can be approximated in a simple

Hubbard-like form[1],

$$E_{\mathrm{DFT+U}} = E_{\mathrm{DFT}} + E_U - E_{\mathrm{DC}} = E_{\mathrm{DFT}} + \frac{1}{2}U\sum_{i\neq j} n_i n_j - \frac{UN(N-1)}{2}, \quad (2.90)$$

where the second term describes the electron-electron interaction in a static mean-field (at first, we neglect the exchange coupling). The last term subtracts the so-called double counting energy, because the LDA already incorporates correlation to some unknown extent. Therefore, the definition of the double counting term is not unique; though, the term given here is reasonable under the assumption that the total Coulomb energy, which depends on the total number of electrons $N = \sum_i n_i$ in the correlated d or f shell, is well-approximated by the LDA. The corresponding orbital energies are then given by

$$\epsilon_i = \frac{\partial E}{\partial n_i} = \epsilon_{\mathrm{DFT}} + U(\frac{1}{2} - n_i). \quad (2.91)$$

This is the basic idea behind DFT+U, and in the following, we briefly discuss some connections with other methods presented so far. Interestingly, DFT+U is indirectly related with the RPA method discussed in Sec. 2.7.1. This is because DFT+U can be seen as an approximate form of the so-called "GW" method [82], which is diagramatically equivalent to the RPA [83]. The GW method is a Green's function technique used to approximate the self-energy of the (reformulated) many-body problem

$$H_0\Psi(\vec{r}) + \int d\vec{r}_1 \Sigma(\vec{r}, \vec{r}_1, E)\Psi(\vec{r}_1) = E\Psi(\vec{r}), \quad (2.92)$$

with H_0 the Hamiltonian on a Hartree level, and Σ the energy-dependent self-energy[2]. The precise form of the self-energy is of course unknown, but it may be written in the GW approximation as

$$\Sigma(\vec{r}, \vec{r}\,'; \omega) = \frac{i}{2\pi}\int_{-\infty}^{\infty} d\omega' G(\vec{r}, \vec{r}\,'; \omega + \omega')W(\vec{r}, \vec{r}\,'; \omega)e^{i\delta\omega'}, \quad (2.93)$$

with the screened Coulomb interaction

$$W(\vec{r}, \vec{r}\,'; \omega) = v(\vec{r} - \vec{r}\,') + \int d^3r_1 d^3r_2 v(\vec{r}\,' - \vec{r}_1)P(\vec{r}_1, \vec{r}_2; \omega)v(\vec{r}_2 - \vec{r}\,'). \quad (2.94)$$

[1] The derivations and explanations given in this subsection follow closely the review by Anisimov *et al.* [81]

[2] The energy-dependence is in the following expressed by the frequency ω

$P(\vec{r}_1, \vec{r}_2; \omega)$ denotes the full response function and $v(\vec{r})$ is the bare Coulomb interaction. Given the spectral function $A(\vec{r}, \vec{r}\,'; \omega)$, which we express by means of KS orbitals as

$$A(\vec{r}, \vec{r}\,'; \omega) = -\frac{1}{\pi} \operatorname{Im} G(\vec{r}, \vec{r}\,'; \omega) \operatorname{sgn}(\omega - \mu) = \sum_{\mathrm{kn}} \psi_{\mathrm{kn}}(\tilde{\mathrm{r}}) \psi^*_{\mathrm{kn}}(\tilde{\mathrm{r}}\,') \delta(\omega - \epsilon_{\mathrm{kn}}), \quad (2.95)$$

we obtain the time-ordered Green's function

$$G(\vec{r}, \vec{r}\,'; \omega) = \int_{-\infty}^{\mu} d\omega' \frac{A(\vec{r}, \vec{r}\,'; \omega)}{\omega - \omega' - i\delta} + \int_{\mu}^{\infty} d\omega' \frac{A(\vec{r}, \vec{r}\,'; \omega)}{\omega - \omega' + i\delta}. \quad (2.96)$$

This allows for a separation of the self-energy in an exchange and a correlation part,

$$\Sigma(\vec{r}, \vec{r}\,'; \omega) = \Sigma_{\mathrm{x}}(\vec{r}, \vec{r}\,') + \Sigma_{\mathrm{c}}(\vec{r}, \vec{r}\,'; \omega), \quad (2.97)$$

where the exchange part is evaluated with the help of the bare interaction

$$\Sigma_{\mathrm{x}}(\vec{r}, \vec{r}\,') = -\sum_{kn}^{\mathrm{occ}} \psi_{kn}(\vec{r}) \psi^*_{kn}(\vec{r}\,') v(\vec{r} - \vec{r}\,'), \quad (2.98)$$

and the correlated part consists of two separated summations, one over occupied, and another over unoccupied states,

$$\begin{aligned} \Sigma_{\mathrm{c}}(\vec{r}, \vec{r}\,'; \omega) = &\sum_{kn}^{\mathrm{occ}} \psi_{kn}(\vec{r}) \psi^*_{kn}(\vec{r}\,') W^-_{\mathrm{c}}(\vec{r}, \vec{r}\,'; \omega - \epsilon_{kn}) \\ &+ \sum_{kn}^{\mathrm{unocc}} \psi_{kn}(\vec{r}) \psi^*_{kn}(\vec{r}\,') W^+_{\mathrm{c}}(\vec{r}, \vec{r}\,'; \omega - \epsilon_{kn}). \end{aligned} \quad (2.99)$$

The screening $W^{\pm}_{\mathrm{c}}$ is defined as

$$W^{\pm}_{\mathrm{c}}(\vec{r}, \vec{r}\,'; \omega) = \frac{i}{2\pi} \int_{-\infty}^{\infty} d\omega' \frac{\int d^3 r_1 d^3 r_2 v(\vec{r}\,' - \vec{r}_1) P(\vec{r}_1, \vec{r}_2; \omega) v(\vec{r}_2 - \vec{r}\,')}{\omega + \omega' \pm i\delta}. \quad (2.100)$$

In this form, the self-energy is reminiscent of the Hartree-Fock self-energy, but with an energy dependence and unoccupied orbitals included. From this point of view, GW is a generalization of Hartree-Fock theory. The following further approximations to the GW method yield the DFT+U scheme. The aim of DFT+U is to give a self-energy correction to the localized states around the correlated atom. These localized states must be at first separated from the delocalized

states, so we consider the correlated self-energy of occupied localized states ψ_d only,

$$\begin{aligned}\langle\psi_d|\Sigma_{\rm c}(\epsilon_d)|\psi_d\rangle &= \langle\psi_d\psi_d|W_{\rm c}^-(0)|\psi_d\psi_d\rangle \\ &+ \sum_{kn\neq d}^{\rm occ}\langle\psi_d\psi_{kn}|W_{\rm c}^-(\epsilon_d-\epsilon)|\psi_{kn}\psi_d\rangle + \sum_{kn}^{\rm unocc}\langle\psi_d\psi_{kn}|W_{\rm c}^+(\epsilon_d-\epsilon)|\psi_{kn}\psi_d\rangle\,,\end{aligned} \tag{2.101}$$

by cancelling the (small) terms of the second line and considering $W_{\rm c}^-(0)$ only, which can be shown to yield

$$\langle\psi_d|\Sigma_{\rm c}(\epsilon_d)|\psi_d\rangle \approx \langle\psi_d\psi_d|W_{\rm c}^-(0)|\psi_d\psi_d\rangle = -\frac{1}{2}\langle\psi_d\psi_d|W_{\rm c}(0)|\psi_d\psi_d\rangle\,. \tag{2.102}$$

The same result follows for unoccupied states, but with a negative sign in Eq. 2.102. Then, their energy separation is

$$\Delta = \epsilon_2^{\rm HF} - \epsilon_1^{\rm HF} + \langle\psi_d\psi_d|W_{\rm c}(0)|\psi_d\psi_d\rangle = \langle\psi_d\psi_d|W(0)|\psi_d\psi_d\rangle\,, \tag{2.103}$$

in agreement with the naive expectation $\Delta = U \approx W(0)$. Then, we can write the self-energy correction to the DFT exchange-correlation energy as

$$\Delta\Sigma(\vec{r},\vec{r}\,';\epsilon_d) = \Sigma(\vec{r},\vec{r}\,';\epsilon_d) - E_{\rm xc}^{\rm DFT}(\vec{r})\delta(\vec{r}-\vec{r}\,'). \tag{2.104}$$

This correction is, as can be shown by further derivations, equivalent to the U term in the DFT+U formula of the very beginning (see again Ref. [81]). Thus, the DFT+U method is, for localized orbitals, an approximation applied to the GW approximation itself, and, by definition, of Hartree-Fock-type. The general total energy functional in the DFT+U method includes an exchange parameter J and spin-polarized states and can be rewritten as a function of the density matrix $n^\sigma_{mm'}$ (in localized representation, with orbital index m and spin σ):

$$E_{\rm DFT}\left[\rho^\sigma(\vec{r}),\{n^\sigma_{mm'}\}\right] = E_{\rm DFT}\left[\rho^\sigma\right] + E_U\left[n^\sigma\right] - E_{\rm DC}\left[n^\sigma\right]. \tag{2.105}$$

The interaction term is given by

$$\begin{aligned}E_U\left[n^\sigma\right] = \frac{1}{2}\sum_{mm'm''m''',\sigma}&\big[\langle mm''|V_{\rm el-el}|m'm'''\rangle\, n^\sigma_{mm'}n^{-\sigma}_{m''m'''} - \\ &(\langle mm''|V_{\rm el-el}|m'm'''\rangle - \langle mm''|V_{\rm el-el}|m'''m'\rangle)n^\sigma_{mm'}n^\sigma_{m''m'''}\big]\,,\end{aligned} \tag{2.106}$$

where $V_{\rm el-el}$ is approximated in terms of Slater integrals [84] in the spirit of the LSDA.[1]

[1] To learn more about Slater integrals, see, e.g., Ref. [85].

The double counting term, now more precisely defined than in Eq. 2.90, is written in the "fully localized limit" [86],

$$E_{\mathrm{DC}}\left[n^{\sigma}\right] = \frac{1}{2}UN(N-1) - \frac{1}{2}J\left[N^{\uparrow}(N^{\uparrow}-1) + N^{\downarrow}(N^{\downarrow}-1)\right], \tag{2.107}$$

and yields the Coulomb energy of an isolated atomic shell ($N^{\sigma} = \mathrm{Tr}(n^{\sigma}_{mm'})$ and $N = N^{\uparrow} + N^{\downarrow}$). Another type of double counting is known as the "around mean-field" (AMF) version [79]. It is based on the assumption of an average orbital occupancy, thus, a diagonal density matrix, which turns out to be problematic for many strongly correlated systems. Therefore, the FLL type of double counting is widely used today and also in our calculations presented in Sec. 7 and 6.2.

2.8.2 DFT++

The DFT+U method, albeit highly successful in reproducing electronic and structural properties of correlated systems, is naturally restricted in its performance when effects beyond static mean-field theory emerge in experiments. A classic example is the Kondo effect [87], which is, as a dynamical effect, inaccessible in DFT+U. A general scheme, called "DFT++" in the following, provides an interface for the computationally feasible combination of the DFT and model Hamiltonians.

Model Hamiltonians for strongly correlated electrons can be divided into two main classes: quantum lattice models and quantum impurity models. For electron interactions in lattices, a simple looking, yet challenging example model Hamiltonian is the Hubbard model [88, 89, 90] that can be heuristically derived [12] by rewriting Hamiltonian 2.6 in second quantization,

$$H_{\mathrm{int}} = \sum_{ij\sigma} t_{ij} c^{\dagger}_{i\sigma} c_{j\sigma} + \frac{1}{2} \sum_{\substack{ijkl \\ \sigma\neq\sigma'}} U_{ijkl} c^{\dagger}_{i\sigma} c^{\dagger}_{j\sigma'} c_{k\sigma'} c_{l\sigma}, \tag{2.108}$$

where $U_{ijkl} = \langle ij|V_{\mathrm{e-e}}|lk\rangle$, c_i ($c^{\dagger}_i$) annihilates (creates) a fermion, i, j, k, l represents the site and orbital index and σ the spin. In the most simple form, the Hubbard interaction U_{ijkl} and the hopping t_{ij} are assumed to be uniform, the hopping integral only taken for nearest-neighbor sites. Furthermore, the Coulomb interaction is adopted in its most local form, for two electrons on the same site with opposite spin (due to Pauli's principle) and only one orbital per site assumed.

This can be condensed in a single-band Hubbard model

$$H_{\text{int}} = -t \sum_{\langle ij \rangle \sigma} c_{i\sigma}^{\dagger} c_{j\sigma} + U \sum_{i} n_{i\uparrow} n_{i\downarrow}, \tag{2.109}$$

with $n_{i\sigma} = c_{i\sigma}^{\dagger} c_{i\sigma}$ the particle number operator. Remarkably, the simplicity of the model is sufficient to cover a broad range of properties in phase diagrams of correlated systems, including metal-insulator transitions, and superconductivity [12]. It can be analytically solved only in the one-dimensional case, and requires huge efforts in computational handling. In infinite dimensions, the Hubbard model 2.109 can be solved with numerical exactness by means of the "Dynamical mean-field theory" (DMFT) [91], and this method is also widely used as an approximation to the Hubbard model in two or three dimensions. Details about DMFT can be found, for instance, in Refs. [12, 91, 92], it should merely be remarked that the DMFT is based on a mapping of the lattice problem onto an Anderson impurity model.

The Anderson impurity model (AIM) [93] was designed to explain the behavior of magnetic impurities in metallic hosts, and it is the prototype impurity model to investigate the interplay of electron itinerancy and localized impurity states. The competition of delocalized states and strongly correlated impurity states is formulated in the AIM as

$$H_{\text{AIM}} = \sum_{k\sigma} \epsilon_k c_{k\sigma}^{\dagger} c_{k\sigma} + \sum_{km\sigma} \left(V_{km} c_{k\sigma}^{\dagger} d_{m\sigma} + V_{km}^{*} d_{m\sigma}^{\dagger} c_{k\sigma} \right) + H_{\text{local}}, \tag{2.110}$$

whereby the first term describes the sea of conduction electrons with a k-dependent dispersion and fermionic creation (annihilation) operators $c_{k\sigma}^{\dagger}$ ($c_{k\sigma}$). The second term denotes their hybridization V_{km} with the impurity states, represented by a Fermi operator $d_{m\sigma}$ with orbital index m and spin index σ (the site index is no longer needed). The local part of the Hamiltonian encompasses states only related with the impurity and is given by

$$H_{\text{local}} = \sum_{m\sigma} \epsilon_{dm} d_{m\sigma}^{\dagger} d_{m\sigma} + \frac{1}{2} \sum_{\substack{mm'm''m''' \\ \sigma\sigma'}} U_{mm'm''m'''} d_{m\sigma}^{\dagger} d_{m'\sigma'}^{\dagger} d_{m''\sigma'} d_{m'''\sigma}, \tag{2.111}$$

with the local impurity on-site energy ϵ_{dm} and the local Coulomb interaction tensor $U_{mm'm''m'''}$. The model allows for investigations of Kondo physics, magnetic moment formation, and temperature effects on impurities, and it is widely discussed in the literature (see, e.g., Ref. [12, 87]).

The solution of an AIM, i.e., the computation of the local propagator, the Green's function of correlated systems, $G_{mm'}(\tau,\tau') = -\langle \mathcal{T}_\tau d_m(\tau) d^\dagger_{m'}(\tau')\rangle$, is challenging, as can be seen from the diversity of available impurity solvers. Besides perturbative treatments, today frequently used are numerical methods, such as the renormalization group [94] or exact diagonalization techniques [95]. Furthermore, there exist a number of quantum Monte Carlo techniques (QMC), such as continuous-time quantum Monte Carlo (CT-QMC) [96], or Hirsch-Fye QMC [97].

After setting up a Hubbard model or an AIM, the decisive step in DFT++ is the interfacing of the model Hamiltonian with the DFT one-particle Hamiltonian. The literature on practical implementations of DFT++ is rich (cf., e.g., Refs. [12, 98, 99, 100] and references therein), but in general, the characteristic DFT++ Hamiltonian reads, in analogy to Eq. 2.105,

$$H_{\mathrm{DFT++}} = H_{\mathrm{DFT}} + H_U - H_{\mathrm{DC}}, \tag{2.112}$$

where the pure DFT Hamiltonian $H_{\mathrm{DFT}} = \epsilon_k c^\dagger_{k\sigma} c_{k\sigma}$ is complemented by an interaction and a double counting term. For an impurity, H_U can be identified with the interaction part of the local Hamiltonian Eq. 2.111, and the double counting correction is due to some correlation included already in the DFT energy functional:

$$H_{\mathrm{DC}} = \mu_{\mathrm{DC}} \sum_{m,\sigma} c^\dagger_{m\sigma} c_{m\sigma} \tag{2.113}$$

In fact, the double counting correction is nothing but a shift of the chemical potential of the interacting states, and it cancels the Coulomb energy contributions from the pure DFT results. In analogy to Sec. 2.8.1, first the correlated subspace is defined. Then, the double counting correction, which controls the filling of the correlated orbitals, needs to be chosen properly.

3

Two-dimensional crystals: an overview

Isolated nanosheets with the thickness of an atom or a molecule are commonly referred to as two-dimensional (2D) crystals. In experiments, these materials are mostly exfoliated from their three-dimensional counterparts, i.e., from a van der Waals solid, which can be considered as a large stack of weakly (van der Waals) bound 2D layers. In fact, 2D crystals are much more than just the building blocks of van der Waals solids. The past years of research in this young area proved the outstanding prospects of 2D crystals for novel applications as well as the rich diversity of unknown fundamental phenomena related with these materials. At first glance, this development seems rather surprising with decades of precedent research on materials such as bulk graphite, MoS_2, and so on, which are nowadays heavily investigated in their (isolated) 2D form. However, a brief look at the widely varying properties of carbon allotropes, from diamond (3D) over carbon nanotubes (1D) to fullerenes (0D) should be proof enough of the importance of dimensionality for nanomaterials in general.

Research on 2D materials has rapidly developed into a vast field over the past few years. Therefore, and due to the diversity of materials investigated in this thesis, a brief overview of the most important members of the "family" of 2D crystals will be given in this chapter, with a special focus on their electronic properties.

3.1 Graphene

The research on two-dimensional crystals was initiated ten years ago with the first isolation of carbon monolayers ("graphene") from graphite crystals [2]. The simple, yet ingenious idea to produce atomically thin carbon films by the meanwhile famous "scotch tape" method evoked an explosion of research effort in this area, producing thousands of publications and patents each year. Graphene attracts researchers and engineers of sundry backgrounds, and it unites a number of unique properties. Albeit having a simple 2D lattice structure, graphene generates fundamental new questions in condensed matter physics and unpredicted phenomena. Its quasi-relativistic behavior even attracts research interest in the high energy physics community ("CERN on one's desk" [101]). Besides all that, possibly the most intriguing aspects of graphene research are about already realized and future applications of this material, in various industry fields, from flexible nanoelectronics over photovoltaics to composite materials (for a review on the prospects of graphene, see Ref. [102]). These prospects are based on the peculiar properties of this material. Some examples are its extraordinary stiffness (interatomic bonds are harder than in diamond), a thermal conductivity at room temperature exceeding 5000 W/m/K and a high visible light adsorption despite its only atomic thickness. In the following, we will discuss some of the electronic properties of graphene in detail.

3.1.1 Electronic properties

Carbon allotropes exhibit a large diversity of electronic properties, owing exclusively to differences in their atomic structure. To understand graphene's peculiar electronic properties, it is instructive to begin this chapter with the lattice structure of graphene. The equations and annotations given in this section closely follow the textbook of M. I. Katsnelson [101] and the review by A. H. Castro Neto *et al.* [103].

The lattice geometry of graphene is depicted and discussed in Fig. 3.1. In short, the graphene crystal is formed by a hexagonal honeycomb lattice, where the C atoms are located in two equivalent sublattices. The ground state configuration of the carbon atom is $1s^2 2s^2 2p^2$. Arranged in a honeycomb lattice, this leads to formation of extremely robust σ (sp^2) bonds in the plane, which give rise to graphene's high stiffness. The fourth electron is located in the p_z orbital

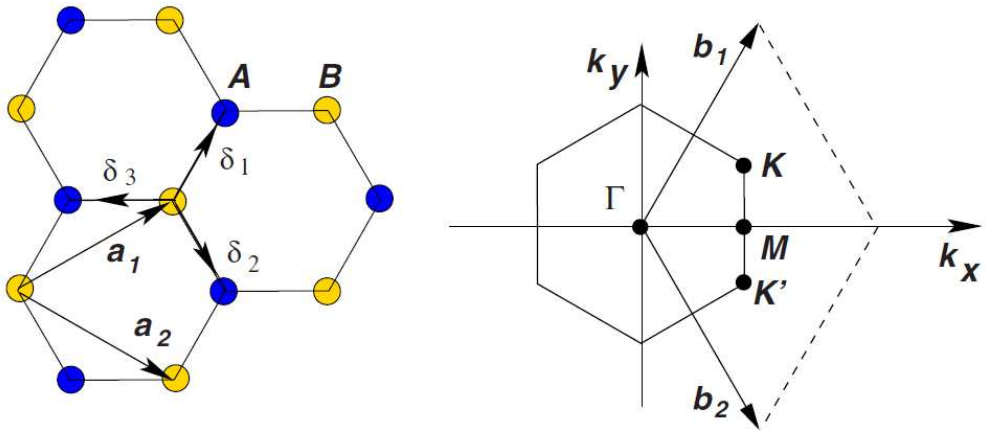

Figure 3.1: Structure of Graphene. - Visualization of the graphene honeycomb lattice from a top view in the left panel. Blue and yellow dots represent C atoms from the A and B sublattice, respectively. The lattice is spanned by two vectors $a_1 = \frac{a}{2}(3, \sqrt{3})$, $a_2 = \frac{a}{2}(3, -\sqrt{3})$ ($a \approx 1.42$ Å is the nearest-neighbor distance). Each C atom is connected to three nearest neighbors by the vectors $\delta_{1,2} = \frac{a}{2}(1, \pm\sqrt{3})$, $\delta_3 = -a(1, 0)$. The corresponding Brillouin zone (black solid line), including high symmetry points $K = (\frac{2\pi}{3a}, \frac{2\pi}{3\sqrt{3}a})$, $K' = (\frac{2\pi}{3a}, -\frac{2\pi}{3\sqrt{3}a})$, and $M = (\frac{2\pi}{3a}, 0)$ together with reciprocal lattice vectors $b_{1,2} = \frac{2\pi}{3a}(1, \pm\sqrt{3})$, is depicted on the right side. From [103].

perpendicular to the plane, and is entirely delocalized in the system. These π states are the only states available near the Fermi level, and therefore responsible for the electron transport. The peculiar shape of the π low-energy states can be derived from a simple tight-binding model.

A low-energy tight-binding model for graphene was already formulated in 1947 by Wallace [104]. A simple (spin-degenerate) Hamiltonian considers only the hopping of π electrons between neighboring sites, and between the next-nearest neighbors, that are located within the same sublattice:

$$H = -t \sum_{\langle i,j \rangle} \left(a_i^\dagger b_j + h.c. \right) - t' \sum_{\langle\langle i,j \rangle\rangle} \left(a_i^\dagger a_j + b_i^\dagger b_j + h.c. \right) \tag{3.1}$$

with t (t') the (second) nearest neighbor hopping, and a_i (b_i) the annihiliation operator for an electron in the A (B) sublattice. (Double) braces in the sum index denote summation over (second) nearest neighbors.

We first discuss the simplest case by allowing nearest-neighbor hopping only

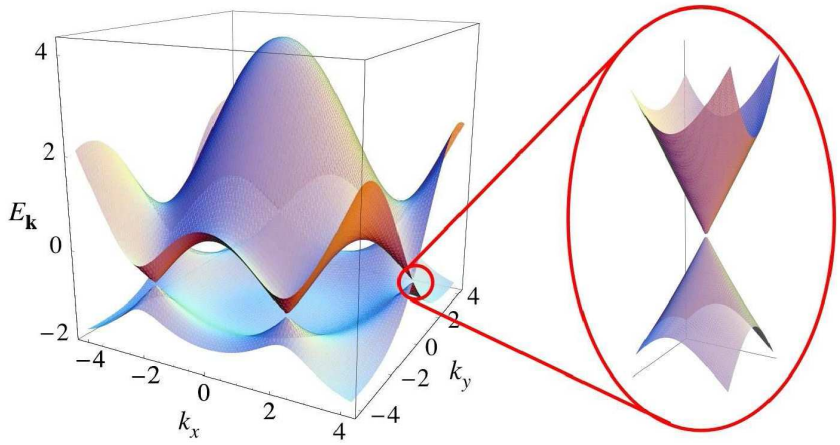

Figure 3.2: Band structure of graphene. - The plot shows the low-energy states of graphene of the tight-binding model with second-nearest neighbor hopping included. A close-up (inset) depicts the linear dispersion behavior around the K/K' point. From [103].

($t' = 0$). The Hamiltonian in reciprocal space then reads as

$$H(\vec{k}) = \begin{pmatrix} 0 & tS(\vec{k}) \\ tS^*(\vec{k}) & 0 \end{pmatrix}, \tag{3.2}$$

with $\vec{k}$ the reciprocal vector and

$$S(\vec{k}) = \sum_{\vec{\delta}} e^{i\vec{k}\vec{\delta}} = 2\exp\left(\frac{ik_x a}{a}\right)\cos\left(\frac{k_y a\sqrt{3}}{2}\right) + \exp\left(-ik_x a\right). \tag{3.3}$$

The Hamiltonian can be easily diagonalized, yielding an eigenvalue spectrum

$$E(\vec{k}) = \pm t|S(\vec{k})|, \tag{3.4}$$

very similar to the one shown in the inset of Fig. 3.2. The most striking feature of the graphene band structure is the linear dispersion behavior at the K and K' points. In undoped graphene, the Fermi level is exactly positioned at the crossing point, such that the valence band is fully occupied while the conduction band is entirely empty. Thus, π and π^* states touch in these single points only, and in this sense the system can be seen as a semiconductor with a vanishing band gap. In Fig. 3.2, the spectrum of the Hamiltonian 3.1 with non-zero t' is

shown. Switching on t' induces breaking of electron-hole symmetry, hence, an asymmetry between π and π^* states. This does not modify the shape of states close to the conical points but shifts the touching point away from $E = 0$ to $E = -3t'$. The parameters t and t' can be obtained from fits to first-principles calculations or from experiments. LDA calculations yield roughly $t \approx -3$ eV and $t' \approx 0.01 - 0.2t$, depending on the concrete choice of the tight-binding model [105].

The linear dispersion of low-energy states implies a chiral nature of graphene states. To understand why, we expand the nearest-neighbor Hamiltonian 3.2 near the K or K' point, to end up finally with a Dirac Hamiltonian,

$$H_K = -i\hbar\nu_{\mathrm{F}}\vec{\sigma}\nabla, \tag{3.5}$$

for low-energy states at the K point and $H_{K'} = H_K^T$ at K'. $\vec{\sigma} = (\sigma_x, \sigma_y)$ is a vector of Pauli matrices. If both sublattices and valleys are considered, the Hamiltonian is composed of 4x4 matrices. We choose an appropriate basis

$$\Psi = \begin{pmatrix} \Psi_{K\mathrm{A}} \\ \Psi_{K\mathrm{B}} \\ \Psi_{K'\mathrm{B}} \\ -\Psi_{K'\mathrm{A}} \end{pmatrix}, \tag{3.6}$$

where the component contains two indices, the valley index K, and the sublattice index. This basis set choice allows rewriting the Hamiltonian in a more symmetric form as

$$H = -i\hbar\nu_{\mathrm{F}}\tau_0 \otimes \vec{\sigma}\nabla, \tag{3.7}$$

with τ_0 the unit matrix acting on valley indices. The Hamiltonian of Eq. 3.5 can be identified with the Hamiltonian present in the massless Dirac equation of fermions. An important difference is the parameter ν_{F}, which replaces the speed of light c by a much smaller velocity: $\nu_{\mathrm{F}} \approx c/300$. Thus, low-energy electrons in graphene mimic the behavior of quasi-relativistic massless Dirac fermions and phenomena of relativistic quantum mechanics can be observed in graphene, such as the Klein tunneling. The term "massless" should not be mistaken for massless electrons in band structure theory: For graphene, a linear dispersion relation yields an effective mass of $m^* = \frac{1}{\hbar^2}(\frac{\partial^2\epsilon_k}{\partial k^2})^{-1} = \infty$.

The Hamiltonian 3.2 times a plane wave reads in momentum space as $H =$

$\hbar\nu_{\mathrm{F}}\vec{\sigma}\vec{k}$, with eigenfunctions around the K point given by

$$\psi_{\mathrm{e,h}}^{(K)}(\vec{k}) = \frac{1}{\sqrt{2}} \begin{pmatrix} \exp\left(-i\phi_{\vec{k}}/2\right) \\ \pm\exp\left(i\phi_{\vec{k}}/2\right) \end{pmatrix}, \tag{3.8}$$

where $\phi_{\vec{k}} = \arctan\left(\frac{k_x - K_x}{k_y - K_y}\right)$ denotes the polar angle of k vectors around the K point. The positive and negative signs correspond to π^* and π states, thus, states with positive and negative energy (electrons and holes): $E = \pm\hbar\nu_{\mathrm{F}}k$. Analogously, around the K' point,

$$\psi_{\mathrm{e,h}}^{(K')}(\vec{k}) = \frac{1}{\sqrt{2}} \begin{pmatrix} \exp\left(i\phi_{\vec{k}}/2\right) \\ \pm\exp\left(-i\phi_{\vec{k}}/2\right) \end{pmatrix}, \tag{3.9}$$

for the Hamiltonian $H = \hbar\nu_{\mathrm{F}}\vec{\sigma^*}\vec{k}$. States at K and K' are related by time-reserval symmetry, as can be seen from the Brillouin zone in Fig. 3.1. Let the origin of the reciprocal coordinate system be in the M point, then a reflection along the k_x axis is nothing else but a time reversal: $(k_x, k_y) \to (k_x, -k_y)$. The states given in Eq. 3.8 and 3.9 also include a Berry's phase, which means a negative sign for a rotation of $\phi_{\vec{k}}$ by 2π.

Now, we consider the projection of the momentum vector k on the spin in the same direction, which is here the pseudospin. From the definition of the helicity operator in quantum mechanics,

$$h = \frac{1}{2}\vec{\sigma}\frac{\vec{k}}{k}, \tag{3.10}$$

we can immediately see that $\psi_{\mathrm{e,h}}^{(K')}$ and $\psi_{\mathrm{e,h}}^{(K)}$ are eigenstates of h:

$$h\psi_{\mathrm{e,h}}^{(K)} = \pm\frac{1}{2}\psi_{\mathrm{e,h}}^{(K)}. \tag{3.11}$$

Hence, for both, electrons and holes, a definite pseudospin orientation can be found, which is positive (electrons) and negative (holes). Thus, Dirac states of graphene exhibit a well-defined chirality, which is not defined with respect to real spin of the electrons, but with respect to the pseudospin, and for low energies, where electrons and hole behave Dirac-like, the helicity is a good quantum number.

The quasi-relativistic and chiral nature of graphene's low-energy states manifests in numerous exotic phenomena. Some of them will be mentioned in the next subsection.

3.1.2 Dirac electrons: experiments and applications

Some remarkable consequences of graphene's quasi-relativistic electron behavior were discovered in transport experiments. The chiral nature of Dirac states leads to peculiar quantum Hall effects [106]. Fig. 3.3a shows the Hall conductivity σ_{xy} and Hall resistivity measurements as a function of carrier concentration. As in usual quantum Hall systems, electrons exposed to a magnetic field lead to equidistant plateaus in the conductivity with a distance of $\frac{4e^2}{h}$. However, a closer look shows the presence of a "half-integer" quantum Hall effect [3, 107, 108], namely, a finite conductivity at zero Landau level, and hence a shift of the series of Hall plateaus by one half: $\sigma_{xy} = \pm\frac{4e^2}{h}(N + 1/2)$.

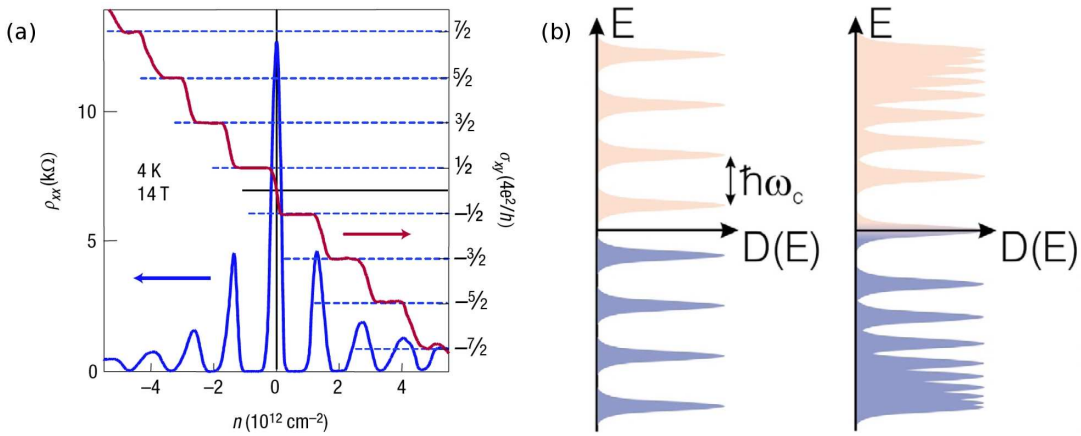

Figure 3.3: Anomalous Quantum Hall effect in graphene. - (a) Hall resistivity (blue) and conductivity (red) of monolayer graphene at 4K and 14 T magnetic field. (b) Scheme of Landau levels in usual Quantum Hall system with equidistant Landau levels (left) and graphene with square-root behavior (right). Adapted from Ref. [106] and [109].

The anomalous QHE can be understood from the Landau levels of graphene in a magnetic field. In usual quantum Hall devices, Landau levels are equidistant and do not exhibit a zero level (Fig. 3.3b (left)). In graphene, however, theory and experiment revealed a square root behavior of Landau levels [110, 111] and a level at zero energy:

$$E_N = \mathrm{sgn}(N)\sqrt{2\hbar v_{\mathrm{F}}^2 eB|N|/c}, \tag{3.12}$$

which is a consequence of the linear spectrum and the chiral nature of the Dirac states. The positive and negative sign in Eq. 3.12 denote electrons and holes, respectively. As a result, the density of states under a magnetic field is modified

according to Fig. 3.3b (right). Obviously, the zeroth Landau level is equally shared by electrons and holes, thus, contains only half as many states as the other levels. This half-degeneracy of the zeroth Landau level shifts the Hall plateaus in the conductivity. The anomalous QHE can be observed even in room temperature due to well-separated Landau levels at typical magnetic fields [112].

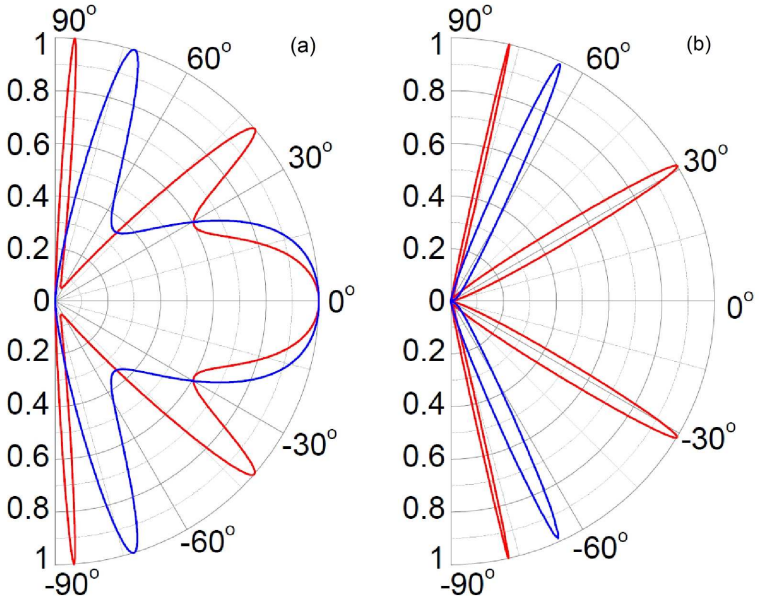

Figure 3.4: Klein tunneling in graphene. - (a) Example of transmission probability in monolayer (a) and bilayer (b) graphene as a function of the incident angle and for different barrier heights (blue and red curves). From [113].

A key phenomenon in transport experiments on graphene and graphene devices is the Klein tunneling [101]: This effect allows for high electron mobility [114] even in the presence of considerable disorder in graphene and suppresses Anderson localization. Briefly, the seemingly "paradox" Klein tunneling evokes a penetration of graphene's electrons through a potential barrier of arbitrary width and length with a probability of one for normal incidence [113]. Katsnelson *et al.* furthermore predicted "magic angles", again with total transmission [113], in monolayers as well as bilayers (Fig. 3.4). Later, Klein tunneling in graphene was confirmed experimentally [115, 116].

The Klein paradox is an obstacle for the development of graphene-based transistors [117]: typical field-effect transistor architectures are based on p-n-p or n-p-

n junctions. Electrons penetrating through this barrier (nearly) unhamperedly do not permit to switch the transistor efficiently to the off state (zero current). This is a main motivation for scientists to open a band gap in graphene. Band gaps in graphene can be generated in numerous ways, e.g., through strains, adatoms, or confinement in nanoribbons (cf. [101]). However, such modifications on graphene drastically degrade the electron mobility, or are impracticable to build stable transistors. Substantial advances have been made with heterostructures based on the combination of different 2D crystals, which will be discussed in Sec. 4.

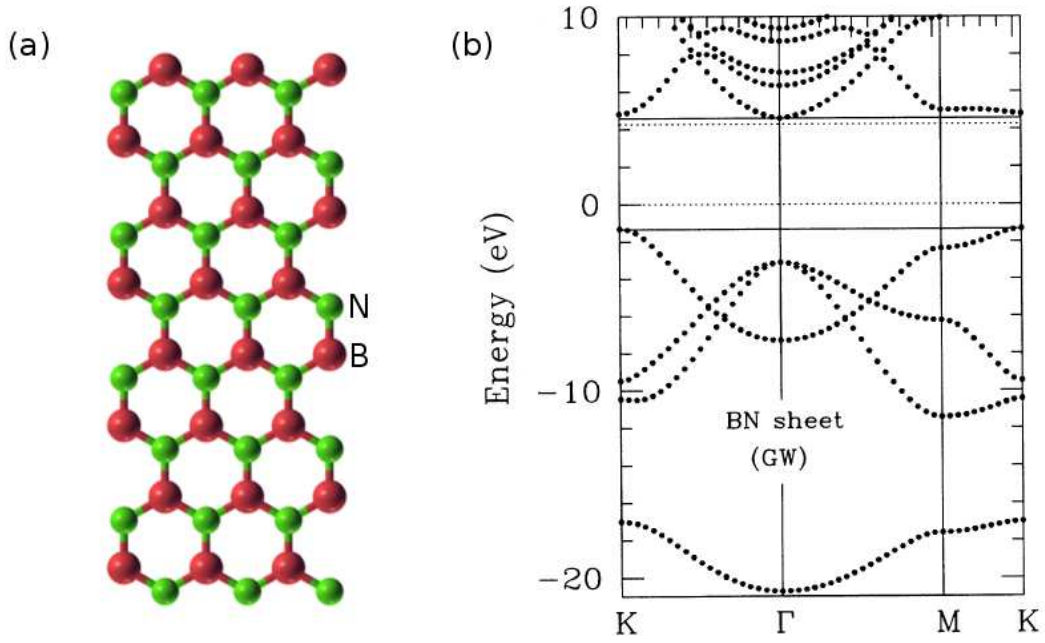

Figure 3.5: 2D h-BN. - (a) Structure of h-BN from a top view. Red atoms denote boron, green atoms nitrogen. (b) Band diagram of 2D h-BN calculated by the GW method (from [118]).

3.2 Hexagonal boron nitride

Hexagonal boron nitride (h-BN) is an isomorph of graphite. It consists of weakly bound layers of atoms in a hexagonal honeycomb lattice with strong sp^2 bonds and a lattice constant being only 1.8% higher than in graphene [119]. However, the sublattices in h-BN are chemically not equivalent due to an alternate occupation of lattice sites by B and N atoms. This results in an electronic structure completely opposite to graphene: Fig. 3.5b shows the GW quasiparticle

band structure of h-BN [118], which exhibits a large band gap of about 6 eV, in agreement with experiments [120]. The strong ionic bonds suppress formation of dangling bonds, and make the system relatively inert. As an atomically flat substrate, it is well-suitable for high-quality graphene devices [121]. In particular, its dielectric properties compare well with the standard substrate SiO_2 and even exceed its thermal conductivity by a factor of 600 [122]. First reports of graphene on h-BN substrates [121, 122, 123] initiated experimental progress in transfer techniques, that are nowadays used to create novel van der Waals heterostructures of materials such as graphene, h-BN, and many others.

3.3 Transition metal dichalcogenides: MoS_2 and others

The class of 2D transition metal dichalcogenides (TMDC) represents a number of different 2D materials with a rich diversity of electronic properties (see, e.g., reviews in Ref. [4, 124, 125]). These materials can be represented by the chemical formula MX_2, where M denotes a transition metal atom from element groups IV-VI (e.g., Ti, Mo, W) and X is a chalcogen (S, Se or Te) [124]. The structural similarity of many 2D TMDCs with graphene can be discerned in Fig. 3.6 (top view). However, in contrast to graphene and h-BN, the TMDC layer is constituted by vertically directed molecules (side view), yielding three planes per MX_2 layer: the transition metal atom resides in the middle plane and is surrounded by chalcogenide atoms below and above.

2D MoS_2 has been heavily investigated in the past few years, much more than its analogues WS_2, $MoSe_2$, WSe_2 [4]. These four systems exhibit very similar electronic properties, in particular, a direct band gap at the K point of the hexagonal Brillouin zone of 1-2 eV [126]. Although the layers in the bulk system are only weakly bound through van der Waals interactions, there are fundamental differences between the monolayer, the mulitlayer, and the bulk system. MoS_2, for instance, exhibits a band gap in the bulk of $\sim$1.2 - 1.3 eV, as can be observed in experiments [127] and density functional theory [128]. Upon going to the few-layer system, the band gap increases and reaches its largest value of $\sim$1.8 - 1.9 eV in monolayer MoS_2, where it becomes direct [127, 128]. Despite being successfully isolated already in 2005, together with a proof of the electric field effect [129], it attracted high attention only three years ago, when researchers presented a transistor made of a single-layer MoS_2 [130] with extraordinarily

high on-off ratios and room-temperature mobility.

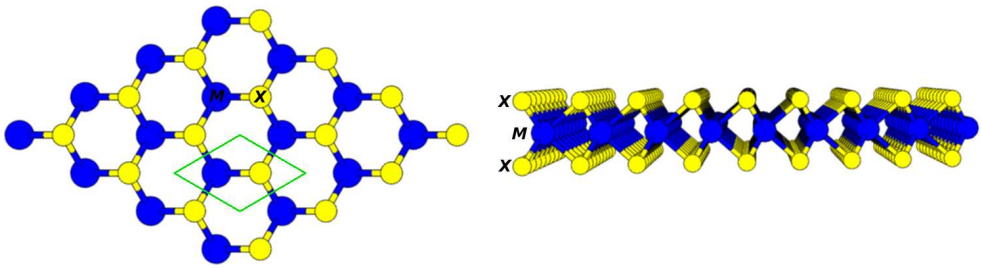

Figure 3.6: Structure of 2D TMDC. - Top view and side view. Blue atoms denote a transition metal M, yellow atoms a chalcogenide atom X. The unit cell is highlighted by green lines.

Recently, attention into isolated 2D TMDCs has been renewed due to the peculiar spin-orbit interaction in MoS_2, $MoSe_2$, WS_2 and WSe_2 [126]. These materials exhibit giant Rashba-like splitting of the conduction and valence states of up to $\sim$ 450 meV. This effect is again exclusively present in the 2D systems due to the absence of inversion symmetry. In contrast to the monolayer, inversion symmetry is present in the bulk and even in the bilayer system, leading to a suppression of the spin-orbit induced Rashba splitting in the multilayer case. Remarkably, two experiments have been recently reported, where this effect has been exploited [131, 132, 133]. With nanodevices based on MoS_2 monolayers, it is possible to store information not by means of the charge ("electronics") or the spin ("spintronics"), but through the wave number of the electron: by optical pumping, the electron number in energetically equivalent band structure "valleys" can be controlled, and a valley polarization of about 30% can be achieved [131]. Encoding information in a system by its valley quantum number forms a new class of electronic devices: valleytronics is the recently established term for this technology. Another material relevant for valleytronics is diamond [134], where electrons reside much longer within a valley (about 300 ns) than in graphene and even much longer than in MoS_2 (1 ns).

MoS_2, WS_2, $MoSe_2$ and WSe_2, which are known to be stable in air, represent only a small fraction of the vast familiy of 2D chalcogenides. Many more chalcogenides (such as $MoTe_2$, $ZrSe_2$) with van der Waals interaction between individual layers exist with not much being known about single-layer stability and electronic properties [4]. The general tendency seems to be that the most stable chalcogenides exhibit a band gap, while metallic (or superconducting) 2D

chalcogenides such as $NbSe_2$ and (Ta,Ti)S_2 seem to be unstable under ambient conditions, although possibly stable in an inert environment [4].

3.4 Other 2D crystals

The current library of available 2D crystals has constantly grown in recent years since the report of Novoselov *et al.* on the fabrication of 2D crystals [129]. Apart from graphene, h-BN and TMDCs, the class of 2D crystals encompasses a considerable number of different materials to this date, that are stable at ambient condition (at room temperature in air) [4]. This comprises graphene-like materials such as boron carbon nitride (BCN), and chemical derivatives of graphene, such as stoichiometric flourographene, with large band gaps. Graphene can be reversibly hydrogenated ("graphane"), allowing for the tunability of graphene's electronic properties from the insulating to the fully recovered semi-metallic behavior [135]. Another important category of available 2D crystals is the one of 2D oxides, where micas, a commonly used graphene substrate [136], and BSCCO have been shown to survive in ambient conditions (see again [4]). Superconductivity in monolayers of BSCCO and other layered oxides is rarely investigated, as well. However, maybe even more promising with regard to superconductivity is the combination of all these 2D materials into novel heterostructures [4].

4

Heterostructures based on two-dimensional crystals

Despite the availability of a whole "zoo" of two-dimensional crystals, the controlled fabrication of layered van der Waals hybrid systems has only recently become feasible. It is nowadays possible to combine single or multiple sheets of graphene other two-dimensional materials such as MoS_2, WS_2, or hexagonal boron nitride (h-BN). This facilitates the "on demand" design of complex stacks (see Fig. 4.1), known as van der Waals heterostructures [4]. Van der Waals heterostructures open a new sub-area in the research on 2D materials and pave the way for novel electronics. Remarkably, some graphene-based heterostructures have already been proven to be applicable as multifunctional devices. Apart from applications, these "materials with tailored properties" [137] exhibit a considerable number of interesting physical phenomena.

The foundation for research on 2D heterostructures was laid by the first interfaces of graphene with h-BN substrates, reported only in 2011. Experiments showed that graphene deposited on a h-BN substrate provides a significantly higher sample quality than on a standard insulating SiO_2 substrate, increasing the electron mobility comparable to those of free-standing graphene [121]. This is because the planar surface structure of h-BN suppresses a buckling of the graphene layer, and, unlike in SiO_2, dangling bonds and charge traps are absent in h-BN. The overall degree of substrate-induced disorder is reduced in graphene on h-BN, which lowers perturbance of graphene's electrons from charge puddles formation [121, 138]. In fact, many-body effects in graphene remained concealed

in experiments until graphene/h-BN interfaces came up[1], due to the inevitable presence of substrate-related charge inhomogeneities.

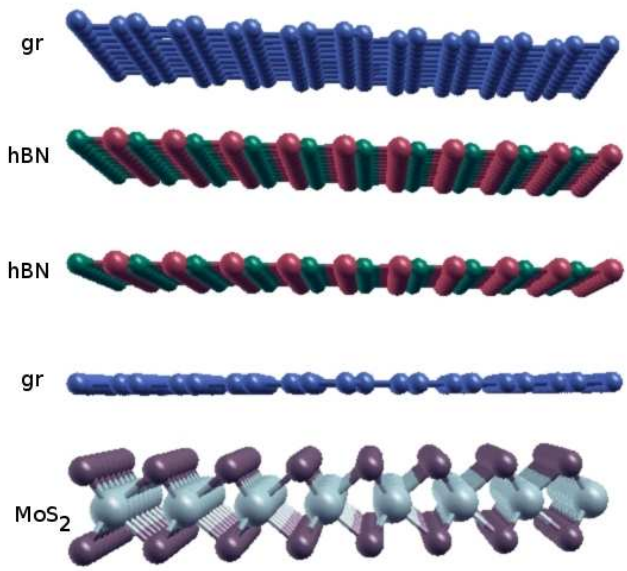

Figure 4.1: Example of a van der Waals heterostructure. - The image shows a hybrid made of graphene, h-BN and MoS_2.

A big step forward were the first experiments on graphene layers encapsulated between h-BN sheets [140, 141, 142], with a quality remaining at high level. Subsequently, tunneling transistors were reported. The functionality of these devices is based on vertical transport between two graphene sheets, which are separated from each other through dielectric tunnel barriers of h-BN, MoS_2, or WS_2 [7, 143]. The architecture of these vertical field-effect transistors permits efficient control of the electron transport in one graphene layer by gating the second graphene layer. The devices demonstrate the possibility to overcome the band gap problem of graphene transistors [1, 144] by offering a tunable tunneling DOS and on-off ratios of 10^6 at room temperature [7, 143]. Other applications of interest are photovoltaic devices based on graphene heterostructures (see Ref. [8, 145, 146] and Sec. 4.2.3).

Double-layer devices were built to explore a phenomenon of strong electron-electron interactions, the Coulomb drag [147]. To this end, electrically decou-

[1] An exception is free-standing graphene, where, e.g., reshaping of Dirac cones due to electron interactions was reported [139].

pled graphene sheets, separated by few dielectric spacers of h-BN, were investigated. The graphene layers in the heterostructure were separated by only about 1 nm, thus, at much smaller distance than typical characteristic distances between charge carriers in graphene. Indeed, carrier distances in graphene are known to diverge nominally proportionally to $1/\sqrt{n}$, where n is the carrier density. The double layer structures provide high degree of electric isolation between two graphene sheets despite spatial proximity and disclose unexpected behavior in the regime of strong Coulomb interaction [147]. Many more collective phenomena are likely to be revealed in the near future in double-layer devices and similar heterostructures.

Novel phenomena found recently their way into graphene physics due to the structural complexity of van der Waals heterostructures. For instance, graphene interfaced with h-BN leads to the formation of moiré superlattices, an issue that will be discussed in detail in this chapter. The presence of an additional long-range potential acting on graphene's Dirac fermions results in a cloning of Dirac cones at higher energy levels [148]. In combination with a magnetic field, the superlattice potential induces self-similar recursive spectra, called Hofstadter's butterflies [149, 150]. Superlattice potentials, although rather weak, can strongly affect electron states in graphene, which we show in Sec. 4.1.1.3. From theory point of view, sustainable progress in this field requires predictions of suitable heterostructures out of a nearly infinite number of material combinations, but this is not the only difficulty. Equally important is the careful identification of the interplay of effects and phenomena on different length scales, from the sub-Ångstrom to the mesoscale.

On this basis, we discuss in this chapter properties of graphene-based 2D heterostructures; in particular, the heavily investigated systems graphene/h-BN and graphene/MoS_2. Parts of the results presented here can be found in the original publications [119] (graphene/h-BN) and [145] (graphene/MoS_2), but in a less detailed form than in this chapter.

4.1 Graphene/h-BN heterostructures

4.1.1 Moiré superlattices in graphene/h-BN heterostructures

Early experiments on graphene deposited on h-BN substrates showed the formation of moiré superlattices [123, 138] and the absence of band gaps [121], in

contradiction to theoretical predictions [151]. In this section, we will bring in line experiment and theory and finally discuss our results in view of latest developments. To this end, we combine different model and first-principles techniques. For instance, forefront ACDFT-RPA calculations of van der Waals interactions will be joined with elastic continuum theory, or standard DFT with effective tight-binding models. In this way, we are able to describe the impact of defects, moiré superlattices and sublattice symmetry breaking on graphene's electrons.

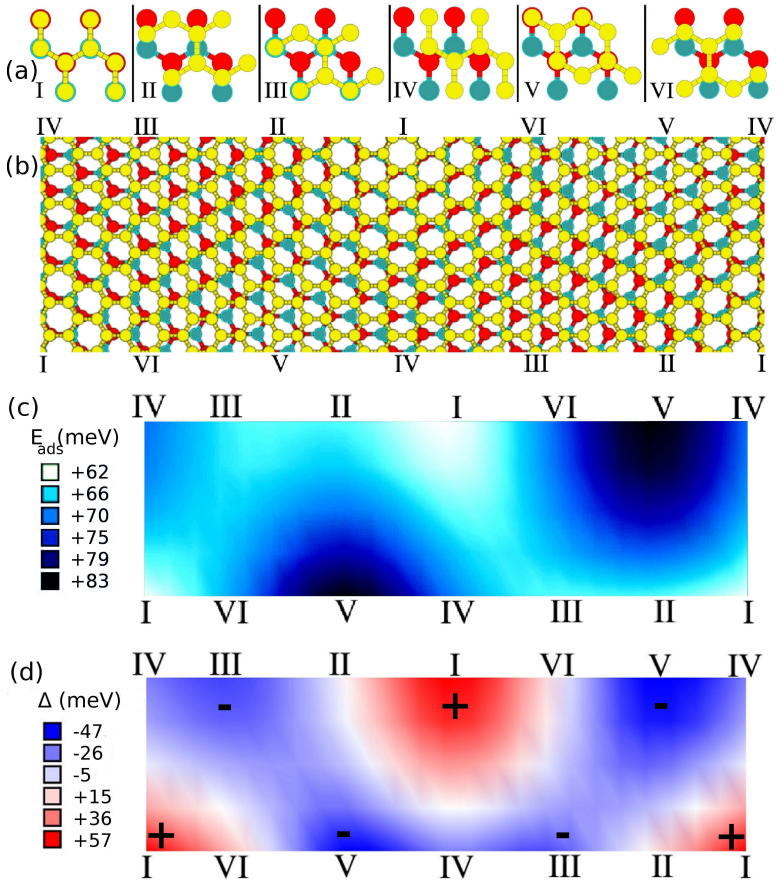

Figure 4.2: Moiré superstructures of graphene on h-BN. - (a) Different local stacking configurations (I-VI) considered from a top view. Yellow atoms indicate graphene carbon atoms, red and green atoms boron and nitrogen, respectively. (b) Visualization of the moiré superstructure with a reduced periodicity for clarity. (c) Adhesion energy landscape within the moiré. (d) The same for the local sublattice symmetry breaking.

4.1.1.1 Adhesion energy landscape in graphene/h-BN

The cohesive properties of layered materials, such as bulk counterparts of graphene and h-BN, are strongly anisotropic. The same holds for layered van der Waals heterostructures. While the building blocks of these materials, the isolated monolayers, exhibit mostly a high planar stiffness formed by strong covalent bonds, interlayer binding is rather weak and mainly of van der Waals-type. This leads to problems in the description of structural and elastic properties of these materials using DFT. Formulations for the exchange-correlation energy, such as commonly used local (LDA) or semi-local approximations (GGA), are well-suited to describe in-plane cohesion of atoms and molecules. However, interaction between layers, as being established by long-range correlations, is by definition not included in LDA/GGA, which calls for more sophisticated methods.

Here, we investigate the adhesive properties of graphene/h-BN hybrids (Fig. 4.2) by means of ACFDT-RPA total energy calculations (see also Sec. 2.7.1). The RPA energies will be used to evaluate adhesion energies of different stacking configurations (Fig. 4.2a) that occur within the moiré (Fig. 4.2b). The RPA method provides an accurate description of long-range van der Waals dispersion, but is also expected to cover electrostatic effects in the system due to polarized B and N atoms, and to take into account Pauli repulsion. All these effects were shown to be important for the adhesion in layered systems such as bulk h-BN [152]. For van der Waals solids, such as graphite and h-BN, the quality of ACFDT-RPA total energies is remarkably high, yielding excellent agreement between experiment and theory for interlayer distances, binding energies, and elastic constants [63, 64].

The total energies of the configurations I-VI as a function of the interlayer separation are plotted in Fig. 4.3 (technical details can be found in App. A.1). The energy curves exhibit minima for all configurations, thus, binding is preferred for all stacking arrangements. However, one can see different equilibrium separations between 3.30 and 3.55 Å. Configuration V is the strongest bound stacking with an adhesion energy of 83 meV/(2C-atoms) and an equilibrium distance of about 3.30 Å. In this configuration, one carbon atom sits above a boron atom, while the other C atom is located above the middle of a BN hexagon.

In contrast, the configuration with the highest energy minimum, thus, the lowest adhesion energy (62 meV/(2C-atoms)), is the one with both carbon atoms on top of a boron and a nitrogen atom, respectively, in a layer distance of 3.55 Å

(config. I). Interesting to note is furthermore that the adhesion of C atoms above BN bridge sites (above B-N bonds, configurations II and VI) yields higher binding energies. Configurations IV and VI are closest to the lowest-energy configuration V with adhesion energies of 71 and 70 meV/(2C-atoms). In configurations I and III, the negatively polarized N atom is covered by C atoms, thus, proximity of C atoms to the N atom diminishes the binding energy.

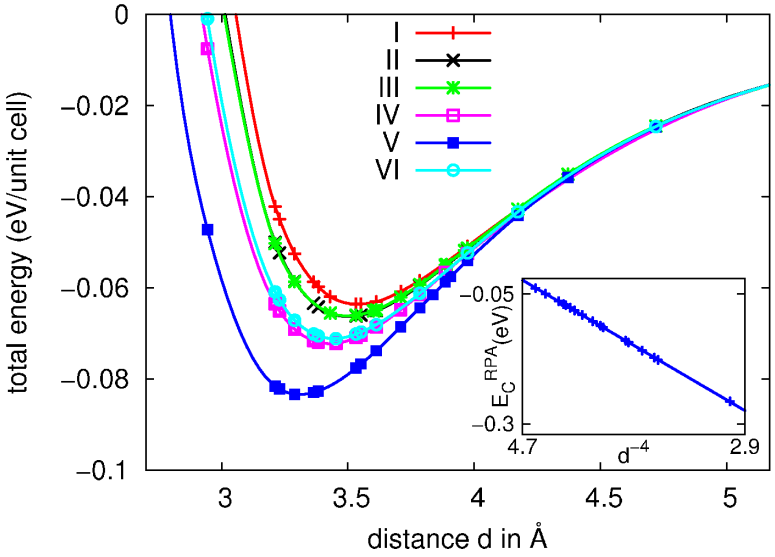

Figure 4.3: Different local stackings of graphene on h-BN - RPA total energies of the graphene/h-BN heterostructure as a function of the interlayer spacing d. The energy at infinite separation has been set to zero. (Inset) The RPA correlation energy relative to d^{-4} between 2.9 and 4.7 Å.

For larger distances, the configurations become energetically equivalent and exhibit a power law decay of $E_c \sim d^{-4}$ (see inset of Fig. 4.3). This indicates a bonding dominated by van der Waals interaction, because local effects would lead to an exponential falloff. The d^{-4} behavior is not a trivial consequence of the presence of London dispersion forces between graphene and h-BN. Assume a simple macroscopic system consisting of two parallel, non-interacting infinite plates with small thickness, which are sufficiently separated from each other. Then, "switching on" van der Waals interaction through a simple sum of R^{-6} terms of interacting elements leads to a standard d^{-4} decay of the vdW interaction energy. This is in agreement with our RPA result and thus seems to be sufficient insight into the van der Waals bonding mechanism. However, for layered nanostructures, the interaction is more manifold and R^{-6} summations can lead to qualitatively

wrong results for anisotropic nanostructures. In Ref. [153], analytic studies of the correlation energy in layered nanosystems were performed using the RPA, thus, without any assumptions on locality or presence of R^{-6} sums. The authors found that the simple macroscopic picture is only valid for gapped layered 2D systems (such as bulk h-BN) while it breaks down for other types of interfaces. Instead, the correlation energy follows $E_c \sim d^{-p}$ or has in some cases an even more complicated behavior. For instance, interfaces between 2D metals exhibit $p = 5/2$, and adhesion of two π-conjugated layers yields $p = 3$. The graphene/h-BN system represents an interface between a π-conjugated and a wide-gap insulator, which has not been studied before. The result of the d^{-4} behavior is important since many of the currently investigated 2D heterostructures are composed of (π-conjugated) graphene and gapped 2D crystals.

A comparison of the total energy curves with standard LDA and GGA confirms the importance of long-range correlations for the correct equilibrium layer distance, the binding energy and the asymptotic behavior. In Fig. 4.4 we plot total energies for LDA and GGA, which we benchmark by means of the high-quality RPA energies. For large separations, the LDA/GGA energies decay much faster than the RPA energies, which is expected because the dispersion is a long-range effect of non-overlapping densities, while correlations between overlapping states decay exponentially in the vacuum. There are also conspicuous differences between LDA and GGA. While LDA (see also Ref. [151]) reproduces roughly the equilibrium distance, GGA entirely fails to give a reasonable layer-layer distance and yields almost negligible binding energy. Although the GGA mostly represents an improvement over LDA regarding chemical bonds [32, 154], it obviously worsens the description of non-local van der Waals interaction in layered materials. The reason why LDA works much better than GGA [155] for weakly bound layered nanostructures is not obvious at first sight. The quality of LDA is rather accidental because errors in the exchange and the correlation energies cancel out spuriously, which is not the case in the GGA where density gradients are taken into account. It can be seen from Fig. 4.4 that the LDA binding energy of graphene on h-BN is underestimated by about 30%, which is in agreement with Ref. [63, 156], where LDA binding energies are shown to be systematically too low in graphite and in other systems [153], in contrast to the common belief that LDA effects an overbinding.

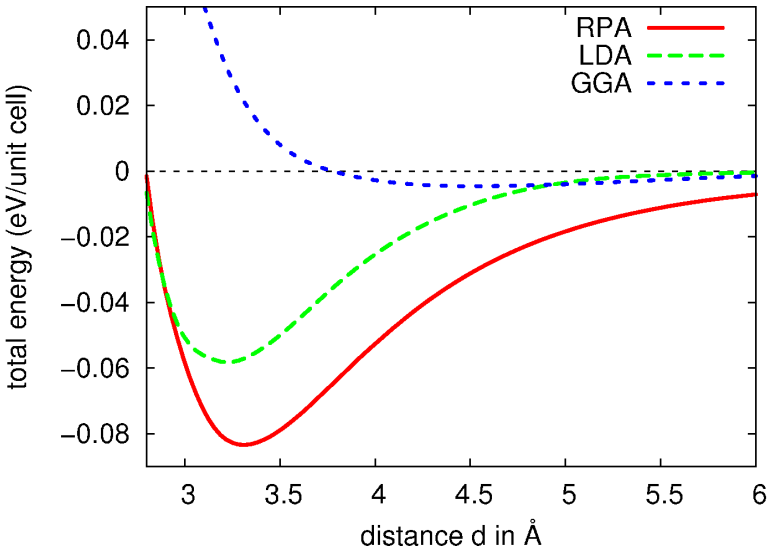

Figure 4.4: Comparison between RPA and (semi-)local functionals. - Total energies of configuration V as a function of the interlayer distance in the graphene/h-BN heterostructure as obtained from RPA, LDA, and GGA.

4.1.1.2 Stability of graphene/h-BN moirés

The RPA calculations provide insight into the strength of local interlayer binding in the graphene/h-BN hybrid, but immediately raise questions on the phenomenon of a moiré superlattice: why do stable moiré systems form when some stacking configurations are energetically more preferable than others, i.e., why is the whole heterostructure not in the lowest-energy configuration V? In particular, this question poses since the lattice mismatch, which has to persist in order to form a superlattice, is very small. We find it to be only 1.8 (LDA) and 1.9% (GGA). The lattice mismatch leads to large moiré periodicities of up to 13.5 nm, with the upper limit corresponding to the absence of relative layer rotations. This corresponds to a moiré unit cell covering the area of 55x55 graphene primitive unit cells. To judge the stability and existence of the moiré structure, elastic properties of the system must be taken into account. We focus on in-plane strains in the following, since the out-of plane corrugations of graphene and h-BN vary by about 0.2 Å (see Fig. 4.3), which is much smaller than the wavelength of the moiré. Elastic energies of the system are then to be compared to the adhesion energy landscape in the system (Fig. 4.2).

It has to be differentiated between two possible scenarios of adhesion: 1.

graphene on a h-BN substrate of considerable thickness, and 2. graphene on (free-standing) few-layer or monolayer h-BN. The first case has been realized in first experiments on graphene/h-BN, and they consistently confirmed the existence of moiré superlattices [123, 138, 157]. This is a consequence of the preserved lattice mismatch between graphene and h-BN. Obviously, the stability of the moiré arises from the high stiffness of graphene: since the topmost h-BN layers will most likely keep the lattice constant of the bulk, a compensation of the lattice mismatch would require a stretching of graphene by about 2% on the h-BN lattice constant. From the elastic properties of graphene, which are well-known experimentally [158, 159] and theoretically [160], it can be easily calculated that this would require 40 meV/(2 C-atoms). In contrast, the adhesion energy gain, that would be the result of the entire sample in the lowest-energy stacking V, is much smaller. Averaged over the six considered configurations, we find the gain to be only 14 meV/(2 C-atoms). Hence, strain energy penalties overcompensate adhesion energy gains, which preserves the incommensurate lattice configuration. This estimation is of course highly simplified; more subtle local strain effects can be found in graphene on h-BN substrate, which is discussed in Sec. 4.1.1.5. However, here we want to emphasize the differences between scenario 1 and 2.

The situation is different for the second scenario. If graphene sticks on a free-standing layer of h-BN, it is as well imaginable that the h-BN layer is slightly compressed towards the graphene lattice constant. To judge the possibility for this scenario, we investigate elastic properties of a h-BN sheet, which have been rarely studied in the literature. We start with basic elastic theory and derive in the following elastic constants based on LDA calculations. The elastic strain energy of a hexagonal system under uniaxial planar strain in x direction, u_{xx}, (hence, $u_{yy} = u_{xy} = 0$) reads as (see, e.g., [161]):

$$E_\mathrm{s}/A_0 = \frac{1}{2}\left(\lambda + 2\mu\right) u_{xx}^2, \tag{4.1}$$

with λ the first Lamé constant and μ being the shear modulus (2nd Lamé constant).

$$u_{\alpha\beta} = \frac{1}{2}\left(\frac{\partial u_\alpha}{\partial x_\beta} + \frac{\partial u_\beta}{\partial x_\alpha}\right) \tag{4.2}$$

is the linearized strain tensor with u_α the α-th component of the displacement vector $\vec{u}$; A_0 denotes the equilibrium unit cell area (for 2D h-BN, $A_0 \approx 5.3$ Å^2). The in-plane elastic properties are isotropic for hexagonal crystals, which defines

the 2D Young's modulus as [162, 163]

$$Y_{2D} = \frac{4\mu(\lambda+\mu)}{2\mu+\lambda}. \tag{4.3}$$

For a single-layer of h-BN, we obtain $\lambda = 59$ N/m, $\mu = 125$ N/m and $Y_{BN,2D} = 298$ N/m (LDA) and $\lambda = 54$ N/m, $\mu = 123$ N/m, $Y_{h-BN,2D} = 290$ N/m (GGA). $Y_{BN,2D}$ corresponds to a (bulk) 3D Young's modulus of $Y_{BN,3D} = Y_{BN,2D}/d \approx 0.9$ TPa (with $d \approx 3.3$ Å the interlayer distance). Y_{2D} and μ, as obtained from the full-potential PAW code VASP [164], are about 10% higher than calculations using Gaussian basis sets [165]. The in-plane stiffness of h-BN is remarkably high and only about 10-15% smaller than in graphene, where $Y_{gr,2D} \approx 340$ N/m [160].

Despite of the similar ultrahigh stiffness of both materials, the second scenario of graphene on a free-standing h-BN layer does not confirm the stability of moirés. Again, we compare elastic and adhesion energies, but here without fixing the h-BN lattice constant. First, we performed LDA simulations of the heterostructure entirely in stacking configuration V and varied the common lattice constant. We found a common lattice constant of 2.467 Å, which is in good agreement with our considerations of the total strain energy of the system, $E_{s,total} = E_{s,BN} + E_{s,gr}$, which exhibits a global minimum close to the LDA-derived lattice parameter. Importantly, the simultaneous compression of h-BN and tension of graphene leads to strain energy penalties of only 18 meV/(2C-atoms), which is considerably smaller than in the first scenario and comparable to the adhesion energy gains of 14 meV/(2C-atoms). Thus, it is possible that the moiré superlattice is not stable in this system and highly sensitive to the experimental environment. For instance, transitions of incommensurate to commensurate lattice matching are imaginable [166]. More experiments have to be done to investigate the delicate interplay of adhesion energy gains and strain energy penalties, for instance, through a systematic decoupling of h-BN layers from the bulk substrate or preparations of suspended h-BN with a graphene layer on top. The realization of a commensurate lattice in graphene/h-BN heterostructures would be of particular interest since this would lead to a spectral gap opening (see discussion below).

4.1.1.3 Band structure of graphene on h-BN substrate

In the previous sections, we have shown that graphene is weakly bound to h-BN through van der Waals forces. Despite this weak interaction, the electronic

states of graphene can be considerably modified, which is crucial for local spectral properties as well as mesoscopic transport. We investigate this issue in detail by a combined DFT and tight-binding study. We start with LDA calculations of the different local stacking configurations shown in Fig. 4.2 with enforced lattice matching. This requires only a small unit cell of 4 atoms (2 C, 1 B, 1 N; for technical details, see App. A.1.1.1). For the configurations I, III, and V, we find in good agreement with Ref. [151, 167] band gaps of 57, 34 and 47 meV, respectively. The configurations II, IV, and VI, which have not been studied elsewhere, yield lower, but still finite band gaps between 7 and 25 meV (see Tab. 4.1). Hence, at first sight, the conclusion of Ref. [151] that graphene on h-BN is gapped also in the moiré, seems reasonable. In contradiction, STM [121] and transport [138] experiments performed later could not confirm this conclusion and found the absence of a spectral gap. The mechanism behind must hence be more sophisticated.

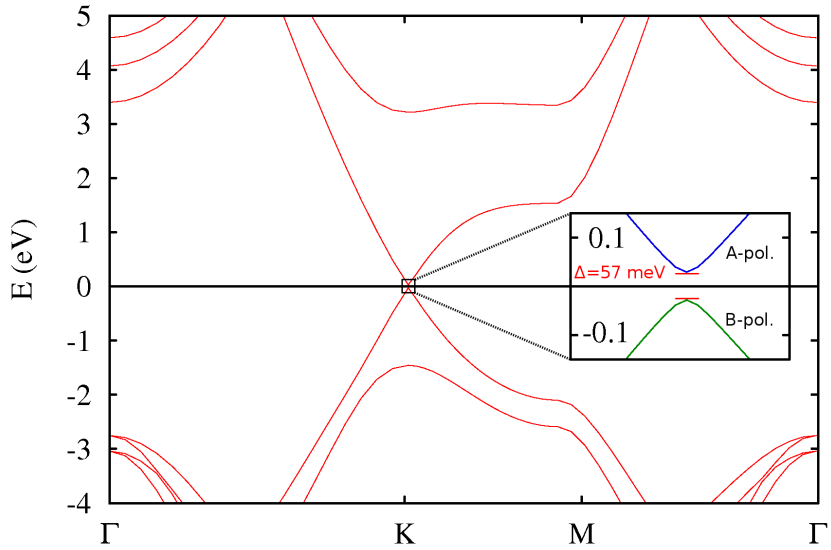

Figure 4.5: Band structure of graphene/h-BN in stacking configuration I (see Fig. 4.2) with enforced lattice matching. - The inset shows a zoom to the graphene p_z states at the K point. States close to the valence band maximum and the conduction band minimum are fully sublattice-polarized and exhibit parabolic dispersion.

To learn more about this, we take a closer look at the band structure of graphene on h-BN in the stacking order with the largest band gap, which is configuration I (Fig. 4.5). Around the Fermi level, one can discern graphene

p_z low-energy states with very similar dispersion as in the free-standing case, while h-BN states are far below -1 eV and above +3 eV. The modification of the p_z states becomes only visible in a close-up (see inset): one can find again the band gap of 57 meV, which is induced by the breaking of the sublattice symmetry, and furthermore, in agreement with Ref. [151], a parabolic dispersion of the states close to the K point. However, there is a detail which had been overlooked in previous studies, namely, a full sublattice polarization of the states around the gap. In the depicted configuration I, this means that p_z states close to the conduction band minimum are entirely localized in sublattice A, while those at the valence band maximum exist only in sublattice B. We will show in the following that this has important implications on the graphene electrons in a moiré potential.

In order to investigate moiré potential effects, one might try to perform an LDA calculation, including the entire superstructure of graphene on h-BN. Due to the lattice mismatch of 1.8%, this would however require a moiré unit cell of the size of 55x55 primitive graphene unit cells, thus, a cell containing more than 10,000 atoms, which would be out reach for standard DFT codes. Instead, we set up a minimal low-energy tight-binding model, which is not only much more efficient to solve, but also reproduces quantitatively graphene's low-energy states and allows for systematic studies by tunable parameters. For graphene on h-BN, we modify the simplest, nearest-neighbor tight-binding model of graphene electrons, as written in Eq. 3.1. Due to the large band gap of h-BN, we neglect h-BN states at high energies in our low-energy tight-binding model, since these can be integrated out. All effects of interlayer coupling are accounted for by effective potential energy terms acting on the carbon sites. These correspond to additional "mass" terms in the nearest-neighbor tight-binding Hamiltonian:

$$H = -t \sum_{\langle i,j \rangle} \left(a_i^\dagger b_j + h.c. \right) + \frac{1}{2} \sum_i \Delta_i \left(a_i^\dagger a_i - b_i^\dagger b_i \right), \tag{4.4}$$

where t denotes the nearest-neighbor hopping of graphene electrons, a_i (b_i) annihilates an electron in sublattice A (B), and Δ_i is the substrate-induced mass term acting on Dirac fermions. The moiré unit cell (n x n) is chosen as $\vec{a}_{n_{1,2}} = n\vec{a}_{1,2}$, whereby $\vec{a}_1 = a\,(1,0)$ and $\vec{a}_2 = a\left(-1/2, \sqrt{3}/2\right)$ are the lattice vectors of the primitive graphene unit cell with the corresponding lattice constant $a \approx 2.45$ Å. The mass term Δ_i is periodic with the moiré unit cell and $i = (l, m)$ defines the position in the moiré.

	I	II	III	IV	V	VI
Δ(meV)	+57	+7	-34	-25	-47	+14
$1-\tilde{t}/t$	0	0.010	0	-0.002	0	-0.010

Table 4.1: Band gap Δ and ratio of the two inequivalent nearest-neighbor hopping parameters $\tilde{t}/t$ with $t = 2.45$ eV in structures with broken trigonal symmetry. The average band gap is -4 meV.

By means of the different local stacking arrangements simulated in LDA, we determine constant hopping parameters $t = 2.45$ eV in regions I, III, and V through a fitting of the tight-binding energy dispersions to the LDA bands. In configurations II, IV, and VI, the Dirac cone turns out to be slightly shifted within the Brillouin zone away to the M point (IV, VI), or in the opposite direction (II). In this case, a second hopping parameter, $\tilde{t} \neq t$ is required to reproduce the *ab initio* low-energy bands (Tab. 4.1). The mass term Δ corresponds to the local band gap of graphene in configurations I-VI, and has the values as given in Tab. 4.1. These are extracted from LDA calculations of all six stacking configurations, and the different signs of the mass term Δ reflect the sublattice polarization. This builds up a local gap landscape as shown in Fig. 4.2d. For the sign of Δ, we use the following convention: states close to the valence band maximum entirely localized in sublattice B correspond to $\Delta > 0$, while the highest valence states localized in sublattice A refer to $\Delta < 0$.

The Fourier transformation of Δ_i to momentum space yields for the 0-th order Fourier component (for the reciprocal lattice vector $\vec{G} = 0$ only):

$$\Delta_{\vec{G}=0} = \frac{1}{N} \sum_i \Delta_i, \tag{4.5}$$

which is simply the average of all local mass terms in the moiré. The LDA calculations of stackings I-VI result in $\Delta_{\vec{G}=0} = -4$ meV, which is one order of magnitude smaller than the local gaps. As we will show in the following, the role of the 0-th order term is crucial for the presence of an absolute band gap in a moiré superlattice, where many more local stackings are realized than just the considered configuration I-VI. The modulation of the local gap landscape (Fig. 4.2d) can be approximated by a simple sinusoidally varying mass term

$$\Delta_i = A \sin(2\pi l/n + \Phi_1) + B \sin(2\pi m/n + \Phi_2) + C, \tag{4.6}$$

where A, B, C and $\Phi_{1,2}$ are constants. The constants are used as fitting parameters, such that Δ_i reproduces the local LDA mass terms Δ in regions I-VI. In this way, we obtain a Hamiltonian with all parameters derived from *ab initio* calculations. The full moiré is formed by a superlattice of 55x55 primitive graphene unit cells, hence, the Hamiltonian has dimensions $(2 \cdot 55^2, 2 \cdot 55^2)$ and can be diagonalized at low computational cost.

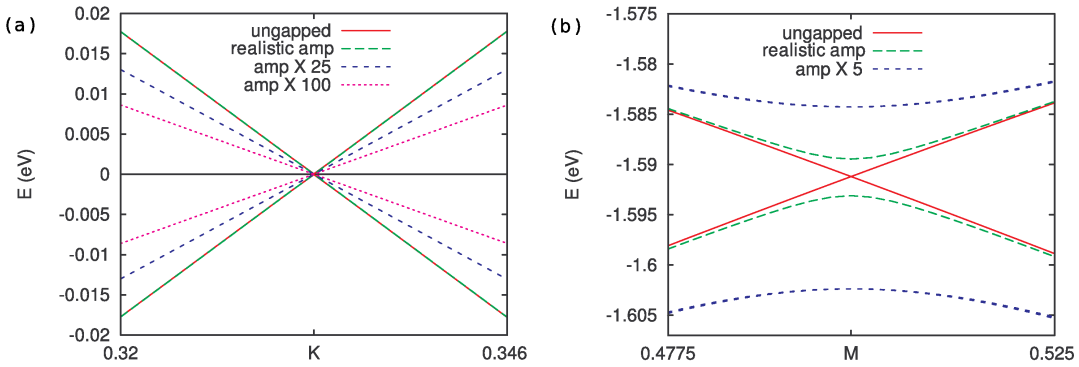

Figure 4.6: Graphene's energy bands according to Eq. 4.4 with $\Delta_{\vec{G}=0} = C = 0$ (a) near the Fermi level, and (b) below the Fermi level at the Brillouin zone boundary. - (a) Comparison for different amplitudes of the local gap landscape: *ungapped* case with all $\Delta_i = 0$, sinusoidally gapped graphene with *realistic* amplitudes as obtained from DFT, and artificially increased amplitudes (by a factor of *25* and *100*, respectively). One can see that no absolute gap opens. (b) The same for states at the Brillouin zone boundary. Minigaps open for finite amplitudes. The Fermi level is set to zero in both figures and a reduced moiré cell (20x20) has been used.

We first focus on states near the Fermi level in order to verify whether an absolute band gap in the moiré is opened or not. The states are shown in Fig. 4.6a. Here, the gap landscape as defined in Eq. 4.6 is simulated, with a vanishing average gap $\Delta_{\vec{G}=0} = C = 0$, but different amplitudes. First of all, one can see that the bands of the free-standing, thus, ungapped graphene ($A = B = 0$, such that $\Delta_i = 0\ \forall i$) coincide with the bands of the modulated system with realistic, *ab initio*-derived amplitudes. Hence, in the case of local gaps, which spatially average out, no absolute band gap opens, not even for much higher (unrealistic) amplitudes of the modulation. The only effect on states closes to Fermi level that we can find from the artificially increased amplitudes A, B, is a renormalization of the Fermi velocity, which is determined by the slope of the bands: $v_\mathrm{F} = \frac{1}{\hbar}\frac{\partial E}{\partial k}$. For amplitudes increased by a factor of 100, v_F drops down by about 50%. For

the realistic graphene/h-BN system, however, v_F remains nearly unaffected and is renormalized by less than 2% compared to free-standing graphene. This is very different from twisted graphene bilayers [168]. A difference between the free-standing graphene and the realistic graphene/h-BN system can be found at energies below E_F: Here, minigaps open at the Brillouin zone boundary (Fig. 4.6b). This effect had been observed for graphene on an Ir(111) surface, where likewise moiré patterns are observed [169, 170].

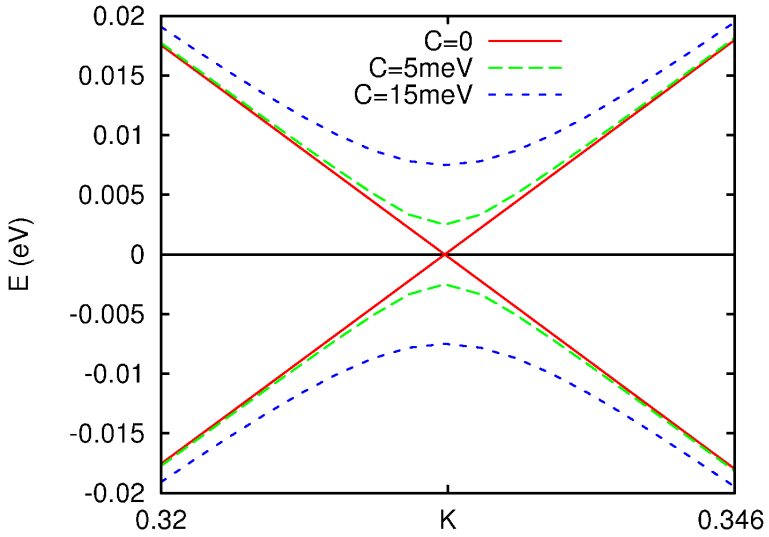

Figure 4.7: Graphene's energy bands according to Eq. 4.4 with $\Delta_{\vec{G}=0} = C$ near the Fermi level. - Comparison for different average gaps C in the local gap landscape: sinusoidally gapped scenario with *realistic* amplitudes A, B as obtained from DFT and different C. Gaps on the order of C open. The Fermi level is set to zero and a reduced moiré cell (20x20) has been used.

When a non-vanishing average gap $\Delta_{\vec{G}=0} = C \neq 0$ is present, the situation changes. The scenario is then analogue to our findings based on ab initio calculations as summarized in Tab. 4.1, where we obtain $C = -4$ meV. Fig. 4.7 shows the low-energy states of a *realistic* gap landscape, thus with realistic amplitudes of the modulation. Besides the ungapped case ($C = 0$, red bands), states for $C = 5$ meV (green dashed line) and $C = 15$ meV (blue dotted line) are plotted. We find that absolute band gaps on the order of C open which furthermore remain stable upon adding additional $\Delta_{\vec{G}\neq 0}$ terms. Artificial increase of the amplitudes A, B by orders of magnitude leads to a reduction of the absolute band gap, but it is not entirely closed. In summary, a realistic moiré pattern as shown in Fig.

4.2c exhibits locally varying band gaps with changing sign. In our tight-binding simulations, such a gap landscape leads to an absolute band gap very close to the spatial average gap, which we find to be small (-4 meV). Therefore, we expect the absolute gap to be at least one order of magnitude smaller than maximum local values $|\Delta|$, thus, a band gap below the sensitivity level in experiments. These results are in good agreement with STM [121] as well as transport [138] experiments.

4.1.1.4 Real-space shape of low-energy states

Local probe techniques, such as STM, are particularly suitable for the investigation of the moiré superlattice, as they allow for monitoring the behavior of graphene's electron states in real space with high resolution in the sub-Ångstrom regime. Simultaneously, large distances up to the mesoscale can be covered with an STM tip on a suitable sample. The topological behavior of states very close to the Fermi level is expected to be non-trivial, and, as will be shown in the following, highly sensitive to the parameter choice in the local gap landscape of Eq. 4.6. Fig. 4.8 visualizes the contribution of carbon atoms in a 20x20 moiré to the density of states in close proximity to the Dirac point, i.e., close below (a) and above (b) the Fermi level. Here, black dots denote atoms of sublattice A, and red dots show those of sublattice B, whereby their thickness depicts information on the distribution of the states in the moiré cell. This is done by choosing the dot size relative to the contribution of each atom to the state. Due to sublattice polarization (Fig. 4.5), we expect not only inhomogeneous spatial distributions of the state, but differences between A and B polarization in the real space shape of the states as well.

We first check graphene on h-BN with *realistic* amplitudes of the modulation, but a vanishing average gap, $C = 0$ (Fig. 4.8). Then, no sublattice polarization is present at all and states look equally distributed in space as in isolated graphene. In the Hamiltonian 4.4, isolated graphene corresponds to $\Delta = 0$, the fully ungapped case. Thus, for a vanishing average gap $\Delta_{\vec{G}} = C = 0$, no difference between fully ungapped and the realistically gapped graphene on h-BN can be observed because fluctuations of the probability density are virtually zero in all regions. The picture changes drastically when the amplitudes are artificially increased by a factor of 25 (Fig. 4.9). Here, states are localized in regions of low $|\Delta_i|$, although no absolute band gap opens. In these so-called "snake states",

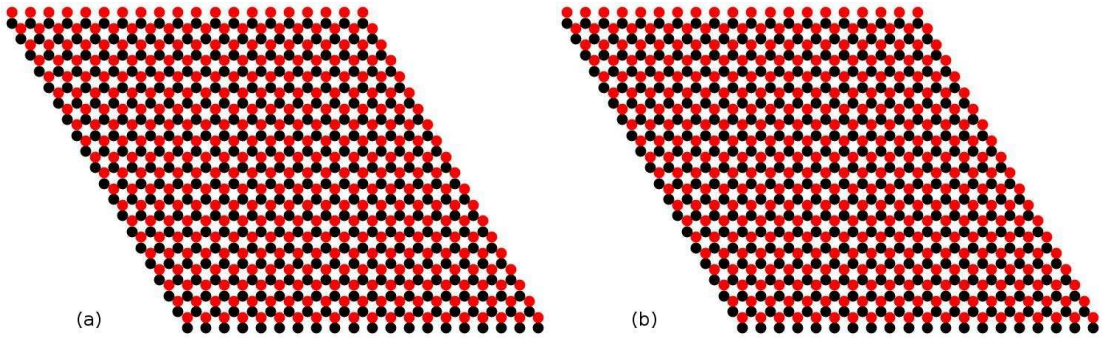

Figure 4.8: Real-space shape of low-energy states with realistic gap landscape and zero average gap. - The size of the dots (black: sublattice A, red: sublattice B) depicts the contributions to low-energy states in close proximity below (a) and above (b) the Fermi level. Here, the scenario of a gap landscape in a 20x20 moiré with *realistic* amplitudes A, B and a vanishing average gap $\Delta_{\vec{G}=0} = C = 0$ is presented. States are equally localized in sublattices A and B and homogeneously distributed within the moiré, yielding no differences to isolated (ungapped graphene).

both sublattices equally contribute to the states in any region of the moiré. The energies required to obtain the snake states are unrealistically high; nevertheless, snake states are experimentally not out of reach. The formation of snake states does not solely depend on the absolute value of the amplitudes A, B, but on the ratio of these compared to the energy, which is related with the periodicity of the moiré:

$$E_n \approx \frac{2\pi\hbar v_\mathrm{F}}{na}, \tag{4.7}$$

with n the size of the moiré (for unrotated moirés, $n = 55$, but here we consider $n = 20$ for visualization purpose). For 20x20 or 55x55 moirés, $E_n \approx 0.7$ and 0.3 eV, respectively, which is smaller than the amplitudes 25xA,25xB and the reason for snake shape of the wave functions near the Dirac point. On the other hand, if n is increased, $n = 100 - 200$, $A, B \approx E_n$ are in an intermediate state being on the same order of magnitude. Moiré periodicities of 100-200a could be reached by external strain, for instance. The case of Fig. 4.8 however with realistic amplitudes $A, B \ll E_n$ shows a nearly homogeneous distribution of low-energy states, which is in good agreement with STM experiments, where neither inhomogeneities in the LDOS nor a band gap were detected [123, 138].

For a non-vanishing average of the local mass terms ($C \neq 0$), the interplay of three energies constitutes the wave function behavior: the amplitudes of the modulation (A, B), the energy established by the moiré periodicity E_n, and the

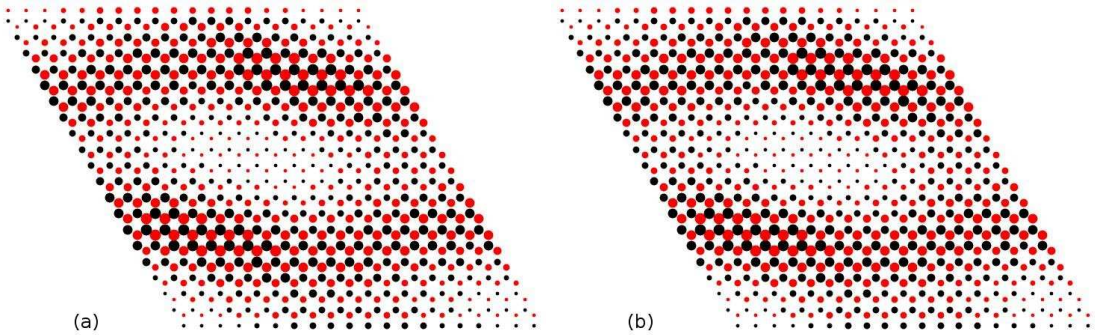

Figure 4.9: Occurrence of snake states - The same as shown in Fig. 4.8, but with a gap landscape with increased amplitudes 25xA, 25xB and a vanishing average gap $\Delta_{\vec{G}=0} = C = 0$. Snake states can be observed.

average mass term C. Fig. 4.10 shows the probability density in the moiré with *realistic* amplitudes, but a high average of local mass terms on the order of the amplitudes: $C = 50$ meV. In this case, states below and above the Fermi level are almost entirely sublattice polarized, which is not observed in experiments. However, our DFT calculations suggest a much smaller average gap of some meV ($\Delta_{\vec{G}=0} \ll A, B$). Then, realistically $\Delta_{\vec{G}=0} \ll A, B \ll E_n$ and it depends on the energy range chosen in experiments, whether or not sublattice-polarized states can be detected. For example, STM measurements of the LDOS should be performed in an energy range $E < \Delta_{\vec{G}=0}$, thus very close to the Dirac point. If $E > \Delta_{\vec{G}=0}$, which is most probably the case for small $\Delta_{\vec{G}=0}$, again homogeneous state distribution without any sublattice polarization would be measured as shown in Fig. 4.8, which is again in agreement with reported STM experiments. Finally, for $\Delta_{\vec{G}=0} \ll E_n \ll A, B$ no sublattice polarization would be measured, but snake states as shown in Fig. 4.9.

We thus conclude the most important facts of our electronic structure calculations: the moiré pattern evokes a small or even vanishing absolute (spectral) gap in experiments, and this leads to the homogeneous distributions of states in the moiré, which can be measured by STM. Phenomena such as snake states or Anderson localization depend on the interplay of average and spatially modulated mass terms and play a very important role when graphene is close to the charge neutrality point. Indeed, today's ultrahigh quality of graphene on h-BN substrates enables experiments close to the neutrality point. This allowed for the observation of Anderson localization in graphene/h-BN heterostructures, see

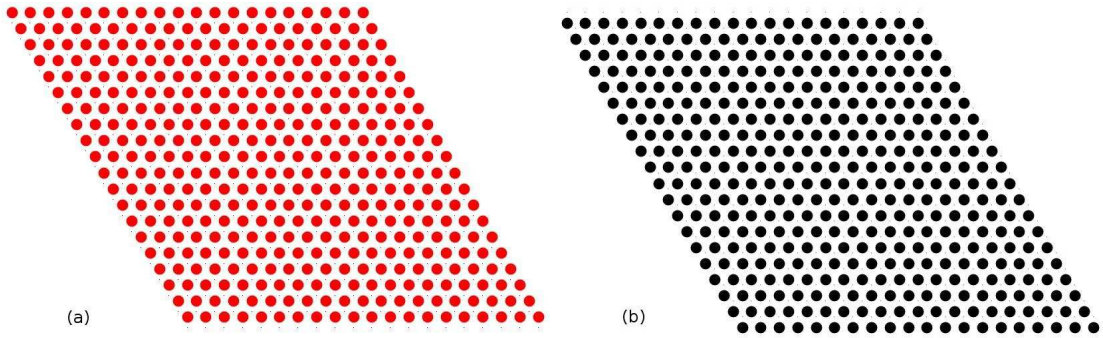

Figure 4.10: Non-zero spatially averaged gap: sublattice polarization. - The same as shown in Fig. 4.8, but with a gap landscape with *realistic* amplitudes A, B and finite average gap of $\Delta_{\vec{G}=0} = C = 50$ meV.

[141]. In the work of Ref. [141], experimentalists revealed an intrinsic metal-insulator transition in the heterostructure, which is hidden in usual conductors by the presence of electron-hole puddles. Screening out these charge inhomogeneities enabled a decrease in disorder which (non-intuitively) led to Anderson localization. Gaps with spatially changing sign have been reported in (Hg,Cd)Te quantum well structures [171]. The transport properties of these systems are controlled by the gap modulation and enable tuning into a topological insulator. We propose the same for the graphene/h-BN heterostructures: while we find that the heterostructure itself (as experimentally realized in different forms [7, 121, 123, 141, 142, 147, 150, 157, 172]) does rather not permit observation of snake states, suitable strains could be applied to manipulate the moiré periodicities to approach these.

During the time of writing up this thesis, it was discovered experimentally that many-body effects can play a significant role in rotated graphene layers on h-BN, which permits to tune the band gap over orders of magnitude by means of the rotation angle [150]. A corresponding many-body theory has been recently proposed [173]. The origin of the large band gaps is speculative but can be associated with moiré instabilities.

4.1.1.5 Elastic properties of graphene on h-BN

In Sec. 4.1.1.2, we estimated the stability of the moiré superlattice occurring in graphene/h-BN hybrid structures. The elastic constants of h-BN and graphene were shown to be comparable. In this simple picture, this should favor, in

the case of a fixed h-BN lattice, the formation of a moiré over a commensurate stacking. However, there are more interesting aspects regarding the elastic properties of moirés. Latest experiments reveal the existence of incommensurate-commensurate transitions, thus, regions where the graphene and the h-BN lattice are aligned [166]. This phenomenon might be the reason for discrepancies between experiments, where recently band gap formation was observed [150] in contrast to previous studies [121, 123, 138]. Also, due to the small lattice mismatch, subtleties such as local defects might play an important role in the heterostructures since they can locally modify the interaction between graphene and h-BN (see Sec. 4.1.1.6).

In the following, we reconsider the impact of the adhesion energy landscape in the moiré, now accounting for local modulations of elasticity and strain, which we neglected so far in Sec. 4.1.1.2. Local strains might possibly promote, in the case of relatively pristine samples, the recently observed commensurate-incommensurate phase transition of moirés despite the extraordinary stiffness of graphene [158, 160, 174, 175] and h-BN [119, 165]. Here, we focus on graphene sheets deposited on a h-BN substrate, with the topmost h-BN layer assumed in a fixed geometry and lattice constant.

The local modulation of interlayer binding within the moiré should have two effects: 1. It should lead to local variations of the elastic constants in c-direction, or, in other words, the rigidity of graphene sheets against decohesion from h-BN should vary within the moiré. For instance, in regions in the moiré of different binding, applying a constant stress in z-direction should be responded with different local strain.

Using the data from Fig. 4.3, we replot the total energy curves (Fig. 4.11) as strain energies as a function of the strain in c direction,

$$\epsilon = \frac{h - d_{\text{local}}}{d_{\text{local}}}, \tag{4.8}$$

whereby d_{local} is the local graphene/h-BN equilibrium distance and h the graphene/h-BN distance under strain of graphene along the c axis. By pulling up or pushing down the graphene layer, the local Young's modulus can be measured by standard contact-mode atomic force microscopy (AFM). In AFM experiments on graphene/h-BN heterostructures, it was shown that a local variation of the Young's modulus arises in the moiré, but no quantitative values of the Young's modulus or its relative modulation were given [166]. The local Young's modulus

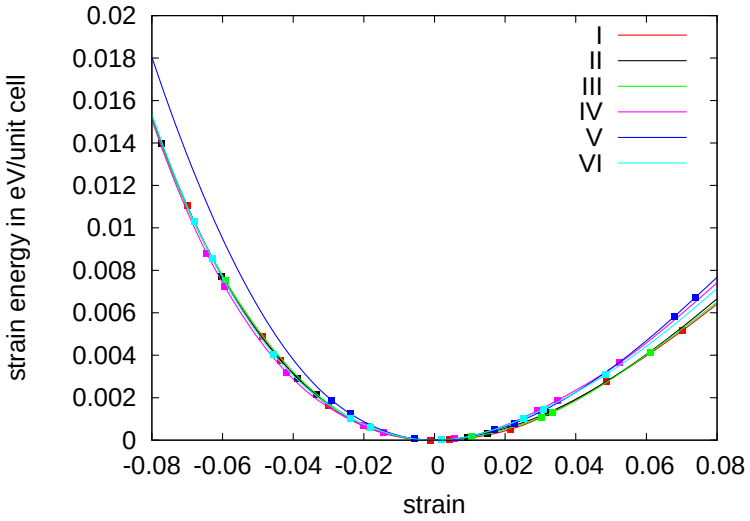

Figure 4.11: Strain energetics in different local stackings. - Strain energy E_{local} as a function of strain ϵ in different regions (I-VI) of the moiré.

can be defined as

$$Y_{\text{local}} = \frac{1}{A_0}\frac{1}{d_{\text{local}}}\frac{\partial^2 E_{\text{local}}}{\partial \epsilon^2}\Big|_{\epsilon=0} \tag{4.9}$$

with E_{local} the strain energy (per primitive graphene unit cell), ϵ the uniaxial strain, $A_0 = 5.3$ Å^2 the h-BN primitive unit cell area, and d_{local} the local graphene/h-BN equilibrium distance (between 3.3 and 3.55 Å). The Young's modulus is obtained according to Eq. 4.9 by a polynomial fit. There is strong compression-tension asymmetry visible in Fig. 4.11, which requires taking anharmonic terms into account. We find the highest Young's modulus in region V to be about $Y_{\text{local}} \approx 31.5$ GPa, while the lowest value is about $Y_{\text{local}} \approx 26.0$ GPa. These values are slightly lower than in graphite, where the Young's modulus in z-direction is about 37 GPa [176]. However, the variation of Y in the graphene/h-BN heterostructure is noticeably high (on the order of 10%). This leads to a modulation of the Young's modulus according to Fig. 4.12. The modulation is in qualitative agreement with the sinusoidal Y modulation observed in contact-mode AFM experiments [166], but slightly deviated due to the large modulus in region V.

2. The second effect of a modulated adhesion energy landscape is a generation of in-plane displacements of graphene atoms. These can be easily estimated to be small, but might be important for the observed incommensurate-commensurate

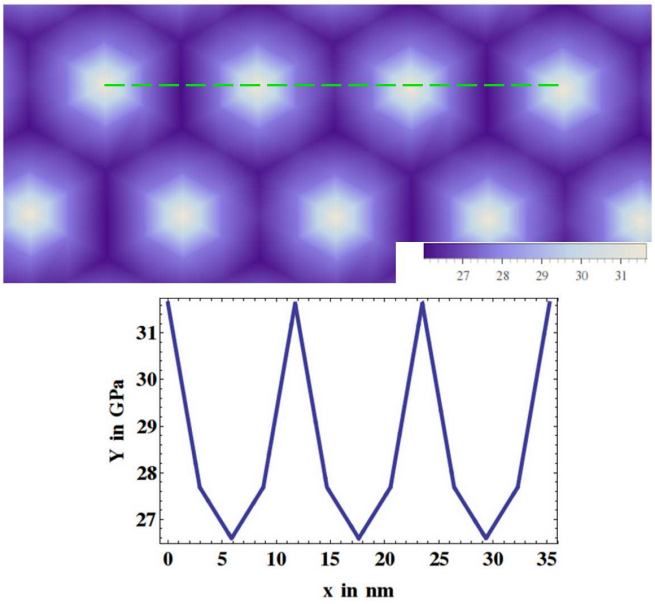

Figure 4.12: Local modulation of the Young's modulus in graphene on h-BN. - Upper panel: visualization of the Young's modulus according to Eq. 4.9. Lower panel: linescan of Y_{local} along the green dashed line.

transition in the system. Interestingly, experimental methods are well-developed to potentially scan for displacement fields in solids on the sub-pm scale [177]. Small displacement fields in the equilibrium state of the heterostructure can occur for two reasons: First, the corrugation of graphene on h-BN is 0.25 Å, as we have found from our RPA analysis of the interlayer spacings between 3.3 and 3.55 Å. The corrugation is distributed over large length scales of the moiré periodicity, about 13.5 nm for the unrotated system, and therefore, resulting planar deformations are negligible. Assuming a corrugation of 0.25 Å within, say, 1/4 of the moiré periodicity, we end up with planar displacements in graphene of much less than 0.01 pm per graphene primitive unit cell.

Another source of in-plane displacement fields originates from the presence of lateral forces. As shown in Fig. 4.2c, the potential landscape induced by the substrate with periodicity of the moiré is modulated on an energy scale of 20 meV. In Sec. 4.1.1.2, we have shown that this potential is not sufficient to favor graphene stretching on the h-BN lattice constant. However, external forces in a thin 2D material must be compensated by local structural deformations. In the following, we will calculate the deformations of graphene from elastic theory.

Following the book of Katsnelson [101], the condition of local equilibrium under external forces (using Einstein summation) reads as

$$\frac{\partial \sigma_{\alpha\beta}}{\partial x_\beta} + f_\alpha^{(\nu)} = 0, \tag{4.10}$$

with $f_\alpha^{(\nu)}$ being the volume density of external forces and $\sigma_{\alpha\beta}$ the (symmetric) stress tensor. In hexagonal 2D crystals, elastic properties are isotropic [161] and we can make use of the stress tensor of isotropic media, which has the form [101]

$$\sigma_{\alpha\beta} = \lambda \delta_{\alpha\beta} u_{\gamma\gamma} + 2\mu u_{\alpha\beta}, \tag{4.11}$$

and is determined by the Lamé constants λ and μ (see also Sec. 4.1.1.2). $u_{\alpha\beta}$ is the strain tensor given in Eq. 4.2 and $u_{\gamma\gamma}$ the trace. For the system to consider here, we obtain two coupled linear partial differential equations (PDEs):

$$(\lambda + 2\mu) \frac{\partial^2 u_x}{\partial x^2} + (\lambda + \mu) \frac{\partial^2 u_y}{\partial x \partial y} + \mu \frac{\partial^2 u_x}{\partial y^2} = -f_x^{(\nu)}, \tag{4.12}$$

and

$$(\lambda + 2\mu) \frac{\partial^2 u_y}{\partial y^2} + (\lambda + \mu) \frac{\partial^2 u_x}{\partial x \partial y} + \mu \frac{\partial^2 u_y}{\partial x^2} = -f_y^{(\nu)}. \tag{4.13}$$

$f_{x,y}^{(\nu)}$ is the derivative of the binding energy landscape as shown in Fig. 4.2c. Both equations can be easily decoupled. However, we have to treat the PDEs numerically using discretized variables, and we want to avoid higher order derivatives. Using the spectral method, we find the discplacement field $\vec{u} = (u_x, u_y)$ which solves Eq. 4.12 and 4.13. The spectral method is well-suited here, since we have to deal with periodic boundary conditions, which naturally favors a Fourier series representation of the solution. The solutions are obtained using the finite difference method, with iterative updates of Eq. 4.12 and 4.13. We find very small displacements of maximally 0.1 pm, with the maximum values reached in moiré regions of large potential gradients (Fig. 4.13). The largest potential gradients are between the lowest-energy configuration V and configuration I, therefore, largest displacement fields are located in region IV. The displacements correspond to maximum values of (local) strains of $u_{\alpha\beta} \approx 10^{-3} - 10^{-4}$.

The strain tensor has four components, namely the normal strains u_{xx}, u_{yy}, and the shear strains $u_{xy} = u_{yx}$. Under suitable transformation, we can find a strain tensor with vanishing shear components, and two components that determine the "principal strain". The maximum principal strain (corresponding to the

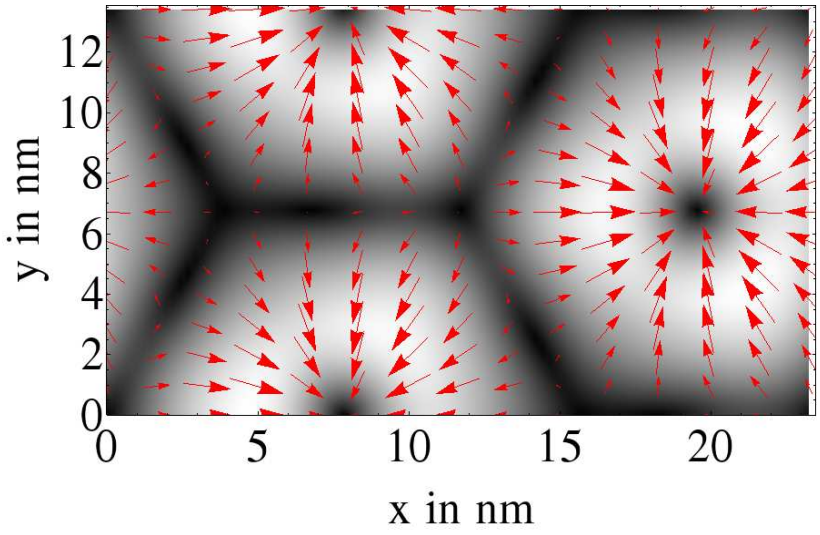

Figure 4.13: Displacement fields of graphene on h-BN. - Red arrows visualize the displacement field $\vec{u}$ as given by the potential landscape shown in Fig. 4.2 (full moiré). The background color denotes the magnitude of the displacement. Black color corresponds to $\vec{u} = 0$, white color denotes the maximum displacement of $|\vec{u}| = 0.1$ pm.

maximum eigenvalue of the tensor)

$$u_{\max} = \frac{u_{xx} + u_{yy}}{2} + \sqrt{\frac{(u_{xx} - u_{yy})^2}{4} + u_{xy}^2} \tag{4.14}$$

is visualized in Fig. 4.14.

Both, the displacement field (Fig. 4.13) and the Cauchy maximum principal strain exhibit a similar pattern owing to the hexagonal symmetry of the adhesion energy landscape. The planar strains in graphene on h-BN are very small, although possibly accessible experimentally. As a consequence, the local displacements will not noticeably affect graphene's p_z electrons. However, it can be speculated that the regions of maximum strain, despite being small, might play a role. The transition of the moiré lattice to a commensurate state, as observed in AFM experiments, means that graphene and h-BN adapt their lattice constants to the same value in large regions, while very narrow regions, domain walls, accumulate compensating strains. One can speculate that, in this scenario, the formation of domain walls is affected by the strain modulation shown in Fig. 4.13 and Fig. 4.14. The emergence of the commensurate-incommensurate transition [166] calls for additional theoretical efforts in this direction, especially by

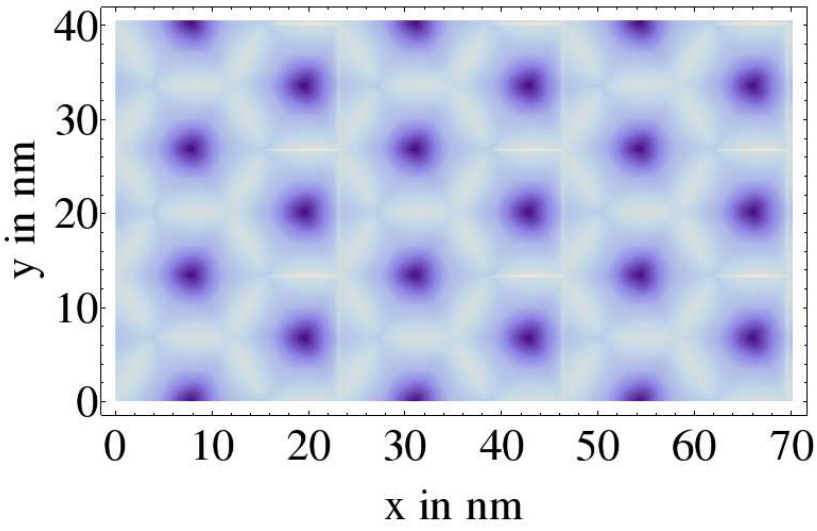

Figure 4.14: Cauchy maximum principal strain in the moiré. - Bright colored areas denote regions of high principal strain. The maximum values are less than 10^{-4}.

means of first-principles methods. The main challenge to overcome, however, is the problem of phenomena interacting on multiple length scales.

4.1.1.6 Graphene on defective h-BN

As has been discussed in Sec. 3.2 and throughout this chapter, the h-BN substrate provides excellent surface quality, atomic flatness and low contamination. Nevertheless, impurities are inevitably present in h-BN crystals, and, despite possibly low concentrations in the graphene/h-BN heterostructure, it is worthwhile to investigate their impact for numerous reasons. At this early stage of studies on graphene-based heterostructures, not much is known about impurity effects from experiments (some speculations about field-effect transistors can be found below). On the theory side, impurity studies were mostly concentrated on isolated graphene sheets, see, e.g., Refs. [178, 179, 180, 181, 182] for *ab initio* studies of various adsorbates. Impurities in graphene heterostructures have been rarely studied so far, with some exceptions [183, 184]. Also, their appearance is manifold, since the fabrication of hybrid structures comprises different possibly defective crystals. Above all, typical fabrication methods, such as the dry transfer technique [140, 141], might cause increased defect concentrations. Besides various impurity types being imaginable, such as antisite defects or oxygen atoms, it was

recently supposed that significant concentrations of carbon atoms are present in h-BN [185].

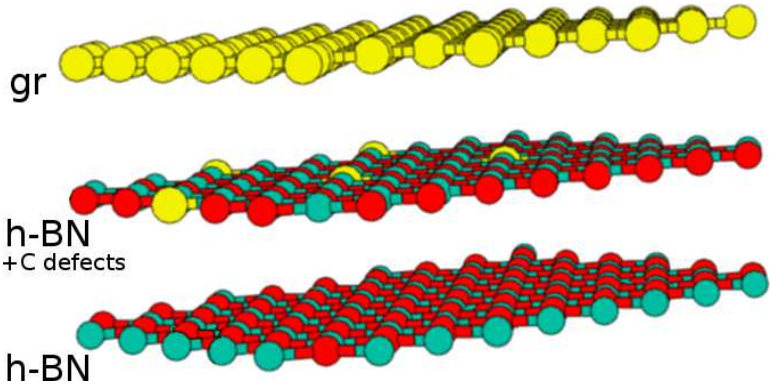

Figure 4.15: Graphene on defective h-BN. - The figure shows the simulated system with carbon impurities in the topmost h-BN layer.

To explore the impact of defective h-BN on graphene electrons, we set up a minimal tight-binding model of graphene's low-energy states in the spirit of Eq. 3.1. Here, we take all states associated with h-BN and defects therein into account using the following effective Hamiltonian:

$$H = H_0 + V\left(a_{i'}^\dagger o + h.c.\right) + \left(\epsilon_{\text{imp}} + \mu\right) o^\dagger o, \tag{4.15}$$

where an impurity orbital o with onsite energy ϵ_{imp} couples (w.l.o.g.) to a sublattice-A graphene atom at site $\vec{R}_{i'}$ via a hybridization V. H_0 is the nearest-neighbor tight-binding Hamiltonian of p_z electrons,

$$H_0 = -t\sum_{\{i,j\}}\left(a_i^\dagger b_j + h.c.\right) + \mu\sum_i\left(a_i^\dagger a_i + b_i^\dagger b_i\right), \tag{4.16}$$

with $a_i^\dagger$ ($b_i^\dagger$) the creation operator of a p_z electron acting on site $\vec{R}_i$ in sublattice A (B), and a hopping parameter t. The second term in both equations includes a chemical potential which is a constant term on the diagonal acting on all atoms, thus, a Fermi level shift. The parameters V, ϵ_{imp}, μ and t are *a priori* unknown. We will determine these in the following by connecting our effective tight-binding model with *ab initio* calculations. The tight-binding Hamiltonian provides a model-based insight into the defective heterostructure; moreover, determination of the model parameters from first-principles offers a quantitative picture of charge redistributions and allows for further processing in transport theory.

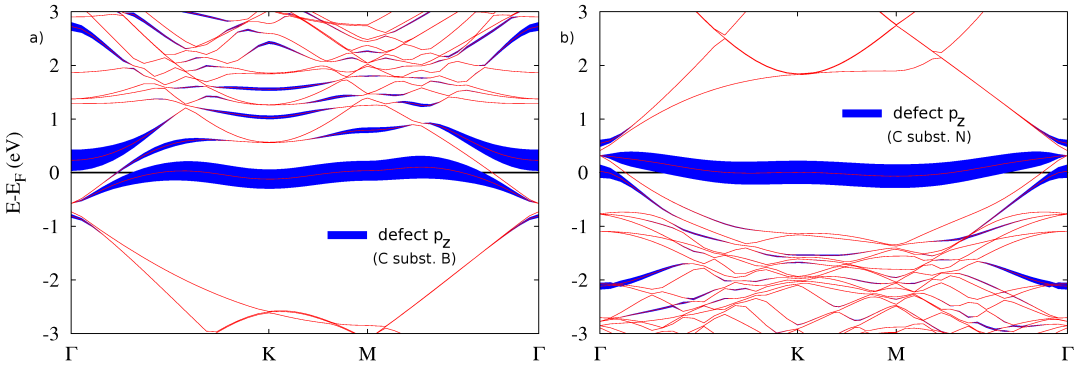

Figure 4.16: Band structure of graphene on defective h-BN. - The figure shows the case of a carbon impurity substituting a boron atom (a) and carbon replacing a nitrogen atom (b). Due to the 3x3 supercell, the Dirac cone is folded to the Γ point. The p_z character of the impurity state is visualized by blue fat bands.

Ab initio calculations were performed of the geometry as shown in Fig. 4.15. The supercell comprised a 3x3 layer of graphene on top of two h-BN layers, with one carbon substitutional atom in the topmost h-BN layer. A graphene/h-BN stacking arrangement according to configuration I was employed (Fig. 4.2). We simulated two scenarios, C substituting a B atom and C replacing a N atom (for computational details, see App. A.1.1.2). The supercell band structure reveals interesting features associated with the impurity (Fig. 4.16). First of all, the Dirac cone, which can be discerned at the Γ point (due to supercell-related Brillouin zone folding), is modified and shifted downwards for carbon impurities substituting boron atoms (a), while it is shifted upwards for carbon replacing nitrogen (b). With the carbon impurity, the h-BN layer contains either one additional electron or a hole, and due to Fermi level pinning, the graphene sheet is likewise n-doped (a) or p-doped (b).

However, the interlayer coupling does not only evoke a charge transfer. A modification of p_z states at the Dirac point can be observed as well that originates from the impurity states. The defect-p_z character of bands is visualized in Fig. 4.16 through the thickness of the blue fat bands [186]. Similar as many realistic adsorbates on graphene [180], the carbon impurity forms a pronounced midgap state as a consequence of the hybridization between the impurity and the graphene atom above. This effect is remarkable since the impurity is located within the neighboring h-BN sheet at a distance of about 3.35 Å, although it acts effectively as an impurity bound exclusively to graphene. The bands in Fig. 4.16 reveal

that the hybridization with graphene is stronger for a carbon defect substituting a boron atom and much stronger than for inert impurities (such as water molecules) adsorbing directly on graphene [179, 187]. However, compared to adsorbates being covalently bound to isolated graphene, hybridization is naturally weaker [180], which is supported by the nearly unmodified graphene/h-BN interlayer distance. The graphene atom above the impurity is only slightly shifted towards the h-BN layer by less than 0.01 Å for both defect sites.

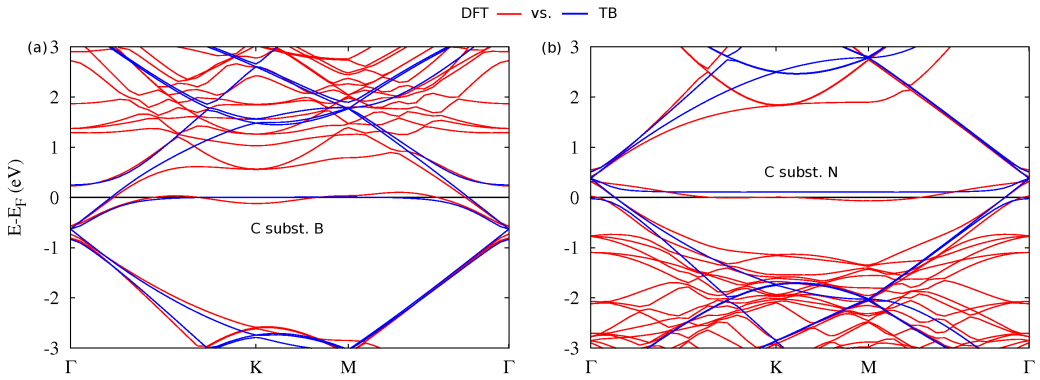

Figure 4.17: Comparison of band structures as extracted from TB model calculations and DFT simulations. - (a) A carbon impurity replaces a boron atom. (b) A carbon atom substitutes a nitrogen atom. Blue bands show the tight-binding bands as established by Eq. 4.15 with fitted parameters in Tab. 4.2.

Fig. 4.17 shows that mapping out an effective tight-binding model as defined in Eq. 4.15 yields energy bands in good accordance with the DFT-derived low-energy states. The fitted values of the used model parameters are summarized in Tab. 4.2. For comparison, $V \approx 0.9$ eV is about 20% of the hybridization of a methyl group with strong covalent bonding to graphene [180], and therefore considerably high. The parameters confirm that the carbon defect located in an empty boron site induces a stronger hybridization and Fermi level shift than in the nitrogen site.

Considerable deviations between tight-binding and DFT bands can only be found at higher energies far from the Dirac point due to the highly simplified model Hamiltonian. At the Dirac point, a small gap appears in the DFT bands, which is not reproduced by the tight-binding states. This is due to the enforced lattice matching of graphene and h-BN, which leads to gap opening. One might easily add a mass term in the spirit of Hamiltonian 4.4 to reproduce the small

	t (eV)	μ (eV)	V (eV)	ϵ_{imp} (eV)
C subst. B	+2.40	–0.63	0.91	+0.70
C subst. N	+2.40	+0.38	0.55	–0.28

Table 4.2: Parameters used for the tight-binding model (Eq. 4.15) as obtained by a fit to DFT bands. The boundary conditions employed were the same as in the DFT simulations (a 3x3 unit cell of graphene interacting with one defect per unit cell). No sign for V is given, because the resulting energy bands only depend on $|V|$.

gap opening. However, here we are interested in short-range scattering processes due to impurities, while the long-range moiré potential will decrease the gap to an even smaller value, as we have found in Sec. 4.1.1.3. It should merely be noted that the gap is slightly increased by some dozens of meV due to the defect midgap state.

But is the role of carbon defects indeed peculiar in a realistic graphene/h-BN hybrid with multiple impurities being present? We checked the effect of oxygen and antisite defects in h-BN. An oxygen defect substituting a nitrogen atom dopes graphene as well, but does not induce formation of a midgap state. Antisite defects significantly hybridize with graphene but are less likely to occur as indicated from cohesive energy calculations (App. A.1.2). Cohesive energies yield the highest stability for a carbon defect in a boron site, while the carbon atom substituting a nitrogen atom is as favorable as an oxygen atom in the same site. Least favorable are the antisite defects and the oxygen atom in a boron site. Only carbon defects in h-BN enable midgap state formation with a comparably high cohesive energy.

Formation of midgap states is potentially responsible for peculiarities of vertical transport in graphene/h-BN heterostructures. Experiments on field-effect transistors based on these heterostructures exhibit transport through vertical quantum tunneling [7]. In agreement with theory [188], carrier tunneling under an applied gate voltage is preserved even if the h-BN spacer has the thickness of multiple layers. However, experiments also show the presence of a small non-vanishing tunneling DOS in the absence of any gate voltages. This behavior was traced back to disorder-induced states close to the Dirac point [7], and midgap states represent a scenario consistent with the observed behavior. Hence, electron tunneling in vertical heterostructures might be mediated through "hot spots" such as carbon impurities in h-BN. The results call for future work in this

direction, proving the necessity of atomistic simulations in transport theory of graphene-based heterostructures.

4.2 Graphene/MoS_2 heterostructures

In this section, we investigate a hybrid system made of graphene covered with layers of the semiconducting material MoS_2. MoS_2 belongs to the class of transition metal dichalcogenides (TMDC, see Sec. 3.3). Heterostructures of graphene and TMDCs have attracted particular research interest since they facilitate the construction of novel, multifunctional nanodevices, such as memory devices [189, 190], or field-effect transistors (graphene/MoS_2 [7], graphene/WS_2 [143]). However, a microscopic understanding of the interface effects in graphene/TMDC heterostructures has been lacking so far, especially in the context of photovoltaic devices being recently reported [8, 146]. In particular, doping effects play a crucial role for the functionality of these devices. In collaboration with L. Britnell and K. Novoselov (U Manchester), we investigated doping mechanisms in the graphene/MoS_2 interface by a combination of first-principles calculations and photovoltaic measurements, which prove the applicability of the heterostructure for photodetection (see Ref. [145]). The results will be discussed in the following.

4.2.1 Interface properties and impurity doping

The properties of graphene and MoS_2 can be compared in Sec. 3.1 and 3.3. In contrast to h-BN, MoS_2 exhibits a lattice constant which exceeds those of graphene significantly. From DFT calculations, we find the lattice constant in isolated MoS_2 to be 23% larger than in graphene (for computational details, see A.2.1). Therefore, it is unlikely for MoS_2 and graphene to adhere in a commensurate stacking. In our simulations of the graphene/MoS_2 hybrid, we incorporate the lattice mismatch by setting up a supercell of a 4x4 MoS_2 layer on top of a 5x5 graphene sheet. In this way, graphene has to be strained by only few percent to conform with the MoS_2 lattice. Similar as for graphene/h-BN, we find a graphene-MoS_2 interlayer spacing of 3.35 Å, indicating a weak bonding of van der Waals-type, in agreement with Ref. [191]. The LDA to the exchange-correlation functional is sufficient for the following calculations, since it produces a reasonable equilibrium distance and we are interested in band structure effects.

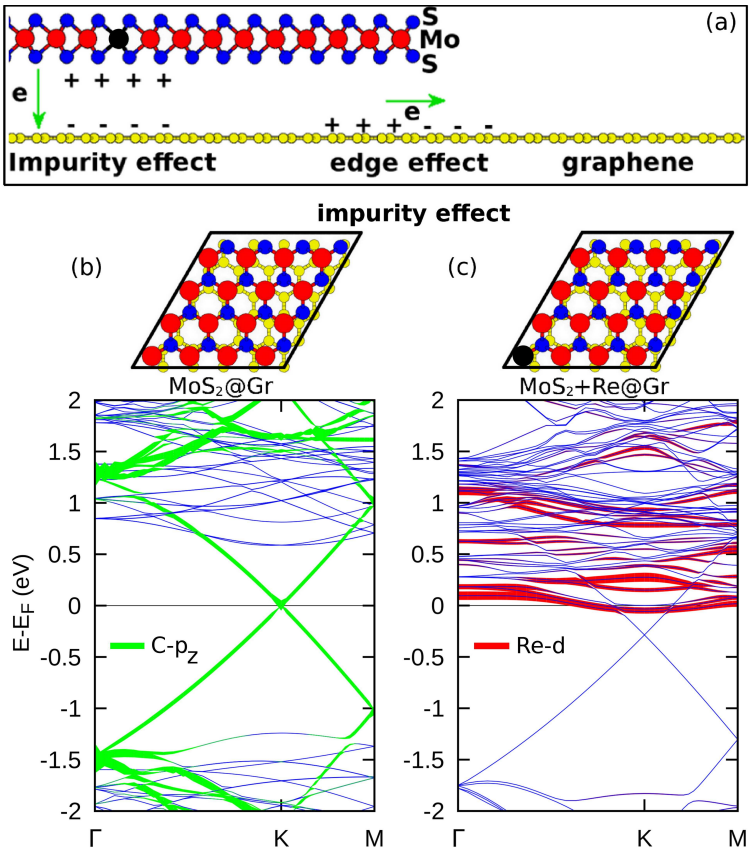

Figure 4.18: Simulated graphene/MoS_2 heterostructure. - (a) Side view of the graphene/MoS_2 heterostructure. (b) Band structure of graphene fully covered with pristine MoS_2. The unit cell used in the simulations is depicted in the upper panel. Green fat bands show the graphene p_z contributions to the bands. (c) The same for graphene fully covered with MoS_2, but one rhenium substituent in the MoS_2 (black atom). Red fat bands depict the Re d-orbital character of bands.

The considered system in our simulations is visualized in Fig. 4.18 (top panel). Here, we seek for possible doping mechanisms in the graphene/MoS_2 hybrid, or, to be concrete, in a graphene layer covered with a flake of MoS_2. To this end, we first investigate the pristine interface and the impact of defects, labelled "impurity effect" in Fig. 4.18 (top panel). In analogy to Sec. 4.1.1.6, where we discussed impurities in graphene/h-BN hybrids, we focus on defects in the insulating material, which is here MoS_2. To judge impurity effects on the system systematically, we compare in the following the band diagrams of the pristine and the impurity-contaminated graphene/MoS_2 hybrid.

The supercell employed in the DFT simulations, which comprises the 5x5 graphene layer below a 4x4 MoS_2 sheet, is shown in Fig. 4.18b. Due to the weak interlayer binding, structural modifications within the graphene and the MoS_2 layer are virtually not present. The electronic band structure (Fig. 4.18b) confirms the weak interaction between the layers: the graphene Dirac cone, which can be discerned at the K point, is obviously preserved under MoS_2. Furthermore, the Dirac point is perfectly aligned with the Fermi level, thus meaning no doping of graphene by pristine MoS_2. This is in contrast to graphene on substrates such as SiC, where an intrinsic doping is observable [192, 193]. Compared to isolated graphene, a MoS_2 effect on graphene's low-energy electrons is barely visible. A small band gap of some meV is opened, which is negligible and does not limit electron mobility significantly. We attribute the gap to a local sublattice symmetry breaking, similar as for graphene/h-BN moiré superlattices (see 4.1.1.3). Also the Fermi velocity of Dirac states remains unaffected.

In recent years, endeavours were made to induce large spin-orbit coupling in graphene. Crucial here is the large Rashba-type splitting of the MoS_2 valence and conduction bands (see Sec. 3.3), which might induce a spin-splitting of graphene's energy bands. In isolated 2D MoS_2, theory predicts a spin-splitting of 150 meV [126]. In similar transition metal dichalcogenides, even values of up to 450 meV have been reported (Sec. 3.3). We tested the effect of the 2D TMDC with the largest spin-splitting, WSe_2, on the band structure of graphene. For the Dirac states, we found the spin-splitting at the Dirac point to be not more than 2 meV, due to the low hybridization of graphene and WSe_2. In interfaces of graphene and MoS_2, spin-splitting in graphene is even lower.[1] A reduced interlayer distance would be required to achieve a larger splitting for applications, such as spintronic devices.

As a first result, graphene fully covered by pristine MoS_2 is unmodified in its atomic and electronic structure. However, the situation can change if impurities are present in the system. X-ray photoelectron spectroscopy (XPS) measurements of our experimental colleagues yielded a significant amount of oxygen in the heterostructure. Their impact on graphene electrons is not significant, which is shown in App. A.2.2. The same holds for sulfur vacancies. However, various kinds of impurities exist in molybdenite crystals, certainly below the XPS sensi-

[1] Since we are interested in impurity effects on graphene bands, spin-orbit interactions were therefore neglected in the band structure calculations depicted in Fig. 4.18.

tivity level. It is known that rhenium (Re) defects are naturally present within MoS_2 [194, 195]. These occur as substituents by replacing a Mo atom. In our simulations, this is incorporated in the unit cell as shown in Fig. 4.18c. The setup with one defect per supercell corresponds to a high impurity concentration of $7.6 \cdot 10^{13}\text{cm}^{-2}$.

The Re impurity affects only marginally the atomic structure of its environment. We find virtually no distortions of neighboring atoms in the MoS_2 layer (< 0.02 Å). Moreover, the interlayer binding between graphene and MoS_2 turns out to be unchanged, with the same binding energy and interlayer distance as in the pristine system, indicating a preserved low hybridization between graphene atoms and MoS_2 molecules. However, in contrast to the geometry, the electronic structure of the system is widely modified under the presence of Re impurities. This is depicted in Fig. 4.18c. First of all, one can see that the Dirac cone is now located below the Fermi level. The Fermi level is shifted upwards by 0.29 eV, corresponding to an n-type doping of graphene by $0.8 \cdot 10^{13}$ cm^{-2}. While the Dirac bands otherwise look unaffected, one can clearly see interesting effects near and above the Fermi level: Here, states associated with the Re impurity occur (red-colored fat bands).

To test for the effect of high impurity concentration, we simulated a four times larger supercell, thus, an impurity concentration of $1.9 \cdot 10^{13}$ cm^{-2}. Here, we found the Fermi level shift to be 0.27 eV, hence, an only slightly lower n-type doping. This indicates the saturation of doping for Re concentrations of 10^{13} cm^{-2}. At first view, such a Fermi level pinning does not seem unique for the heterostructure, since a similar doping mechanism was found for graphene on h-BN in the previous section with equally weak interlayer binding. However, in the graphene/MoS_2 hybrid, the distance between the Re impurity and the graphene is much (about 4.9 Å) higher due to the trilayer structure built by MoS_2 molecules. Atoms closest to graphene are the sulfur atoms, but these hybridize only weakly with graphene p_z orbitals, as can be seen from the sulfur vacancy calculations (App. A.2.2). Therefore, the conclusion that Re-contaminated MoS_2 dopes graphene despite of the far impurity-graphene distance and a weak van der Waals bonding, is rather surprising.

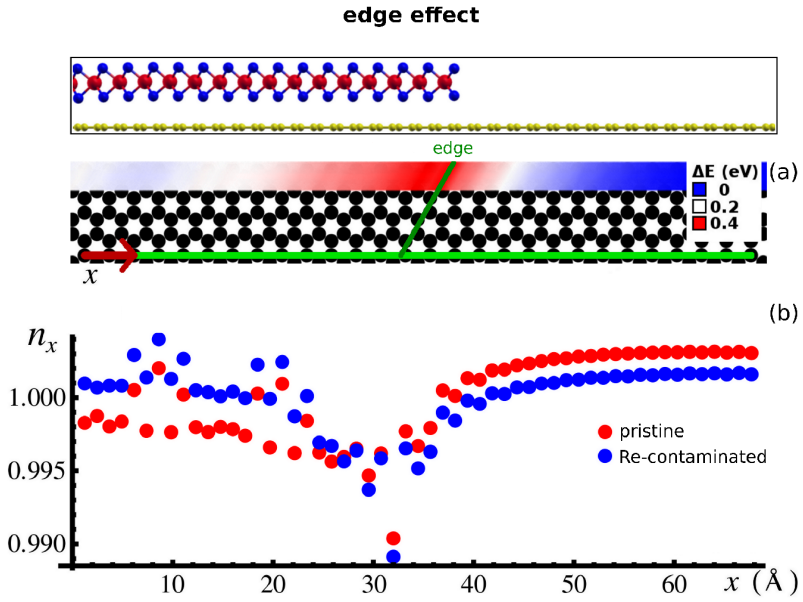

Figure 4.19: Edge effect in a graphene/MoS_2 hybrid. - (Top panel) Sketch of the setup from a side view. (a) Visualization of p_z on-site energies of graphene atoms (black dots) from top view. The on-site energies are defined with respect to the lowest values, which can be found in uncovered graphene far away from the edge. Details of the on-site energy calculations can be found in App. A.2.4. (b) Occupation n_x along the light green line depicted in a) for pristine (red) and defective (blue) MoS_2. $n_x > 1$ corresponds to n-type doping, $n_x < 1$ to p-type doping. The maximum value, about $n_x = 1.004$, corresponds to an electron-doping of $1.5 \cdot 10^{13}$ cm^{-2}.

4.2.2 MoS_2 edge states acting on Dirac fermions

Besides "vertical" graphene doping through defects, we furthermore investigate effects related with a partial coverage of graphene by MoS_2, see Fig. 4.18 (top panel). Lateral effects, such as potential gradients and planar charge redistributions near edges, can potentially improve the applicability of hybrid compounds. In Sec. 4.2.3, we will present an application of the graphene/MoS_2 heterostructure as a photovoltaic device, which is based on edge effects. Graphene sheets partly covered with MoS_2 flakes will obviously lead to a built-in potential landscape in the sample. To simulate edge effects and the resulting potential landscape within DFT, we constructed a large graphene supercell with half MoS_2-coverage. In order to avoid confinement effects, the supercell encompassed a large stripe with the length of nearly 100 Å, in total 600 atoms, and different edge configurations (see App. A.2.4 for computational details). In total, three realistic edge con-

figurations of MoS_2 [196, 197] were simulated, namely the S-terminated $(\bar{1}010)$ edge and the Mo-terminated $(10\bar{1}0)$ edge saturated with either S dimers or S monomers. A sketch of graphene under a $(1\bar{0}10)$ edge is given in the top panel of Fig. 4.19.

A crucial question is to what extent lateral transport in graphene is hampered by the potential under a MoS_2 edge; particularly, since there is only a weak van der Waals bonding between graphene and MoS_2. To analyze this, we plot in Fig. 4.19a graphene p_z on-site energies in the hybrid below a $(1\bar{0}10)$ edge. A potential step building up in the edge region (dark green line) on the order of 400 meV can be discerned. The potential gradient is induced by a work function difference between the uncovered and the covered part, similar as for pristine graphene contacted with a metallic electrode [198]. The presence of a built-in electric field leads to a charge reordering effect, which is shown in Fig. 4.19b (red dots). Here, the p_z occupation number is plotted along the green line in panel a. The uncovered part of graphene is slightly n-doped in the contact region due to lower on-site energies. In contrast, the MoS_2-covered graphene is locally p-doped. We emphasize again the locality of the reordering effect: At far distance, both sides are undoped under the assumption of no further disorder. Close to the edge (at 32 Å in Fig. 4.19b), a depletion zone is formed. This is in close analogy to the graphene/metal scenario, where an electric field leads to a charge reordering effect, which builds up a p-n junction.

It should be noted that the results are qualitatively the same for other edge configurations (see App. A.2.4). Although the shape of the potential barrier varies, it is always on the order of some hundred meV, and the resulting electric field is directed such that charge separation leads to a similar junction as depicted in Fig. 4.19. Another remarkable feature in the occupation number plot are kinks in the MoS_2-covered part. These are not of technical origin, but a consequence of the moiré superlattice: for most graphene atoms, $n_x < 1$, but some atoms in the unit cell (Fig. 4.18b) are located below the middle of a MoS_2 hexagon, which suppresses discharging and even leads to $n_x > 1$.

The picture becomes more manifold if Re impurities are taken into account. In this case, bulk doping by Re and charge redistributions at the edge are two superimposing effects. This can be seen in Fig. 4.19b (blue dots): Here, both sides below the edge become n-doped, giving in the end an n-p-n junction with a very narrow p-doped region. In this setup, a high impurity concentration as in

Fig. 4.18b was simulated and the minimum distance of the Re impurities from the edge was 10 Å. The interplay of different edge types, impurity types and concentrations yields a multifaceted picture of electrostatic effects below MoS_2 edges. However, we find considerable potential steps and charge redistributions for all configurations. One application of this inhomogeneous potential landscape is discussed in the next section.

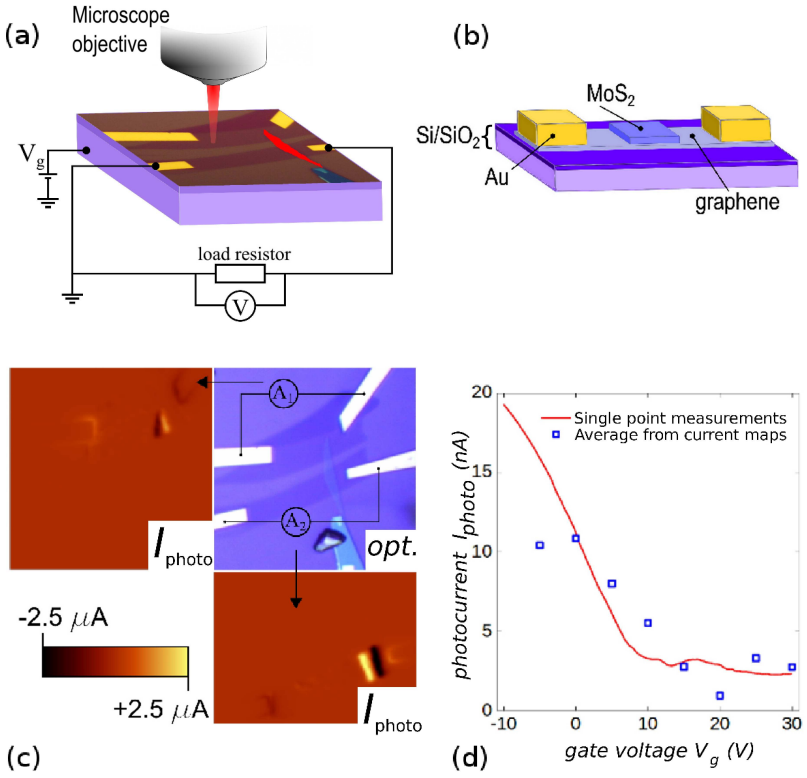

Figure 4.20: Photodetector based on a graphene/MoS_2 heterostructure. - (a) Illustration of the sample. Graphene (brown stripes) is contacted with gold (yellow bars) and covered with a MoS_2 flake (red stripe) in perpendicular orientation. The sample is irradiated by a laser beam of 633 nm wavelength. (b) Lateral cut through the sample. (c) Photocurrent measurements of the geometry shown in the optical image (top right panel). The top left (bottom right) image shows the photocurrent maps for the system with terminals connected to the top (bottom) electrode. (d) Response of the photocurrent to the gate voltage for static point measurements and averages of photocurrent maps.

4.2.3 A photovoltaic application of the graphene/MoS_2 hybrid

Graphene/MoS_2 hybrids have been examined by experimental colleagues at the University of Manchester. To this end, photocurrent measurements of graphene covered with MoS_2 flakes were performed (see Fig. 4.20). After placing the graphene/MoS_2 sample on a piezoelectric stage, it was illuminated with a 1.96 eV (633 nm) laser[1]. This setup allowed measuring of (spatially resolved) photocurrent maps by varying the stage position. Fig. 4.20c (top left and bottom right panel) shows such measurements of a setup as depicted in the optical image (top right panel). While in most regions, including the gold contacts, only a weak signal is detected, the measurements exhibit a strong signal in the heterostructure region, where graphene is covered by a MoS_2 flake.

Obviously, laser-induced electron-hole pairs can be more efficiently separated in the heterostructure region than near the gold contacts. A comparison with the optical image clearly allows for identification of the gold contacts (white stripes) and the MoS_2 flake (light blue stripe). When the laser illuminates uncovered graphene, the photocurrent is virtually zero. Here, small finite currents can be attributed to fluctuations of local doping. In contrast to usual graphene-based photodetectors (see, e.g., Refs. [199, 200, 201, 202]), a large photocurrent is not generated near metal contacts, but in the heterostructure region. The charge separation can be traced back to the interplay of the simulated impurity doping and the edge-induced electric field. The symmetry of the strong signal in the photocurrent maps demonstrates that the current is generated at the interface region of bare and MoS_2-covered graphene. Graphene covered with Re-contaminated MoS_2 is doped with electrons, while bare graphene is undoped. Due to work function differences, an electric field builds up as discussed in Fig. 4.19, which efficiently separates electrons and holes induced by the laser. Thereby, the device is not sensitive to the origin of electron-hole pairs. These are generated in graphene, but might also be photoexcited in MoS_2 and drift to graphene, or result from a thermoelectric effect (hot carriers have been reported in both 2D materials [203, 204, 205]). Since the photocurrent in the active regions is proportional to the local potential gradients, the photocurrent maps can be used to monitor the built-in potential landscape with spatial resolution. Moreover, local variations of the doping, respectively the Fermi level position, can be resolved

[1]The laser had a power of 80 μW and a 0.5 μm spot radius. More details on the experiment and sample preparation can be found in the original publication [145].

spatially, making this device a powerful tool for analysis and characterization of novel heterostructures.

Interestingly, the potential barrier can be tuned by applying an electric field. In the experimental setup, this is realized by an external gate voltage. The response of the photocurrent with respect to the gate voltage is depicted in Fig. 4.20d. The measurements were performed in two ways (static point measurements and photocurrent map averages, see also Ref. [145]) and give qualitatively the same trend: For positive gate voltages, the photocurrent drops down and saturates towards a small value at $\sim$ 30 V, corresponding to an electron concentration of $2 \cdot 10^{12}\mathrm{cm}^{-2}$. At this high voltage, the heterostructure region can hardly be distinguished in the photocurrent map, indicating an equalizing of the doping levels in bare graphene and MoS_2-covered graphene. On the other hand, for negative gate voltages (hole doping), the photocurrent increases. The measurements confirm our theoretical results: Obviously, MoS_2-covered graphene is electron-doped in agreement with our proposed scenario of Re impurities. N-type doping of graphene was recently confirmed in Ref. [146].

The origin of the potential barrier sensitivity to electric fields can be found again in the peculiar electronic structure of graphene and the impurity states in the conduction band. Fig. 4.21 gives a sketch of the local Fermi evolution in uncovered and MoS_2-covered graphene for different gate voltages. Without a gate voltage applied ($V_\mathrm{g} = 0$), bare graphene is undoped, while the Fermi level in the MoS_2-covered part is pinned due to impurity states, yielding an n-type doping. Switching on a gate voltage then leads to different response in both sides. While in uncovered graphene, all charge density ρ is collected in graphene bands, the situation is different in the covered region: In the graphene/MoS_2 heterostructure, MoS_2 and impurity states can be present at the Fermi level. Due to graphene's low density of states, large parts of ρ are taken up by MoS_2 and the impurity band, which becomes slowly filled. Since the Fermi level in the uncovered part increases much faster, both Fermi levels become equal around $V_\mathrm{g} = 30$ V, and the potential barrier vanishes together with the photocurrent. At negative voltages, the partially filled impurity band empties slowly and the potential barrier increases. The Fermi level pinning plays the crucial role here for the existence of an electric field. In other words, the MoS_2 on top of graphene effectively screens out the electric field between graphene and the back gate, which is related to the high quantum capacitance of graphene [206].

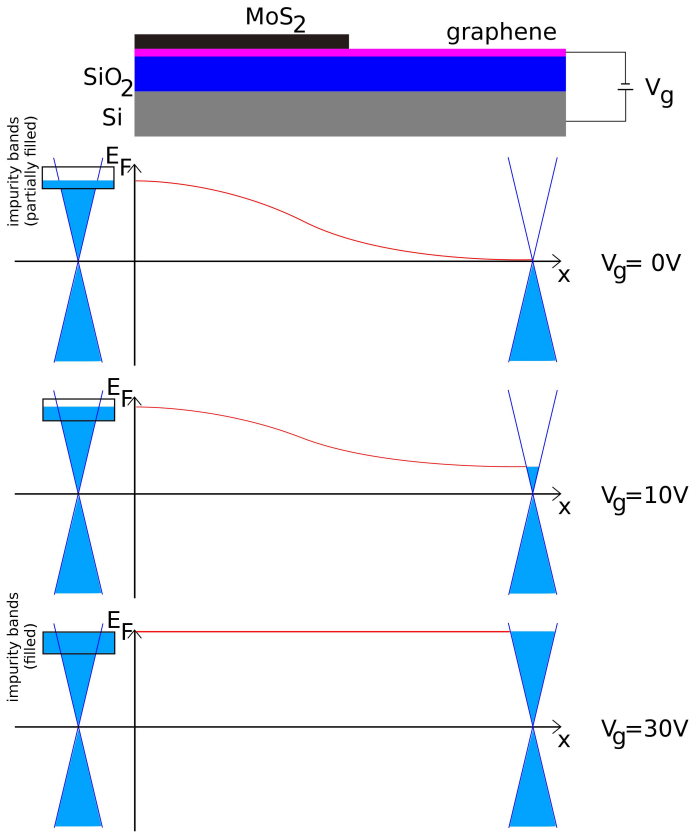

Figure 4.21: Gate-dependent Fermi level evolution. - Illustration of the local Fermi level in graphene for different gate voltages in the device as a function of the lateral position. While the impurity band is only slowly filled with the positive gate voltage in MoS_2-covered graphene (left), the Fermi level in the uncovered region (right) increases fast due to graphene's low density of states.

Altogether, the studies of this chapter prove the importance of first-principles simulations on the atomic scale for a fundamental understanding of novel van der Waals heterostructures. In particular, the interplay of moiré potentials, edge effects, and local defects calls for electronic theories valid up to the mesoscale. This, and the combination of these methods with many-body methods will be required to gain a complete understanding of the electronic properties of 2D-based heterostructures and, in particular, the behavior of Dirac fermions in van der Waals hybrids.

5

Graphene on metals as seen by scanning tunneling microscopy

This chapter is devoted to the properties of graphene-metal substrate interfaces with a special focus on local probe experiments (STM). Realistic graphene devices obey mostly interactions with an underlying substrate. The physics of graphene-substrate interfaces are manifold and depend significantly on the substrate material. We have been approaching an understanding of metal substrate interaction with graphene in recent years in collaborations with the experimentalist groups of R. Wiesendanger (U Hamburg, Ref. [207]) and R. Berndt (U Kiel, Ref. [208]). In particular, we aim for an analysis of metal substrate effects in local probe experiments and the electronic properties of metal substrates upon graphene adsorption.

In our joint experimental and theoretical investigations of graphene on the magnetic Ni(111) surface and graphene on non-magnetic Ir(111), we find large influence of graphene on the substrate properties; not only in the strongly bound case of graphene/Ni(111), but also in the system of graphene/Ir(111), where the interaction is dominated by van der Waals forces. The effects comprise surface state quenching, spin-polarization inversion in the vacuum and surface resonance shifts. We furthermore show that the underlying band structure effects are crucial for the visibility of graphene states in STM/STS, which must be considered in interpretations of local probe experiments.

5.1 Graphene, metals and STM: general remarks

Metal surfaces are an appropriate choice to grow clean graphene flakes of large size, such are, for instance, Ni [209], Cu [210], Pt [211], Ru [212], Rh [213] and Ir [214]. Mostly, metal growth techniques rely on surface segregation of carbon atoms or on chemical vapor deposition (CVD) by means of hydrocarbon decomposition on the metallic surface (cf., e.g., reviews in Refs. [215, 216] and many others). The adsorption of graphene on metallic substrates strongly varies with the substrate material, from strong chemical bonds and lattice matching, to physisorption and the formation of moiré superlattices due to lattice mismatch [215, 216, 217, 218]. STM studies prove a high structural quality of graphene on the metal surface and high continuity, even over steps between flat terraces [216]. To exploit graphene's unique electronic properties, however, graphene is frequently transferred or separated from the substrate. This is because metallic states around the Fermi level dominate in transport, and often the metal-graphene interaction diminishes the Dirac-like behavior of low-energy carriers.

Moiré superlattices of graphene on metals indicate a weak bonding of graphene and usually preserve the Dirac bands. However, mostly a charge transfer due to work function differences between the metal and the graphene layer is observed [217]. This effect can be utilized to build p-n junctions in graphene by employing metal contacts, which is relevant for, e.g., photocurrent generation. In analogy, the graphene/MoS_2 hybrid presented in Sec. 4.2 exploits an inhomogeneous doping induced by (lateral) work function differences, making the system suitable for efficient electron-hole separation.

Scanning tunneling microscopy (STM) is a powerful tool to investigate local structural and electronic properties of graphene on metals, for both weakly and strongly bound systems. Remarkably, its atomic resolution allows for identification of single graphene atoms up to large moiré patterns (Fig. 5.1b). In short, STM relies on the tunneling of a current between a thin metallic tip and the investigated surface. The tip is as sharp as possible (at best, one atom sharp at the apex), and placed in the vacuum at a typical distance of about 3-10 Å above the surface. From Bardeen's formalism, a formula for the tunneling current I can be derived, which depends on the local density of states (LDOS), the temperature (via the Fermi-Dirac distribution $f(\epsilon)$), and a tunneling voltage V, which is

applied between the tip and the sample [219]:

$$I \sim \int_{-\infty}^{+\infty} [f(E_\mathrm{F} - eV + \epsilon) - f(E_\mathrm{F} + \epsilon)]\, \rho_S(E_\mathrm{F} - eV + \epsilon)\rho_T(E_\mathrm{F} + \epsilon)|M|^2 d\epsilon, \quad (5.1)$$

whereby M is the z-dependent tunneling matrix from Fermi's golden rule, and ρ_S and ρ_T denote the density of states of the sample and the tip, respectively. Note that the temperature dependence of the integrand requires low temperatures for a high resolution in energy. One can show that the current decays exponentially with the height z (see Sec. 5.2). Topography maps can be recorded by keeping the bias voltage constant and moving the tip laterally. Vice versa, at a fixed position of the tip, one can sweep bias voltage to record differential conductance spectra (dI/dV maps). Such scanning tunneling spectra (STS) are, according to Tersoff-Hamann theory, directly proportional to the vacuum LDOS [220, 221]

$$dI/dV \sim \rho_s(E_\mathrm{F} - eV). \quad (5.2)$$

Structural and electronic properties with atomic resolution as probed in experiments may then be directly compared to *ab initio* density functional theory simulations, which we perform to obtain theoretical STM images and STS spectra.

5.2 Graphene on Ir(111)

Scanning tunneling spectroscopy (STS) experiments of graphene islands on the Ir(111) surface were performed by the group of R. Berndt, S. Altenburg, and co-workers at the University of Kiel. Fig. 5.1a (inset) shows two dI/dV curves - one on the bare Ir(111) surface and one of graphene on Ir(111). Over the bare Ir surface (blue curve), a step-like drop of the signal can be discerned around a sample voltage $V \approx -350$ meV, and a similar drop of the signal is found over graphene (red curve), but shifted upwards to $V \approx -150$ meV. This is confirmed by the spatially resolved STS spectra in the main plot (see figure caption for details).

In order to understand the spectra in detail, *ab initio* calculations were performed. An Ir(111) surface of a thickness of 18 layers was modelled in order to simulate surface states and to avoid spurious interaction between the periodic surface unit cells. Spin-orbit interaction was included to account for the Rashba-type splitting of Ir surface states [222]. For calculation details, see App. A.3.1.

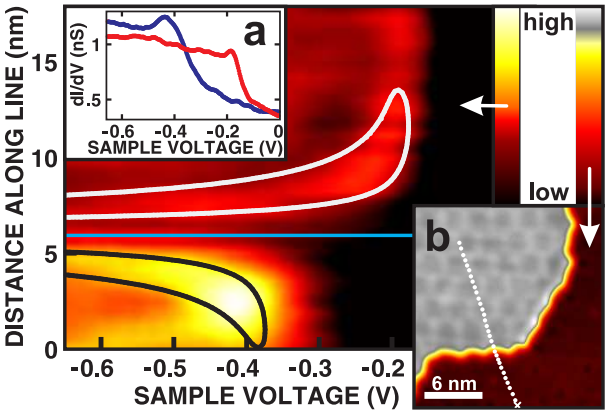

Figure 5.1: Experiments: STS of graphene islands on Ir(111). - Main figure: STS (dI/dV) measured (by the Berndt group) as a function of the sample voltage along a path from bare Ir to a graphene island as depicted by the white dots in inset (b). The crossover is indicated by a horizontal blue line and spectra of the beginning (blue) and the end point (red) of the path is shown in inset (a). The data clearly shows a shift of the surface resonance onset. For more details, see the original publication [208].

The band structure of the Ir slab is shown in Fig. 5.2a (gray lines). Many bands are present due to the large number of electrons in the unit cell. The states around E_{F} are of a mixed p and d orbital character, and can be partly identified as bulk bands. For instance, around the $\bar{K}$ point, the large Ir bulk gap is reproduced. In addition, surface states emerge around this point, and a pronounced hole-like surface resonance at the $\bar{\Gamma}$ point. In the energy interval -1 eV $< E <$ 0 eV, the resonance, which is mainly derived from Ir p_z orbitals, is approximately parabolic. In Fig. 5.2a, the resonance is marked by a thin green line. We find an effective mass of $m^* \approx -0.17 m_e$, which is in excellent agreement with the experimentally derived value of $-0.18 m_e$.

For a better comparability of the band structure simulations to the experiments, tunneling current contributions were calculated, which is again visualized in Fig. 5.2a by blue "fat bands". The tunneling current contributions were calculated based on Tersoff-Hamann theory. The tip was modeled as an empty s orbital $|L\rangle$ placed in the vacuum in a typical height (0.48 nm) above the surface. The width of the blue bands in Fig. 5.2a depicts the overlap $|\langle \Psi_{n,k}|L\rangle|^2$ of the Bloch wave function $|\Psi_{n,k}\rangle$ at wave vector k and band n. The resulting blue "fat bands" prove that the tunneling current is mediated by the surface resonance in the entire energy (voltage) interval investigated in STM (Fig. 5.1).

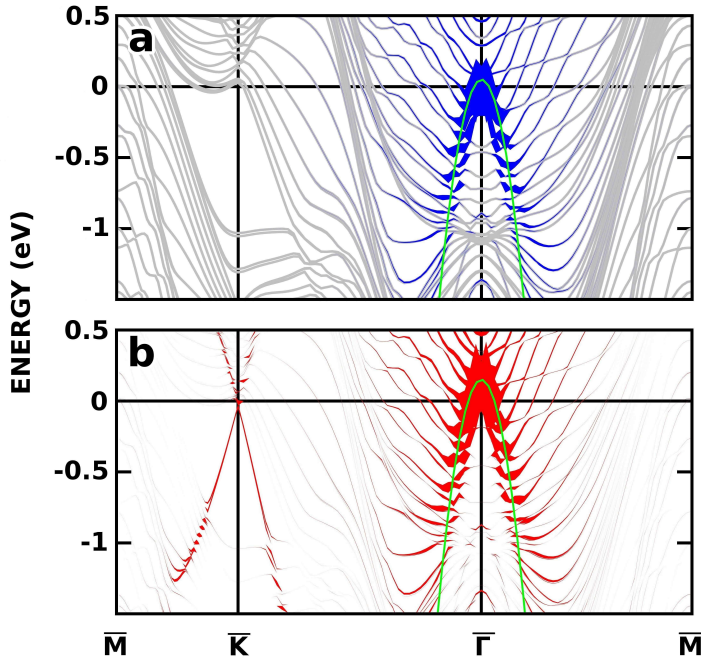

Figure 5.2: Energy bands of Ir(111) and of graphene islands on Ir(111). - (a) Simulated band structure of the bare Ir(111) surface (gray lines). Coloured "fat bands" visualize states contributing to the tunneling current above the Ir(111) surface (a) and above the graphene/Ir(111) system (b). Green parabolas, fitted by an effective mass $m^* \approx -0.17 m_e$, show a shift of the resonance when the Ir surface is covered with graphene. For both systems, the Ir surface resonance predominates in the STM signal, while graphene states play a minor role.

When graphene is placed on top of the Ir(111) surface, it binds only weakly to the substrate and gives rise to a moiré pattern (see, e.g., Refs. [169, 214, 218, 223, 224, 225, 226]), that covers an area of 10x10 primitive graphene cells (or 9x9 primitive Ir(111) unit cells). Similar as for graphene on insulating h-BN (Sec. 4.1.1.1), the interlayer distance within the moiré is not constant. As has been shown by non-local van der Waals density functionals [225], the height variation in graphene/Ir(111) is between 3.27 and 3.62 Å. The interlayer binding heights are thus very similar to those of graphene on h-BN or TMDCs, although the underlying binding mechanism is different for graphene on metallic Ir(111): graphene adhesion on h-BN is mostly van der Waals-dominated, whereby, amongst others, slight electrostatic contributions due to partially charged B and N atoms play a role [227]. The graphene/Ir(111) interface is in fact equally constituted by van der Waals forces. However, there is additional chemical modulation within the

moiré: despite of an average antibonding chemical interaction, in some regions weak covalent bonds are formed due to accumulated charge in the interface [225], leading to adsorption heights deviating from the mean value of 3.41 Å.

In the simulations, we had to enforce a lattice matching of graphene and Ir(111) due to the large number of Ir layers in the unit cell, but we tested carefully different stacking configurations and adsorption heights. Thereby, we verified in particular not only the modification of graphene electrons upon adsorption of graphene on the Ir(111) surface, but the modification of the substrate properties as well. Surprisingly, experimental as well as theoretical literature about graphene impact on substrates is rare, although metal surface electrons are generally well-known to be sensitive to adsorbents.

Looking at Fig. 5.2b, one can find a huge graphene effect on Ir states: The surface resonance is shifted upwards between 100 and 200 meV, dependent on the graphene-Ir distance between 3.27 and 3.62 Å in the respective stacking configuration. Moreover, we can see from the simulated tunneling current contributions that the main contributions are still due to the Ir surface resonance, while graphene p_z states only marginally contribute to the signal. This is counter-intuitive because the graphene layer is located much closer to the STM tip. An explanation for this observation is found in the location of the graphene Dirac point in k space: low-energy electrons in graphene around the K point have parallel momenta $k_\parallel$, while the surface resonance is located at the Γ point. Starting at sufficient height $z \gtrsim 1.5$ Å above the surface, probability densities of wave functions decay as $|\Psi(z)|^2 \sim e^{-\lambda^{-1}z}$ in the vacuum. The decay constant λ can be obtained from the one-particle Schrödinger equation [221, 228] as

$$\lambda^{-1} = 2\sqrt{k_\parallel^2 + 2m\phi/\hbar^2}, \tag{5.3}$$

where the work function ϕ is the potential barrier that has to be overcome by electrons in order to leave the surface and to contribute to the tunneling current. As a rough estimate, inserting the graphene p_z momentum $k_\parallel$ =1.7 Å and the work function of graphene on Ir(111), ϕ =4.4 eV, in the formula, one finds $\lambda^{-1} = 4.0$ Å^{-1}, while at the Γ point $\lambda^{-1} = 2.2$ Å^{-1}. Hence, graphene states at the K point decay much faster in the vacuum than states related to the surface resonance, where $k_\parallel = 0$. In principle, scattering of states from the K point to the Γ point might occur due to the periodic moiré potential. However, this is unlikely due to the large moiré wavelength, which corresponds to small momenta, thus, multiple

scattering processes would be required.

The theoretical results shed light on the measured scanning tunneling spectra. First of all, the experimental shift of the STS signal of about 190 meV is in good agreement with the calculations. Second, STM signals originate almost entirely from the Ir surface resonance, that becomes shifted upwards in energy upon graphene adsorption. Importantly, the graphene states are nearly invisible in the signal, which is confirmed by the absence of electron-hole symmetry in the experimental spectra. This important issue had been overlooked so far in STM studies of graphene on Ir(111), where spectral properties were interpreted on the assumption of electron tunneling from graphene to the STM tip [229, 230]. In the experiment, our colleagues further demonstrated confinement of STM-measured states due to the nanometer-sized graphene islands. These results are in contrast to Ref. [231], where graphene states were erroneously assumed to be decisive for confinement at certain island sizes. Our results on the resonance shift were confirmed at the same time independently in Ref. [232], where the Ir(111) surface resonance, including the large Rashba splitting, was shown to persist under ambient atmosphere.

Finally, we seek for a better understanding of the origin of the upwards shift of the surface resonance under graphene. Coulomb interactions arising from charge redistribution [225] as well as Pauli repulsion may potentially affect the Ir surface resonance. To learn more about this, we performed again calculations of an Ir(111) surface, but this time covered with a layer of neon (Ne) atoms instead of graphene. With the layer of chemically fully inert Ne atoms, adsorbate states are unavailable around the Fermi level such that no charge from the Ir substrate can be accepted or donated. For the same adsorption heights as for graphene, we observe virtually the same upwards shift of the surface resonance. This indicates that the resonance shift in graphene/Ir(111) is owing to Pauli repulsion. However, Coulomb potential effects certainly play a role as well and may not be neglected. This becomes obvious from a look at the graphene Dirac point, which is downshifted in energy, when graphene is artificially pushed towards the substrate. Thus, charge rearrangements and resulting Coulomb interactions are decisive for the position of the Dirac cone on the Ir(111) surface. Altogether, the results prove the importance of careful interpretation of STM/STS spectra of graphene on metals, which will be confirmed by the next section about graphene/Ni(111).

5.3 Graphene on Ni(111)

Long time before the isolation of graphene in 2004 [2], the Ni(111) surface was used for the growth of carbon monolayers (see, e.g., [233, 234]). Since the rise of graphene, metal growth techniques such as chemical vapour deposition (CVD) [235] were continuously improved, leading to the ability of large-scale growth of graphene on Ni(111) [236, 237]. In a joint theoretical and experimental study with experimentalists from the groups of R. Wiesendanger and H. P. Oepen (U Hamburg), we investigated the bare Ni(111) and the graphene-covered Ni(111) surface on length scales from the sub-nanometer up to the millimeter scale. Details about physics on the millimeter scale, such as magnetic domain patterns, can be found in the paper [207]. Here, we continue the aim of this chapter to investigate graphene/metal interaction on an atomic scale and gain insight into STM experiments (performed by the Wiesendanger group) from theory.

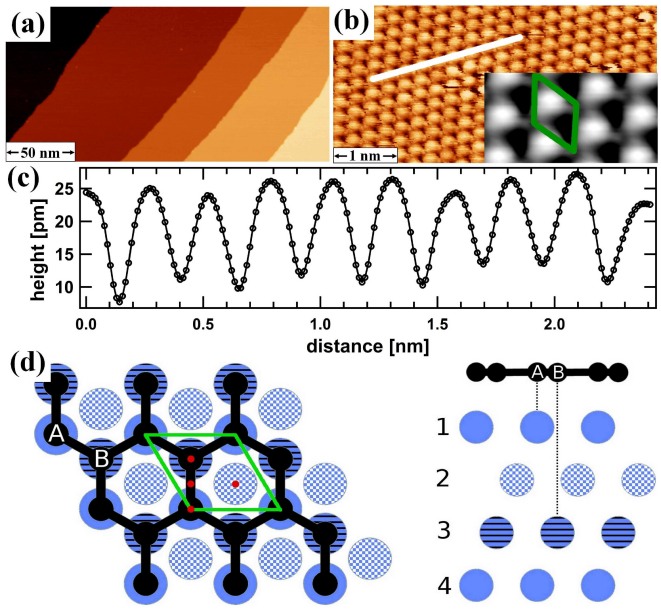

Figure 5.3: STM experiments of graphene on Ni(111). - (a), (b) Constant current image (topography) image (Wiesendagner group, for details, see [207]). The green diamond shows the unit cell used for simulations (d). (c) Height profile along the white line in (b). (d) Top and side view on the simulated geometry. Red dots visualize positions of the empty spheres in the calculations.

Experimental STM images and a sketch of the adsorption geometry of graphene on Ni(111) are shown in Fig. 5.3. In contrast to graphene on Ir(111), it is known

that graphene is chemically adsorbed on the Ni surface [233]. The lattice constant of Ni is very close to those of 2D h-BN. However, due to the strong bonding of graphene on Ni(111), a commensurate lattice instead of a moiré pattern is formed [238]. Fig. 5.3a,b, and c show STM measurements performed on the system. It turns out that the corrugation on top of the surface (about 10-15 pm in a unit cell) is enhanced compared to the bare Ni surface by a factor of 3.

To verify the origin of the corrugation and for further interpretation of STM images, DFT simulations were performed of the geometry depicted in Fig. 5.3d, which is the so-called *top-fcc* arrangement (for technical details, see App. A.3.2). Here, one carbon atom (named atom A) is sitting above a Ni atom of the first Ni layer, and the second graphene atom (atom B) is on top of an atom of the third Ni layer. This was shown to be the most favorable configuration in experiment [239] and theory [240]. It was argued that another configuration, the *bridge-top* configuration, is energetically close to the *top-fcc* configuration [240, 241], but the coexistence is supposed to depend on the presence of impurities [242].

Our calculations yield an adsorption height of graphene of ~ 2.10 Å, which is in good agreement with the literature [217, 239, 240, 241, 242]. The corrugation we found in the unit cell, thus the height difference between carbon atom A and B, was only 0.5 pm and therefore much smaller than those obtained by STM (10-15 pm). The reason for this discrepancy can be understood from the fact that the STM topography mode records modulation of electronic states, which is not necessarily coincident with the atomic corrugation. Indeed, the enhanced corrugation over the graphene/Ni(111) surface is an electronic effect. Indications for this can be found in the simulated STM images for a tip height of 3.6 Å.

For the bare Ni(111) surface (Fig. 5.4a), one observes a triangular pattern of protrusions (bright spots) in good agreement with the experiment (for experimental results on the bare Ni(111) surface, cf. [207]). Hence, states probed in STM are related with atoms of the topmost Ni layer, where the atoms are arranged in a triangular lattice and supply a high LDOS in the vacuum. For graphene on Ni(111), the situation is different (Fig. 5.4b): Only one of two carbon atoms per unit cell (green box) causes a bright spot in the STM image, which forms again a triangular pattern in agreement with the experiment (Fig. 5.3b). Following the notation of Fig. 5.3d, we find that only carbon atoms in sublattice B induce the bright spots. The effect is stable under variation of the bias voltage or the tip height and originates from a sublattice symmetry breaking. The Ni atoms of the

topmost layer hybridize with graphene A's p_z states in contrast to B sublattice atoms, meaning that carbon atoms in the A and B sublattice are not any more electronically equivalent. The high corrugation as observed by STM is thus an electronic effect. The origin of the electronic interface effects will be discussed in the following.

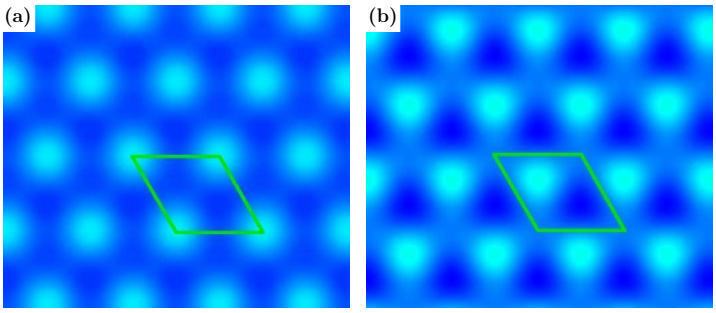

Figure 5.4: Simulated STM of graphene on Ni(111). - The spectra were simulated in a height of 3.6 Å above the bare Ni(111) surface (a) and above graphene on Ni(111). Unit cells are highlighted by green boxes.

More insight into this mechanism can be gained from simulated STS (dI/dV) spectra. To calculate dI/dV spectra, we simulate the LDOS in the vacuum and employ the Tersoff-Hamann approximation [220, 221], where influence of the STM tip on the sample is neglected and the differential conductance is assumed to be proportional to the LDOS according to Eq. 5.2. The vacuum LDOS is calculated inside empty atomic spheres in the vacuum (see below).

In this way, local vacuum states can be directly compared to spectra obtained from scanning tunneling spectroscopy (STS) for different lateral positions of the STM tip. Simulated vacuum spectra of the bare Ni(111) surface are shown in Fig. 5.5a. There is good qualitative agreement between the spin-averaged spectrum and the experimental STS spectra (experimental spectra can be found in the original publication [207]). The spectra exhibit two signficant maxima, one around -1 eV below the Fermi level and one broad maximum around +1eV above the Fermi level. The peaks remain invariant under variation of the lateral position in the unit cell. Important to note is the difference of spectral distribution in majority and minority spin channels. The peak at -1 eV can be derived from minority spin states, while the majority states carry more weight at positive energies. Therefore, spin splitting of states can be detected in the vacuum using spin-polarized scanning tunneling microscopy (SP-STM) above the bare Ni(111)

surface.

The energy-dependent spin contrast, which can be defined by the spin-polarized DOS $\rho_{\uparrow,\downarrow}$ as $\Delta\rho = (\rho_\uparrow - \rho_\downarrow) / (\rho_\uparrow + \rho_\downarrow)$, is depicted in Fig. 5.5b (blue dashed line). It is negative below the Fermi level and changes sign at $E = 0$. Surprisingly, when Ni is coated with nonmagnetic graphene, the spin contrast curve exhibits a different progression (red line). The spin contrast (averaged over four lateral tip positions as shown in Fig. 5.3d) shows sign reversal for energies at -0.23 eV and above E_F. This allows for the following important conclusions: 1. The graphene overlayer does not suppress spin polarization of states in the vacuum. This is confirmed by ferromagnetic domains observed in SP-STM 2. The graphene layer induces a spin contrast reversal in the vacuum.

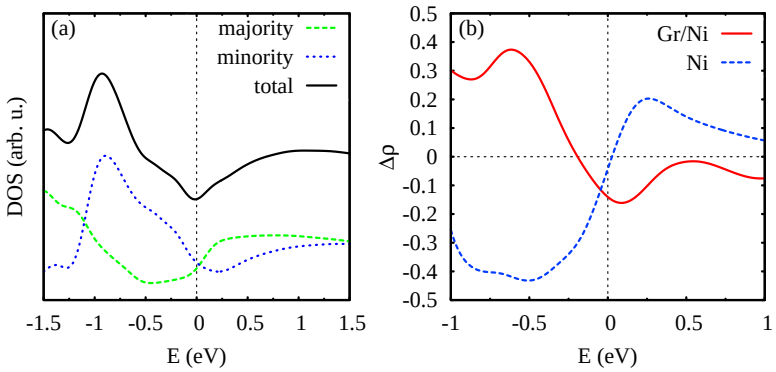

Figure 5.5: Simulated STS of Ni(111) and spin contrast of graphene/Ni(111). - (a) Vacuum spectra of the bare Ni(111) surface for the majority and the minority channel. The spectra were simulated in a height of 3.6 Å and weighted by a height-dependent factor as given by Eq. A.4. (b) Spin contrast $\Delta\rho$ in the vacuum above the graphene/Ni(111) surface. The Fermi level has been set to zero in both figures.

To learn more about the origin of the spin contrast reversal and the STS spectra, we verify the orbital character of states contributing to the tunneling current. Therefore, band structure calculations were performed together with a "fat bands" analysis. Similar as in Sec. 5.2, we make use of empty spheres placed in the vacuum in different lateral positions. The wave function $|\Psi_{n,k}\rangle$ can be projected onto an empty s orbital $|L\rangle$ in a typical height of 3.6 Å above the bare Ni surface or above graphene/Ni(111). The overlap $|\langle\Psi_{n,k}|L\rangle|^2$ is then depicted in Fig. 5.6 as an additional information by a colored thickening of the bands.

The band diagram of the pure Ni(111) surface is shown in Fig. 5.6 for the majority (a) and the minority (b) spin channel. Since the Ni surface was simulated

by a 15-layer-thick slab of Ni atoms, a considerable number of bands is present in the diagrams. The energy bands of bulk Ni [243, 244, 245, 246] and the Ni surface [245, 247, 248] have been well-studied, but here we focus on vacuum states contributing to the tunneling current. Above E_F (set to zero in the figure), in both channels upward dispersing bands with a minimum at the Γ point at energies of 10 meV (majority) and 140 meV (minority) can be discerned, which dominantly contribute to the tunneling current at low positive voltages. The energy bands can be identified as surface states and surface resonances. The state in the majority channel was identified as a Shockley state and has a mixed orbital character [247, 248] formed by Ni p_z and $d_{3z^2-r^2}$ states at the Γ point and, for $k \neq 0$, admixtures of $d_{xz,yz}$ orbitals. The corresponding feature in the minority spin case is a mixture of p_z and $d_{xz,yz}$ states [247, 248].

Below the Fermi level, there is again one dominating feature in both channels. In the majority channel, it starts at -0.6 eV and disperses downwards away from the Γ point. The feature can be attributed to a surface resonance [245], while it exhibits a mixed Ni p_z and $d_{xz,yz}$ orbital character. A very similar surface resonance can be found in the minority channel [245, 248], but shifted upwards above E_F with identical orbital decomposition as the Shockley state. Compared to the majority channel, there is much higher contribution to the tunneling current due to this surface resonance in energy regions between ~ -1 eV and ~ 0.1 eV, which explains the spin-polarization of the STS spectra in this region. Therefore, the maximum at -1 eV in Fig. 5.5a can be attributed to the surface resonance, while at positive energies majority states dominate due to the Shockley state. The spectra demonstrate the importance of surface-related features to states the vacuum.

The image changes drastically upon adsorption of the graphene layer on the Ni surface. In particular, graphene has implications on states in the vacuum. The energy bands for the same Ni slab, now coated on one side with graphene, are shown in Fig. 5.6c and d. Conspicuously, graphene p_z states occur at the K point, but these do not resemble the well-known Dirac cones of free-standing graphene. Due to the effect of interfacial chemisorption, and due to sublattice symmetry breaking, a gap is opened between graphene π and π^* states. However, in both spin channels, the graphene states provide only small contribution to the tunneling current compared to the Ni-derived features around the Γ point. This is in analogy to graphene on Ir(111), where we found that graphene states are less

visible in STS than expected (see Sec. 5.2). A closer look at the energy bands reveals modifications of Ni states: One band, which is related to the Shockley surface state, (Fig. 5.6c) vanishes, such that only one band remains, which belongs to the pristine side of the Ni slab. Thus, the graphene overlayer quenches the Shockley surface state. Similarly, the downward dispersing surface resonance below the Fermi level is quenched as well. This explains the sign reversal of the spin contrast in Fig. 5.5b. We emphasize here that this reversal in the vacuum is not connected with an inversion of the magnetization in Ni surface atoms. The magnetic moments in the topmost Ni layer (0.51 μ_B) are merely reduced by about 20% compared to the bulk (0.65 μ_B). In agreement with the literature [238, 249], we furthermore find small induced magnetic moments in the graphene layer (-0.02 μ_B for C_A and 0.03 μ_B for C_B).

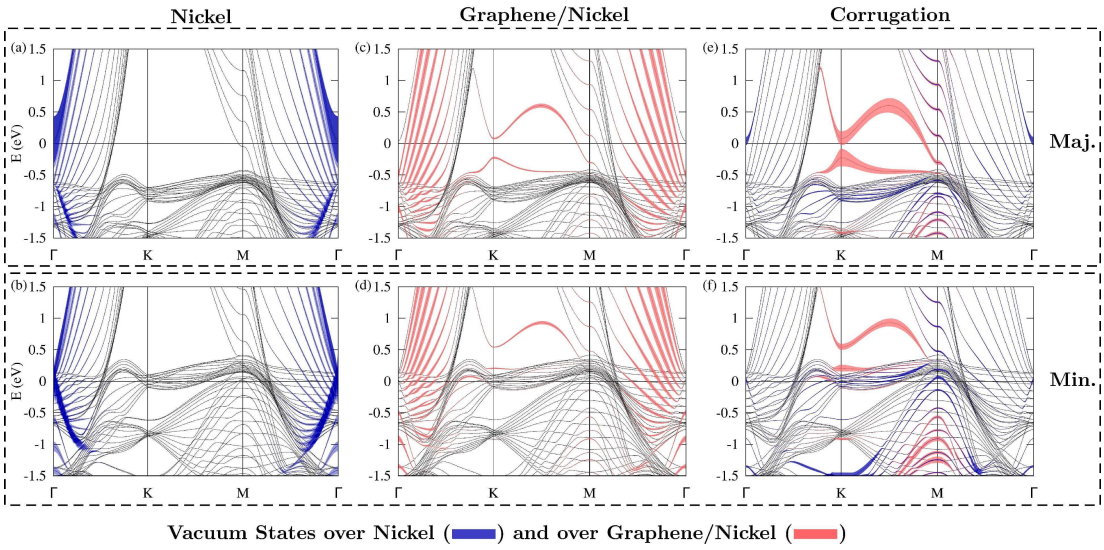

Figure 5.6: Band structure of Ni(111) and graphene/Ni(111). - Energy bands of a pristine Ni slab consisting of 15 layers in the majority (a) and minority (b) spin channels. Blue "fat bands" indicate vacuum states that contribute to the tunneling current for a simulated tip height of 3.6 Å and an *s*-like STM tip. (c), (d) The same for the graphene-covered surface (the slab is covered on one side with a graphene layer). Vacuum states are marked red. (d), (e) Visualization of states contributing to the corrugation measured in STM above the bare Ni surface and the graphene-covered side of the slab in the same color code. The corrugation above clean Ni is small and therefore enhanced by a factor of 4.

Finally, we make again use of the "fat band" technique to analyse the origin of corrugations as measured in STM. Since we place the empty spheres in different

lateral positions within the unit cell, we can compare the wave function amplitudes and identify from amplitude differences the electronic states responsible for the corrugation. The thickness of the bands in Fig. 5.6e and f is now used to depict the strength of corrugation. We define the thickness d of the colored bands as the standard deviation of vacuum projections as

$$d \sim \sqrt{\sum_r \left(|\langle \Psi_{n,k} | L_r \rangle|^2 - \overline{|\langle \Psi_{n,k} | L_r \rangle|^2} \right)^2} / \rho_{\uparrow\downarrow}(E), \tag{5.4}$$

for each band and k point with r indexing the four different lateral positions in the unit cell (red dots in Fig. 5.3d). The denominator normalizes the thickness of the bands with respect to the LDOS integrated over the Brillouin zone. The corrugation over graphene is much higher than over clean Ni(111), as can be seen in Figs. 5.6e and f. Responsible for the enhanced corruagtion in both spin channels are the graphene p_z states. Due to the sublattice symmetry breaking, graphene atoms C_A and C_B are not equivalent anymore, and STM measures only the LDOS of the C_B atom, while the C_A atom is strongly hybridized with the Ni atom located below. This in close analogy to STM of graphite, where an ABAB (Bernal) stacking evokes occurrence of a triangular lattice [250].

For STM measurements at very low bias voltages, close to the Fermi level, the corrugations are of a strong carbon p_z character in the majority spin channel, originating from the Fermi level crossing of the upper graphene band at the M point. In contrast, the minority spin channel exhibits additionally small Ni d contributions close to E_F and strong contributions from the lower graphene band. Over pristine Ni, corrugations are low and originate mainly from slight lateral wave function amplitude differences of Ni d states. This confirms again the purely electronic character of high corrugations measured in STM.

The graphene/Ni(111) system conveniently demonstrates the importance of careful interpretation of STM spectra. While the presence of graphene atoms is responsible for a strong increase of STM-measured corrugation, overall, graphene states are barely visible in the STM signal. This is in agreement with the weakly bound system graphene/Ir(111), although the underlying mechanisms are distinct from each other. Altogether, the studies of graphene/metal interfaces prove that the evolution of the wave function in the vacuum has to be carefully considered in simulations of STM/STS spectra; a comparison of experimental STS spectra with the simple graphene atom-centered LDOS is misleading for graphene/metal systems.

6

Nickel adatoms on graphene

6.1 Magnetic and electronic configurations

The electronic, magnetic and structural properties of individual Ni adatoms and Ni clusters on the graphene surface have only rarely been studied in theory (cf. [181, 251]). Experimentally, one paper of our and the Wiesendanger group (U Hamburg) [252] reported the adsorption site of single Ni adatoms by STM and revealed an orbital-selective coupling of the adatom on graphene from DFT. The effect was proven to be mediated by the unique properties of the graphene substrate. For Ni clusters on graphene, detailed knowledge about their properties is lacking, including electronic configurations and magnetic moment formation. Systems consisting of individual magnetic adatoms are not only important with regard to the downsizing of magnetic nanostructures. Also, there is a fundamental interest in magnetic moment formation in graphene, and an efficient way to generate spins in graphene would be a big leap forward in spintronics. Altogether, this calls for a deeper understanding of the interactions between magnetic impurities and the graphene substrate.

In collaboration with T. Eelbo *et al.* (Wiesendanger group, U Hamburg) x-ray magnetic circular dichroism, x-ray absorption and STM experiments as well as *ab initio* simulations were performed of $3d$ transition metal adatoms on graphene (cf. also Ref. [253]). In this section, we focus on individual Ni adatoms and clusters.

In agreement with previous works [181, 252], STM images show adsorption of the Ni adatom in the so-called "hollow" position, above the center of the graphene hexagon. In this adsorption position, the electronic configuration was

suggested to be $3d^{10}4s^0$, meaning the suppression of magnetic moment formation [252]. Indeed, we find the same hollow site adsorption and absence of magnetic moments from DFT calculations, see Fig. 6.1 for a plot of the Ni d LDOS. The LDOS in Fig. 6.1a is shown for both spin channels, and the curves exactly match each other. Thus, there is no spin-splitting observable, meaning the absence of a magnetic moment, which seems to confirm the scenario of an entirely filled d shell.

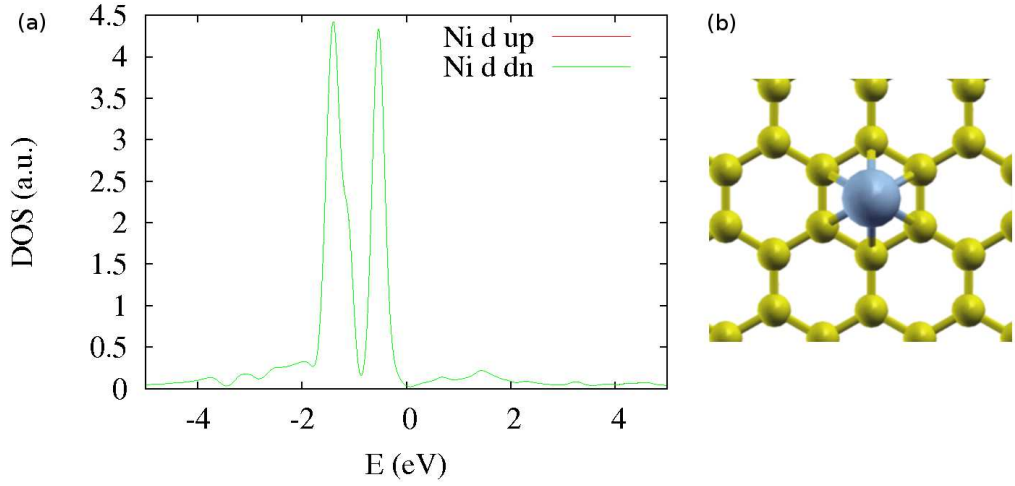

Figure 6.1: Absence of magnetic moment of Ni monomers on graphene - (a) Spin-polarized Ni d-LDOS. The Fermi level has been set to zero. The coincidence of the up- and down-LDOS shows the nonmagnetic nature of the Ni adatom. (b) Hollow-site adsorption of Ni monomer on graphene (yellow: C, blue: Ni) .

In the following, we verify whether this picture is oversimplified. To gain a more fundamental understanding of electronic and magnetic configurations of Ni adatoms, x-ray absorption experiments were performed by our experimental colleagues. X-ray absorption spectroscopy (XAS) is a powerful tool to investigate the local structure and unoccupied density of states of materials, and it is both element- and site-specific (for an introduction, see, e.g., Ref. [254]). Moreover, shining with circularly polarized light facilitates measurements of so-called x-ray magnetic circular dichroism (XMCD) spectra, which are simply the difference between XAS signals at positive and negative light polarization. In this fashion, magnetic moment formation can be detected. Fig. 6.2 shows experimental results on XAS and XMCD for graphene with low (a) and high (b) Ni coverages at the L_3 edge (for more details on experiments, c.f. Ref. [253]). At low coverage, most

Ni atoms occur as individual monomers and do not form clusters. The orange line in Fig. 6.2a shows the absence of an XMCD signal at normal (0 ° incident angle), and the same holds for grazing (70 °) incident angle (green line). This demonstrates the absence of a spin or orbital moment and suggests again a $3d^{10}4s^0$ configuration. However, a pronounced multipeak structure in the XAS spectra (black/red and blue/green curves, respectively) can be found, which exhibits two main peaks, named A and B. This behavior is in disagreement with the scenario of a fully occupied d shell. Since $2p \rightarrow 3d$ transitions would be excluded in a d^{10} configuration, $2p \rightarrow 4s$ excitations should be detected in XAS due to selection rules, but these transitions were shown to result in step-like XAS features due to broad $4s$ bands [255]. A multipeak structure, as observed here, is however indicator for a nonfully filled d shell and has been measured for gaseous Ni [256], which is known to be in a $3d^8$ configuration.

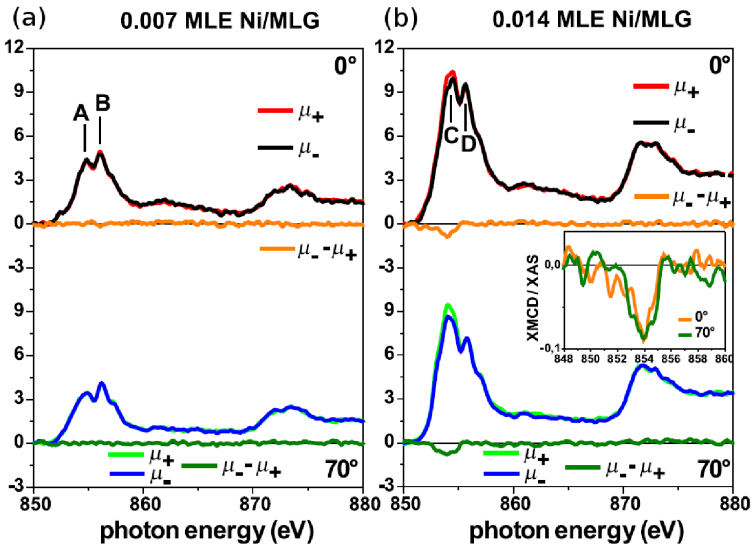

Figure 6.2: XAS and XMCD of Ni on graphene. - Measurements (by the Wiesendanger group) are shown for low coverage (a) and high coverage (b). (Upper panel) XAS measurements at 0 ° incident angle parallel (μ_+, red curve) and antiparallel (μ_-, black curve) alignment between the helicity of the incident beam and a magnetic field of $B = 5$ T. The XMCD difference spectra ($\mu_+ - \mu_-$, orange) are shown as well. (Lower panel) The same for a grazing angle of 70 °. The inset in (b) compares the XMCD signal for both incident angles by dividing the XMCD signal by the average XAS intensity.

In order to resolve this discrepancy, we simulated XAS spectra using the WIEN2K package (for computational details, see App. A.4.1). Using the dipole

approximation within Fermi's golden rule, XAS spectra are calculated as the product of the unoccupied LDOS and the transition matrix elements. We tested explicitly the effect of core holes and found only slight modifications of XAS spectra. Therefore, core hole effects were neglected in the calculations. Fig. 6.3a shows the XAS spectra of Ni monomers (black line). The relaxed adsorption height of the Ni monomer was found to be 1.55 Å. In agreement with the experiment, we identify two pronounced peaks at 0.7 eV (A') and at 1.6 eV (B') close to the L_3 edge. We associate these with the A and B peaks which can be discerned in the experimental spectra at 854.8 and 856.1 eV, respectively. The separation of the A and B peak in energy is 1.3 eV, while we obtain 0.9 eV in our calculations. This deviation might originate from neglecting of many-body effects, which renormalize the spectra. The orbitals responsible for the two-peak structure can be found from the Ni s and d LDOS, Fig. 6.3a. Apparently, the spectra mainly follow the d LDOS while the Ni s orbitals exhibit the largest weight at the A' peak. However, this large peak is not significant in the XAS spectra due to small transition matrix elements for $2p \rightarrow 4s$ excitations compared to $2p \rightarrow 3d$ transitions. This was attributed to the high localization of $3d$ orbitals and the nodal structure of $4s$ states [257]. Therefore, the XAS double-peak structure is almost entirely mediated by unoccupied d orbitals.

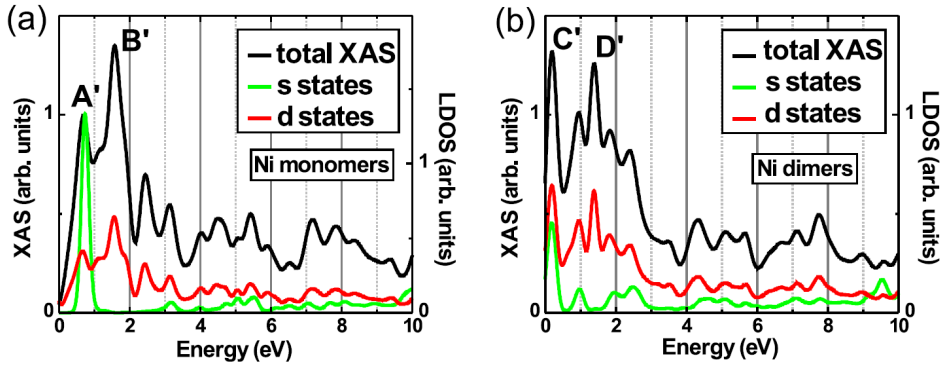

Figure 6.3: Simulated XAS of Ni on graphene. - Spin-averaged XAS and LDOS of Ni s and d states for Ni monomers (a) and Ni dimers (b).

The results prove that the Ni d shell is not entirely filled. But what is the electronic configuration then? An electronic configuration close to the free atom (d^8) or the bulk (d^9) can be excluded since no magnetic moments are formed, as can be seen from the absence of an XMCD signal. Moreover, we observe

no magnetic moment in our DFT calculations at all in agreement with previous theoretical works [181, 252]. This allows for the following conclusion: The Ni d shell is not completely filled, but the amount of holes is very small ($\lesssim 0.1$, see Fig. 6.1). The reason for the absence of magnetic moments despite a fractional d shell occupation can be understood from an Anderson impurity model in a static mean field (Hartree Fock) solution (see, e.g., Ref. [87]). Here, the necessary condition is that Coulomb energy gains have to overcome kinetic energy penalties when magnetic moments are formed. The gain of Coulomb energy upon formation of magnetic moments is $U(\langle n_\uparrow \rangle - \langle n_\downarrow \rangle)$ with U being the on-site Coulomb repulsion and $\langle n_{\uparrow,\downarrow} \rangle$ expectation values of the spin up/down occupation. Hence, to obtain a magnetic impurity, less kinetic energy must be paid than Coulomb energy gained: $U(\langle n_\uparrow \rangle - \langle n_\downarrow \rangle) > \pi\Delta$. In the system at hand, the hybridization function exceeds the Coulomb energy gain upon moment formation. Thus, no magnetic moments are formed.

The small amount of Ni d hole states can be traced back to a hybridization of the Ni d orbitals with graphene p_z states. The multipeak structure of the XAS spectra is caused by the anisotropy of this hybridization. From our calculations, we obtain a hybridization of Ni d_{z^2} and Ni s states, which forms the A' peak, while the B' peak is due to hybridization of Ni E_2 symmetry states (d_{xy} and $d_{x^2-y^2}$) and graphene p_z states, which form a van Hove singularity at this energy. States with E_2 symmetry were shown in Ref. [258] to couple exclusively to this van Hove singularity due to the symmetry of graphene states in the conduction band.

In the next step, we investigated the evolution of electronic and magnetic configurations under formation of Ni clusters. In the experiments, clusterization can simply be achieved by increasing the Ni coverage of graphene, which increases the probability for aggregation. XAS and XMCD measurements of Ni on graphene with high coverage are shown in Fig. 6.2b. Similar as in the low-coverage case, a multipeak structure can be observed with two pronounced peaks, named C (854.4 eV) and D (855.6 eV), which are located at different energies and exhibit modified relative intensities compared to peaks A and B. However, the most striking difference here is the occurrence of a clear XMCD signal near the L_3 edge (see also inset), which indicates magnetic moment formation.

We performed again electronic structure simulations of Ni on graphene, but this time for Ni molecules of different sizes. The XAS spectrum at the L_3 edge for

a Ni dimer (adsorption height: 1.60 Å) is depicted in Fig. 6.3b. The main peaks C' and D' reproduce well the experimental XAS curves: the C' peak exhibits a higher intensity than the D' peak, and the distance between both peaks is about 1.2 eV, in excellent agreement with the experimental C and D peaks at 854.4 and 855.6 eV. Compared to the Ni monomer spectra, the C' peak (at 0.2 eV), which corresponds to the A' peak at 0.7 eV, is shifted downwards by about 0.5 eV. Taking a look at the LDOS, we find again that the absorption spectrum follows the Ni d LDOS due to small transition matrix elements for $2p \rightarrow 4s$ excitations. The LDOS also reveals that the shift of the C' peak is due to increased spectral weight of d states above the Fermi level. This is caused by a hybridization of $4s$ orbitals of neighbored Ni atoms in the dimer, which depopulates the d shells and therefore leads to enhanced spectral weight above the Fermi level.

For the Ni dimer, it turns out that the depopulation of the d shell is not sufficient for the formation of finite magnetic moments. Hence, the Coulomb energy gain is not sufficient similar to the monomer case. However, with increasing cluster size, we find that sizeable magnetic moments can be formed, depending on the precise number of atoms in the Ni cluster. Our calculations show that clusters with more than four Ni atoms are sufficient to induce magnetic moments[1]. Most importantly, magnetic moments can be tuned by increasing the number of Ni atoms, yielding moments of about 0.85 μ_B per Ni atom in the limit of full graphene coverage. In this limit, Ni atoms are close to a d^9 configuration similar as in the bulk due to the amplified amount of electron transfer to the $4s$ shell. Thus, theory calculations provide insight into the nature of experimental XAS and XMCD. The modification of the two main peaks in the XAS spectra is due to the hybridization between neighboring Ni atoms in the cluster. The non-vanishing XMCD signal, which demonstrates the presence of finite magnetic moments, must originate from Ni clusters containing more than four atoms. As a result, the magnetic moment depends crucially on the number of atoms and the cluster shape. This allows for investigations of Ni-covered graphene with a tunable magnetism, simply by varying the Ni coverage in experiments.

[1]The magnetic moment formation is of course dependent on the cluster shape. For a four-atom cluster, we assume the Ni atoms to form a 2x2 block.

6.2 Evolution of correlations with the Ni cluster size

Transition metal systems are well-known to exhibit various phenomena related with the presence of strong electron-electron interactions. The many-body physics of various transition metal impurities on graphene have been extensively studied, mostly in theory (cf. Ref. [181] and references therein). The Ni adatom is a special case in this series, since the monomer is close to the d^{10} electronic configuration; the almost fully occupied $3d$ shell is expected to diminish the effects of electron correlations. However, it has been shown in this chapter that the electronic configuration in Ni clusters is tunable with the cluster size. Therefore, it is reasonable to assume that correlation effects evolve in Ni clusters when the d shell is emptied towards a d^9 configuration with increasing number of atoms in the cluster.

We consider again the Ni monomer, which is close to a d^{10} configuration, and verify whether correlation effects are reflected in the spectra. To this end, the Ni d LDOS has been calculated within GGA+U with Hubbard corrections and parameters $U = 4$ eV and $J = 1$ eV (technical details can be found in Ref. A.4.1). The results can be found in Fig. 6.4. Deviations between GGA and GGA+U are hard to discern, which is expectable for a nearly filled d shell. Due to the Hubbard U correction, the tiny double peak structure of the first main peak at -1.4 eV is washed out, and both main peaks are slightly shifted towards the Fermi level by about 80-100 meV.

More pronounced correlation effects on spectra are expected to occur in the opposite case of infinitely large Ni clusters, thus, a fully occupied graphene sheet. This is because the Ni atoms go towards the bulk d^9 configuration, which has been shown above to facilitate magnetic moment formation. In order to obtain an accurate picture of electron correlations in this open $3d$ shell system, DFT++ calculations were performed (cf. Sec. 2.8.2 for a brief overview). DFT++ can take dynamical correlations into account and is therefore superior to (static) DFT+U. For the DFT++ calculations, a correlated subspace of $3d$ electrons was extracted from the DFT Hamiltonian and further processed by means of a home-built interface between the "DFT" and the "++" part (developed by M. Karolak and O. Peil [259, 260]). Since the Ni atoms in the limit of full coverage form a regular 2D lattice, a dynamical mean-field theory (DMFT) treatment of the resulting lattice problem was employed. For simplicity, the interaction was

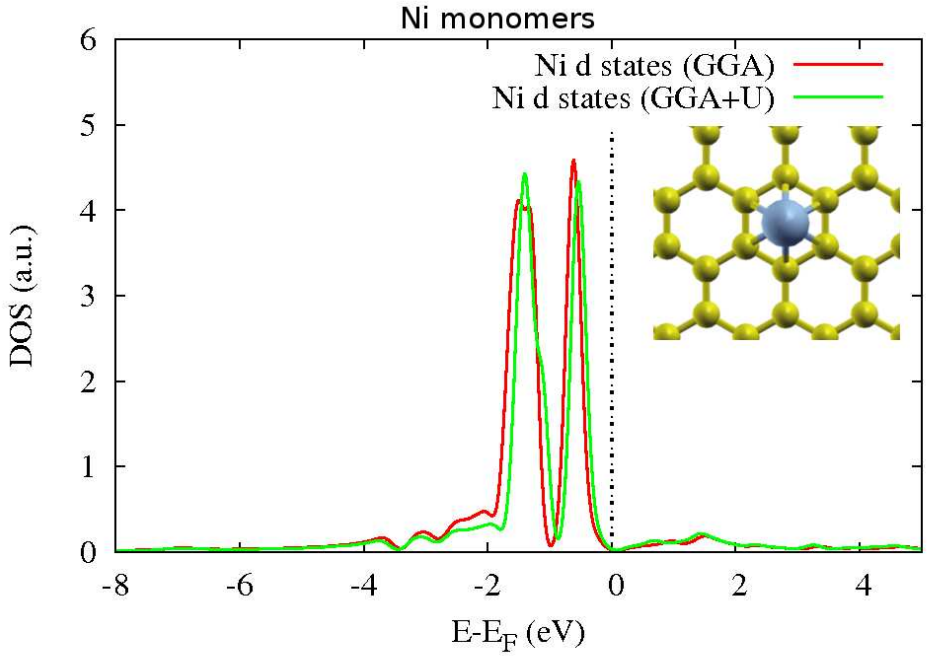

Figure 6.4: Simulated Ni monomer d LDOS. - The LDOS has been calculated using GGA (red line) and GGA+U (green line).

reduced to a density-density type only, and the calculations were performed in the paramagnetic phase. The effective Anderson model was solved by means of a continuous time quantum Monte Carlo (CT-QMC) solver in a segment picture (for technical details, see App. A.4.1).

The resulting spectra of Ni d states are plotted in Fig. 6.5. There are some noticeable deviations between the GGA (red curve) and the GGA+DFMT (green curve) spectra. First, one notices the presence of a 6 eV satellite in GGA+DMFT, which is well-known from bulk Ni [262]. Furthermore, one main peak, located at ~ -1.5 eV in GGA, is shifted downwards by about 0.8 eV and broadened in GGA+DMFT, leading to a nearly opposite distribution of spectral weight below the Fermi level. The main peak at the Fermi level, which controls the filling of the d shell, is slightly sharpened, while other peaks are shifted. Altogether, there are significant differences between GGA and GGA+DMFT away from the Fermi level. Interestingly, the 6 eV satellite is not the only property known from the bulk. Indeed, the Ni atoms exhibit a similar electronic configuration as the isolated bulk system, which has a d^9 filling. This is partly owing to the hollow site

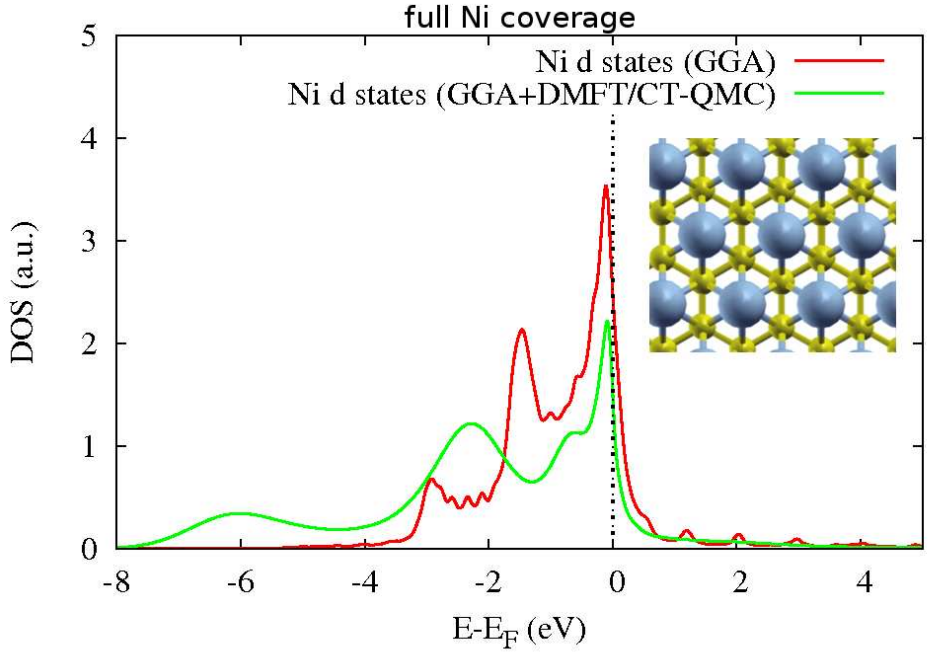

Figure 6.5: Simulated Ni d LDOS at full Ni coverage of graphene (infinitely large Ni clusters). - The LDOS has been calculated using GGA (red line) and GGA+DMFT (green line). In the QMC calculations, the temperature has been set to $\beta = 20$ eV^{-1}. The QMC spectra were obtained by employing the maximum entropy method [261] for analytical continuation of the Green's function.

position of the Ni atoms, which avoids distortions of the Ni atoms on graphene, and the fact that graphene and Ni exhibit similar lattice constants. Due to the strong orbital-selective coupling of Ni d states to graphene and the 2D nature of the Ni layer, there are, naturally, differences between spectra of bulk Ni (cf. Ref. [262]) and Ni monolayer on graphene. However, the fact that many features of bulk Ni are preserved in a Ni monolayer adsorbed on graphene is rather surprising: the previous chapter on the graphene/Ni(111) interface (5.3) led to the conclusion of surface state quenching and strong modifications of Ni(111) surface states due to graphene.

The correlation effects in the Ni monolayer on graphene are so pronounced that these should be easily observable in, e.g., photoemission experiments. The tuning of correlations, from almost zero in the case of single Ni adatoms (monomers) to the strongly correlated system at large Ni clusters (monolayers), might be achieved simply by varying the Ni coverage on graphene in experiments. To

conclude this chapter, we have not only demonstrated the tunable magnetism in Ni clusters on graphene (Sec. 6.1). Moreover, we predict from GGA+DMFT simulations the emergence of strong correlations in large clusters with increasing number of atoms. The underlying mechanism is the hybridization of neighboring Ni atoms, which fills the $4s$ shell and empties the $3d$ orbital, leading eventually to an open d shell system with large influence of electron-electron interactions on spectra.

7

K_2CuF_4, a two-dimensional ferromagnet

7.1 The lack of ferromagnetic 2D crystals

The 2D materials available today (see discussion in chapter 3) cover a number of electronic properties, from wide-gap insulators such as h-BN, over semiconducting MoS_2 and semimetallic graphene to superconducting BSCCO. This rich diversity of electronic properties is the precursor for novel van-der-Waals heterostructures with tailored properties and a tremendous potential for nanoelectronic applications. Two examples of these heterostructures (graphene/MoS_2 and graphene/h-BN hybrids) are discussed in Sec. 4, where also a brief overview of their nanoelectronic applications and novel phenomena is given.

The large variety of properties of these novel materials however does not feature any aspects of magnetism. Free-standing individual magnetic 2D crystals could not be produced so far, and their existence would not only be of fundamental interest on its own, but furthermore pioneer magnetic 2D-based heterostructures. In this chapter, we propose a way to realize free-standing 2D ferromagnetic crystals by exfoliating atomically thin films of the magnetic bulk material K_2CuF_4. Furthermore, a discussion will be given about the promising prospects that would result from the first realization of isolated 2D ferromagnets. It should be emphasized that quasi-2D ferromagnets have been realized decades ago, but these materials required the presence of a substrate to ensure their chemical stability. In contrast, the system proposed here will be predicted to form a free-standing magnetic 2D membrane without the need of a substrate. Importantly, the truly

2D nature would turn K_2CuF_4 into the first truly 2D magnetic spin model system in experiments, which would allow for systematic studies of the nature of the Kosterlitz-Thouless transition. This chapter is based on the results published in the article in Ref. [263].

7.2 Cleavage, structure and stability of 2D K_2CuF_4

The bulk material K_2CuF_4 was intensively investigated long ago, and it took over a decade to find a consensus about its actual crystal structure [264, 265, 266]. The 3D crystal is formed by layers, with each layer consisting of three planes, one Cu-F_2 plane and two K-F planes below and above (Fig. 7.1). The Cu atoms have in total six F neighbors, four in the Cu-F plane, and one in each K-F plane respectively, located on top or below the Cu atom. Importantly, the F atoms of the Cu-F plane are Jahn-Teller distorted, which lowers the symmetry of the otherwise tetragonal system to an orthorhombic lattice symmetry. K_2CuF_4 is a member of the K_2MF_4 perovskite class, with M =Mn, Fe, Co, Ni, Cu symbolizing a $3d$ transition metal [267].

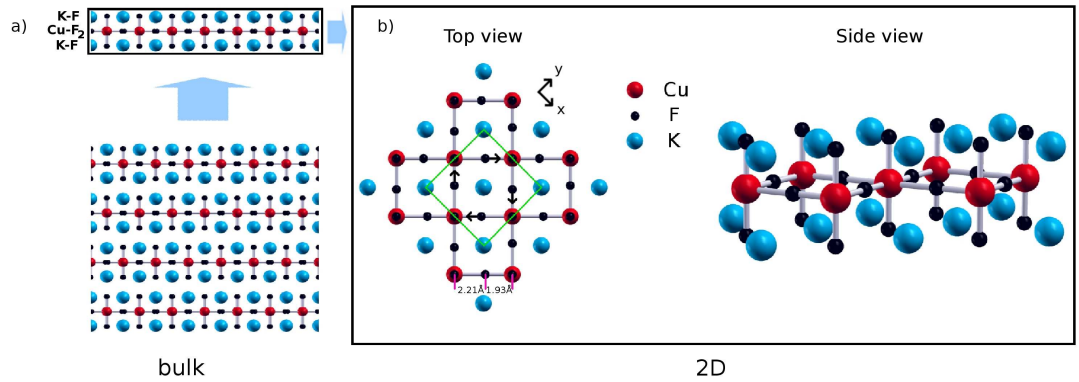

Figure 7.1: Bulk and 2D K_2CuF_4. - (a) Side view on the crystal structure of bulk K_2CuF_4. (b) Crystal structure of the exfoliated 2D layer from a top and a side view. Small black arrows denote Jahn-Teller distortions (see text) and the green lines symbolize the square unit cell of the 2D layer. To ensure lucidity, only Cu-F bonds are shown by gray lines.

A precondition for the exfoliation of monolayers is a weak interlayer binding in the bulk. A reasonable quantity to judge the feasibility of an exfoliation is the cleavage decohesion energy. We simulated the energetics of a cleavage procedure by introducing a fracture in the bulk crystal and varied the width of the fissure d

(for calculation details, see App. A.5). The cleavage energy $E_{\mathrm{cl}}(d)$ is depicted in Fig. 7.2. From the asymptotic limit, the ideal cleavage decohesion energy [268] can be extracted. The cleavage energies were obtained from LDA calculations with and without van der Waals (vdW) corrections in the scheme of Grimme [73] in order to estimate upper and lower boundaries. Local Hubbard U corrections, which play an important role for electronic and magnetic properties of the system (see below), turned out to be irrelevant for the interaction between layers and were therefore neglected (App. A.5.3). The obtained ideal cleavage decohesion energies are 0.78 J/m^2 with vdW corrections and 0.53 J/m^2 without. These values are comparable to other van der Waals solids: experimental estimations of the cleavage energy in graphite are about 1.5-2 times higher than our results for K_2CuF_4. For the cleavage procedure, the cleavage strength [268] is another useful quantity, given by the maximum value of the derivative of $E_{\mathrm{cl}}(d)$. We obtain 5.7 GPa and 4.4 GPa with and without vdW corrections, respectively.

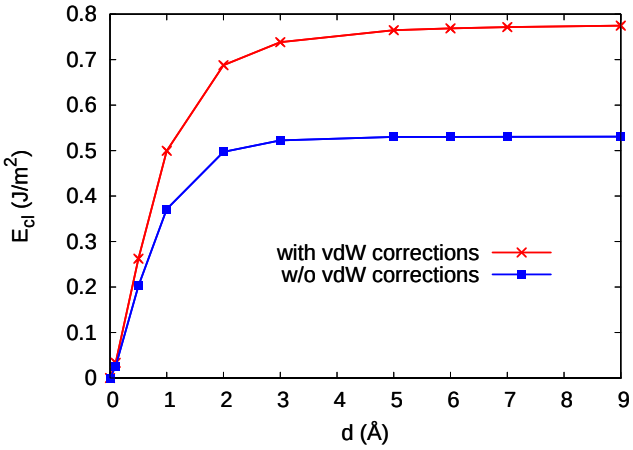

Figure 7.2: Energetics of the cleavage procedure in K_2CuF_4. - The cleavage energy E_{cl}, which has to be overcome in an exfoliation procedure, calculated with and without van der Waals corrections. The width of the fracture d is defined with respect to the equilibrium interlayer spacing of 2.6 Å.

A comparison between the bulk cleavage energies and the binding energies of the isolated bilayer shows that both energies are virtually identical. This can be attributed to the weak interaction between single layers and the far distance between next-nearest layers ($\sim$ 9 Å). This ensures not only the feasibility of exfoliation down to the monolayer, but also indicates that possible interactions between few-layer K_2CuF_4 and substrates are independent of the layer number.

The bilayer binding energies of other 2D crystals turn out to be only slightly larger. For instance, the calculated bilayer energy of K_2CuF_4 is only 2-3 times larger than theoretical values for bilayer graphene [63, 269] and 1.5-2 times higher than for Bi_2Se_3 [270]. Therefore, it is safe to state that the interlayer binding in bulk K_2CuF_4 is low enough to produce single-layers of this material, as has been done for many others [4, 5]. One possible technique mighty simply be the Scotch tape method.

Although the interlayer binding in bulk K_2CuF_4 is weak, possible structural changes under an exfoliation must be verified. A cleavage procedure might especially affect the Jahn-Teller distortions, which are crucial for the magnetism in the material. We carefully checked for structural modifications in our simulations by relaxing the atom positions in the 2D layer. Beforehand, we tested the performance of our simulations (see App. A.5.2) and reproduced the experimentally known structure. In particular, the positions of the Jahn-Teller atoms in the bulk agreed perfectly with the literature. Afterwards, we checked the 2D layer and found only slight modifications of the distortions. Overall, the structural properties of K_2CuF_4 turned out to be not sensitive to layer cleavage. As a consequence, the 2D layer as shown in Fig. 7.1b contains two formula units (14 atoms in total) in a quasi-2D square unit cell.

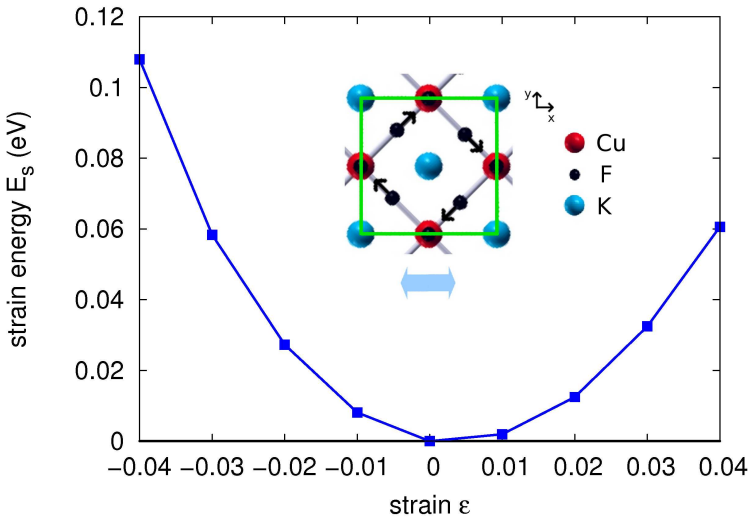

Figure 7.3: Energetics of uniaxial deformation. - Strain energy E_s as a function uniaxial strain ε. The unit cell shown in the inset sketches the simulated tension ($\varepsilon > 0$) and compression ($\varepsilon < 0$) direction.

For feasibility of future experiments on 2D K_2CuF_4, it is important to judge aspects of the chemical stability of such compounds, in particular with regard to the necessity of a substrate. If the in-plane stiffness of the material is high enough, substrates will not be required and experiments on the free-standing material might be performed. To judge the applicability of K_2CuF_4 in experiments, some elastic properties of the materials must be considered. From first-principles calculations, one can easily derive elastic constants such as the 2D Young's modulus, which can be formulated for the 2D square lattice as

$$Y_{2D} = \frac{1}{A_0} \frac{\partial^2 E_s}{\partial \varepsilon^2}\Big|_{\varepsilon=0}, \tag{7.1}$$

with E_s the strain energy, ε the uniaxial strain and A_0 the unit cell area in the equilibrium. The strain energy as a function of the strain is plotted in Fig. 7.3, from which we extract $Y_{2D} = 44.8$ N/m. This value is about 13% of the 2D Young's modulus in graphene, as has been reported in Ref. [271]. In the same paper, the authors fabricated free-standing graphene beams that were supported only from one side, which the authors attribute to the low bending of graphene due to the high in-plane stiffness of graphene. In analogy, we estimate the bending of K_2CuF_4 flakes of similar length l and width w. An estimation of the out-of-plane deformation h is then given by an anharmonic expression: $h/l \approx (\rho g l / Y_{2D})^{1/3}$ [271]. Inserting the simulated value of $Y_{2D} = 44.8$ N/m and the density $\rho = 2.1 \times 10^{-6} kg/m^2$ of K_2CuF_4, we obtain $h/l \approx 10^{-3} - 10^{-4}$ for a flake of length $l \approx 100$ μm. This is not more than one magnitude larger than in the ultrastrong material graphene, where $h/l \approx 10^{-4}$. Hence, even large flakes will not collapse under their own weight, which ensures stability of samples under vibrations or significantly large extra loads. Importantly, we find in our simulations that the Jahn-Teller distortions are stable under in-plane deformations. This ensures the stability of the magnetism, which is discussed in the next section.

7.3 Magnetism of 2D K_2CuF_4

The downsizing of magnetic materials up to atomically small nanomagnets is the ultimate goal of current research on magnetism. Magnetism in atomically thin films could so far only be realized by means of supporting substrates [272, 273, 274]. 2D K_2CuF_4, in contrast, fulfills the criteria to form a free-standing membrane, and offers the possibility to produce a truly 2D magnetic crystal. At first

sight, the truly 2D nature of K_2CuF_4 raises the question of the stability of the magnetism, since long-range magnetic order in a 2D system is excluded by the Mermin-Wagner theorem [275]. However, a quasi-long range ordering effect in the 2D XY model, the Kosterlitz-Thouless transition, might pave the way to a ferromagnetic phase for K_2CuF_4. In the bulk, indeed two critical temperatures were identified, the Curie temperature T_C and the Kosterlitz-Thouless temperature T_{KT}. In order to predict the feasibility of experiments on magnetic 2D K_2CuF_4, several criteria need to be fulfilled: 1. Although the layer-layer binding is weak, 3D interaction can be very relevant for the Kosterlitz-Thouless magnetism. Hence, the magnetism of the bulk [266, 267] must be preserved in the exfoliated monolayer at zero temperature. 2. In practice, strains and deformations will occur in real samples, and the magnetism should be robust against these perturbations. 3. In the 2D layer, T_{KT} must be high enough to allow for experiments.

The robustness of the Jahn-Teller distortions in the system plays a decisive role for the first two conditions. We found that the fully relaxed 2D layer conserves the Jahn-Teller distortions, yielding a magnetic moment of 1 μ_B per Cu atom. The magnetic moments turned out to be stable under applying strains as well. This stability is remarkable, since ferromagnetism in isolated 2D crystals has only been predicted theoretically for artificially strained layers of $NbSe_2$ and NbS_2 [276]. To shed light on the mechanism behind the stability of the magnetic moments in 2D K_2CuF_4, we consider the DOS of the system (Fig. 7.4, blue lines). The DOS was calculated using the LDA+U method [80] with a realistic value of $U \approx 8$ eV (for details cf. again App. A.5.4). The system exhibits a large band gap of more than 3 eV, which is sensitive to the choice of U. For $U = 0$, the gap is only as small as 0.3 eV. The gap separates the occupied states from a pronounced hole state in the spin-down channel, which we identify to be responsible for the ferromagnetism. It is mostly of $d_{z^2-r^2}$ orbital type (Fig. 7.4, red line) and, importantly, robust under deformations. For uniaxial strains, we find that the hole state is shifted in energy by not more than some hundred meV. Hence, deformations of realistic amplitudes will not quench the hole state and therefore prevent the magnetism, which is accompanied by the presence of Jahn-Teller distortions.

To gain a better understanding of the magnetic moment formation, we look at the band structure of the system (see Fig. 7.5a,b). First of all, a direct band gap can be observed. Since the primitive unit cell consists of 2 formula units (14

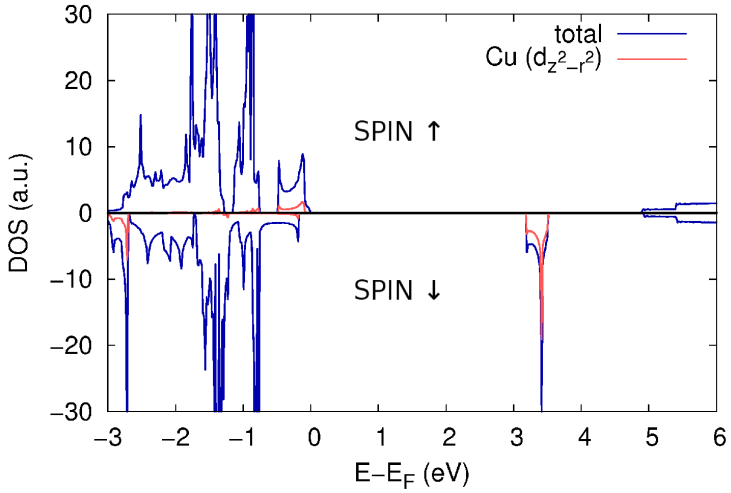

Figure 7.4: DOS of 2D K_2CuF_4. - Spin-polarized total DOS (blue lines). The projected DOS reveals the $d_{z^2-r^2}$ character of the hole resonance above 3 eV (red lines).

atoms), a considerable number of bands is visible below the Fermi level. Using the "fat bands" technique, we emphasize bands of Cu $d_{z^2-r^2}$ character by red color. Here, we find remarkable differences in the spectral weight distribution between both spin channels. In the spin-up channel, large spectral weight is located around -6 eV, while no states exist in this energy window at all in the spin-down channel. Instead, a similar state is now located above the Fermi level, which we identify as the hole state at ~ 3.2 eV.

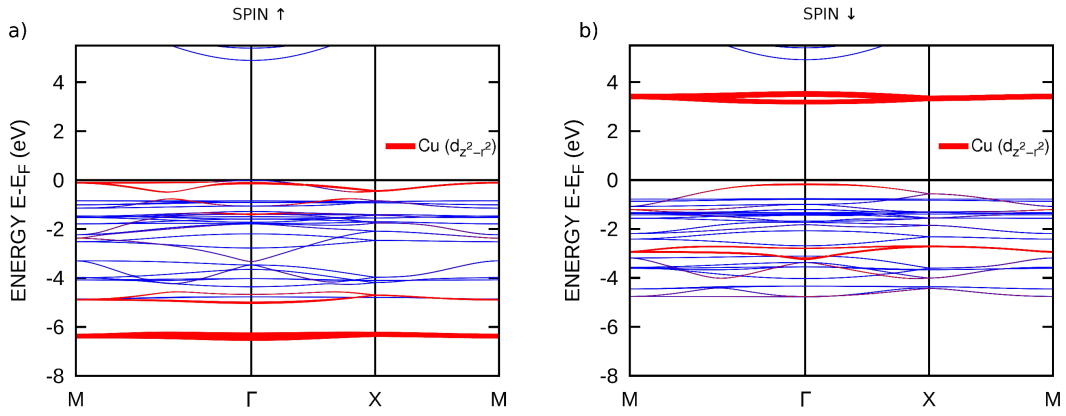

Figure 7.5: Band structure of 2D K_2CuF_4. - Energy bands in the spin-up (a) and the spin-down channel (b). Red "fat bands" visualize the Cu $d_{z^2-r^2}$ character of the bands.

The magnetism is generated by means of the following effect: the Jahn-Teller distortions, i.e., alternate Cu-F bond lengths, induce a peculiar orbital ordering at Cu sites that can be traced back to an alternate occupation of $d_{z^2-x^2}$ and $d_{z^2-y^2}$ orbitals (Fig. 7.6). This is in conjunction with the $d_{z^2-r^2}$ hole state, which is a linear combination of $d_{z^2-x^2}$ and $d_{z^2-y^2}$ orbitals. We also tested the effect explicitly for a geometry without Jahn-Teller distortions by enforcing equal Cu-F bond lengths. In this case, we find an ordering of antiferromagnetic type, which confirms that only the interplay of Jahn-Teller distortions and the alternate $d_{z^2-x^2}/d_{z^2-y^2}$ occupation allow for feromagnetism. This mechanism is already known from the bulk [266] and the fact that it is conserved in the monolayer is of critical importance for experiments on the isolated 2D system.

Thus, the first two conditions for a magnetic 2D layer are fulfilled: magnetic moment formation survives in the monolayer and the moments are robust against strains. In practice, however, the third condition of a sufficiently high Kosterlitz-Thouless temperature is crucial for experiments. The transition temperature is closely related with the magnetic anisotropy. In the bulk, the in-plane anisotropy was found to be weak [277]. We performed *ab initio* calculations (App. A.5.4) of the magneto-crystalline anisotropy (MCAE) in the 2D system. We found that the easy axis of the bulk is preserved: it lies in-plane but is undirected within the plane. It is not obvious that the bulk easy plane is preserved in the monolayer: there is a finite chemical interaction between two K_2CuF_4 layers, although the magnetic interlayer coupling, which is only about 0.1% of the intralayer magnetic coupling, is small.

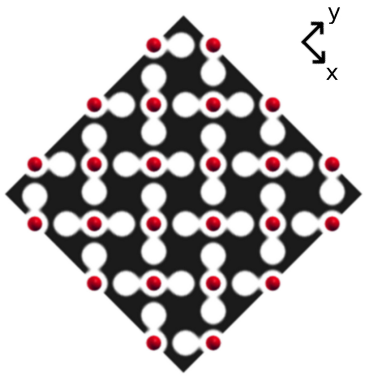

Figure 7.6: Orbital ordering in 2D K_2CuF_4. - Density of the hole state at ∼3.5 eV (0.35 – 0.55e/unit cell) in black/white colors. Red dots illustrate Cu atoms.

The monolayer thus constitutes, from a model point of view, a model system consisting of a square lattice of spin-1/2 sites, with the spin direction lying in-plane. This allows for experimental studies on an effective 2D Heisenberg model. Similar as for the bulk, the Heisenberg Hamiltonian can be written as [278]

$$H = -\frac{1}{2}\sum_{\langle i,j\rangle} J\left[S_i^x S_j^x + S_i^y S_j^y + \eta S_i^z S_j^z\right], \tag{7.2}$$

whereby $J > 0$ constitutes the ferromagnetic nearest-neighbor coupling, and $1-\eta \ll 1$ the small in-plane anisotropy. We can connect our first-principles calculations with the model Hamiltonian by evaluating DFT total energy calculations to estimate model parameters J and η: $J = E_{\mathrm{fm}} - E_{\mathrm{afm}}$, whereby E_{fm} is the total energy of the ferromagnetic system and E_{afm} the total energy of the system with enforced antiferromagnetic ordering. The parameter η can be directly extracted from the MCAE calculations. Our simulations yield $J/k_{\mathrm{B}} = 25.3$ K and $\eta = 0.90$. According to Ref. [278], this allows calculating the Kosterlitz-Thouless temperature (T_{KT}) by means of the renormalization group method as

$$T_{\mathrm{KT}} = \frac{2\pi J S^2}{\ln\left(\sqrt{\frac{T_{\mathrm{KT}}/JS}{1-\eta}}\right) + 2\ln\left(\frac{2}{T_{\mathrm{KT}}/2\pi JS^2}\right) + C}, \tag{7.3}$$

where $C = -0.5$ is a constant used for the bulk system. In this fashion, we end up with $T_{\mathrm{KT}} = 7.9$ K, which is close to the Curie temperature of the bulk system ($T_{\mathrm{C,bulk}} \sim 6.3$ K). Experimentally, the transition temperature T_{KT} can be easily reached by Helium cooling. Thus, all properties of 2D K_2CuF_4 indicate the feasibility of experiments on a free-standing, exactly 2D ferromagnetic crystal.

7.4 Magnetic 2D crystals - Prospects

K_2CuF_4 is only one of many possible materials suitable for the fabrication of truly 2D magnetic crystals. Our results indicate that K_2CuF_4 fulfills all properties required for a stable ferromagnetic 2D membrane. The possibilities for future experiments as well as novel applications are numerous.

Besides a fundamental interest in ferromagnetic atomically thin films, 2D K_2CuF_4 offers a large number of possibilities for new experiments on heterostructures of atomically thin materials. For instance, it might be used in graphene-based heterostructures as a spin-polarized electrode or in order to induce magnetic

moments that could be tuned via external fields. Another interesting possibility is to use 2D K_2CuF_4 as a magnetic overlayer on surfaces of topological insulators. In this way, band gaps in the (topologically protected) surface states [279] may be opened.

Beyond various applications in heterostructures, there is a broad research interest in the nature of the Kosterlitz-Thouless transition. In bulk K_2CuF_4 (and all other bulk materials with a Kosterlitz-Thouless transition), two phase transitions occur with two characteristic temperatures: the Curie temperature and the Kosterlitz-Thouless temperature. However, the Kosterlitz-Thouless transition in the bulk is interfered by 3D interactions [280]. This is in analogy to the differences between graphene and bulk graphite: Dirac states are not absent in graphite (they exist at the Brilluoin zone boundary), but they are "hidden" by parabolic dispersion quasiparticles due to layer-layer interaction. Only the isolation of graphene monolayers facilitated experimental access to Dirac states. In analogy, with 2D K_2CuF_4, we demonstrate a way to perform experiments on a Kosterlitz-Thouless system without perturbations through 3D interactions. K_2CuF_4 would allow for systematic studies of the Kosterlitz-Thouless transition in the future. For instance, efforts could be made to increase the Kosterlitz-Thouless temperature by doping through substituent atoms (such as Sr). Also, the physics of magnetic vortices may be studied, which would be present in a 2D Kosterlitz-Thouless system. First results of a recently started project together with R. Nair (U Manchester) on another 2D material, hexagonal $CrCl_3$, look promising.

8

Summary and Outlook

The different 2D crystals studied in this thesis cover a large parameter space and reveal a diversity of phenomena. Simultaneously, the number of possible combinations into van der Waals heterostructures is practically infinite. One goal of this thesis was to investigate the electronic properties of the most frequently studied 2D-based heterostructures at this time, graphene/h-BN and graphene/MoS_2 interfaces. For graphene/h-BN, there is on-going discourse about the formation of moiré superlattices and the presence of a spectral gap. Our work showed that moiré superstructures reduce absolute band gaps due to the spatial cancellation of mass terms acting on Dirac fermions. For an accurate judgement of elastic properties and mechanical strength, a consideration of van der Waals interactions beyond simplest DFT is crucial. Future efforts should be made in order to merge model calculations from the sub-Å to the moiré periodicity of more than 10 nm, with the ultimate goal to understand the conditions responsible for inconsistent experimental results on moiré formation and electronic properties.

The rather applied project on graphene/MoS_2 hybrids is a good example for the interplay of multiple doping mechanisms in realistic nanosystems, which eventually facilitate an application as a photodetector. In analogy to graphene/h-BN hybrids, the role of defects in these systems turns out to be counter-intuitive. While in graphene/h-BN midgap states are induced by carbon impurities located in the neighboring boron nitride layer, common defects in MoS_2, such as sulfur vacancies, do not affect graphene. Instead, substitutional rhenium impurities in the inner molybdenum plane dope graphene with electrons, which, in combination with a MoS_2 edge, allows for efficient separation of photo-induced electron-hole pairs in graphene. The role of inhomogeneities in graphene heterostructures is

far from being understood; for instance, defects in h-BN are suspected to mediate vertical carrier transport even at zero field. This calls for a comprehensive transport theory.

Apart from heterostructures, the influence of graphene sheets on metallic substrate properties was studied in this thesis. Graphene on a magnetic Ni(111) surface quenches the Ni surface state, which reverses spin polarization in the vacuum. Due to strong binding and sublattice symmetry breaking, the Dirac cone vanishes, and only one graphene sublattice is visible in STM topography images. In STS spectra, the contributions of graphene atoms to the tunneling current are much lower than from the Ni atoms, which is unexpected above a graphene surface. Interestingly, a similar invisibility of graphene states is observed on Ir(111), although graphene is only weakly bound to the Ir substrate. Graphene also affects Ir properties by shifting the Ir surface resonance. The results corroborate that STM/STS spectra of graphene/metal interfaces have to be interpreted carefully. Another local probe technique, XAS, was topic of our study on Ni adsorbates on graphene. XAS simulations revealed the magnetic and electronic configurations of Ni monomers and clusters. Most importantly, graphene can be used as a scaffold to manipulate the size of Ni clusters for the purpose of tunable magnetic moment generation. Furthermore, GGA+DMFT calculations demonstrated the emergence of electronic correlations in the case of large clusters, an effect related to the depopulation of the *d* shell.

Finally, the motivation of the study of 2D K_2CuF_4 is a proposal to fabricate Kosterlitz-Thouless magnetic materials in experiments. Although a second-order ferromagnetic phase transition does not exist in a strictly 2D crystal, the Kosterlitz-Thouless transition does provide a ferromagnetic phase in 2D K_2CuF_4 below about 8 K. Crucially, it turns out that the chemical stability of the crystal is sufficient to either form a free-standing magnetic membrane, or to interface K_2CuF_4 with graphene or topological insulators. Imaginable applications are countless, while at the same time the system would be the first realization of a truly 2D magnetic crystal. Further studies of 2D magnetic materials have already started that raise hope for the feasibility of magnetic 2D crystals in the near future.

Appendix A

Appendix

A.1 Graphene/h-BN

A.1.1 Computational method

A.1.1.1 Graphene on pristine h-BN

Simulations of the graphene/h-BN system were performed with the Vienna *ab initio* simulation package (VASP) [164]. The (unrotated) moiré consisting of a 56x56 graphene layer on top of a 55x55 layer of h-BN would contain more than 12000 atoms, which is out of reach for DFT-PAW methods even in a supercomputer. Therefore, we restrict to small unit cells of 4 atoms with the graphene lattice being enforced to match the h-BN lattice. A vacuum of 25 Å was employed. We constructed the unit cells with six different local stacking configurations as shown in Fig. 4.2a. The order of configurations can be viewed as a sequence of snapshots being realized when the graphene sheet is translated downwards by half a B-N bond length for each configuration. The enforced lattice constant was chosen as 2.49 Å, thus, graphene was stretched onto the LDA-optimized lattice constant of h-BN. In the computationally extremely demanding ACFDT-RPA calculations, the response function χ^{KS}, the RPA correlation energy E_c^{RPA}, and the exact exchange energy E_{EXX} were evaluated with LDA KS orbitals. We chose a kinetic energy cutoff of 347 eV for the response function and a plane wave cutoff of 520 eV together with a mesh of $7 \times 7 \times 1$ k-points. Although E_c^{RPA} and E_{EXX} require a higher cutoff to converge, it can be shown that the sum, which we calculate to obtain total energies, converges much faster [61], and the cutoff of 347 eV ensured satisfying convergence. To assess the quality of our RPA calculations, comple-

mentary LDA/GGA calculations were performed using a $24 \times 24 \times 1$ k-points grid and a kinetic energy cutoff of 500 eV. Furthermore, LDA/GGA calculations of a single h-BN sheet were performed using $15 \times 15 \times 1$ k-meshes and a 500 eV kinetic energy cutoff to calculate the elastic properties of a single h-BN sheet.

A.1.1.2 Graphene on defective h-BN

DFT calculations of carbon, oxygen, and antisite defects (Sec. 4.1.1.6) with 3x3 graphene supercells on top of two h-BN layers were performed with enforced lattice matching. The lattice matching effect is negligible here due to the significant resonances related with the C defects around the Fermi level. The stacking order was chosen to be according to configuration I (Fig. 4.2a), and the two h-BN sheets were stacked in A-A' order (eclipsed with B over N) analogous to the stacking in bulk h-BN [281]. The geometries were fully relaxed. The LDA functional was employed and a k-mesh of 12x12x1 points was employed for Brillouin zone sampling. Cohesive energy calculations indicate the highest stability of C defects, while antisite defects are less stable, although interesting candidates for short-range scattering of graphene electrons, as well.

A.1.2 Cohesive energies

The stability of the defective heterostructure can be estimated from its cohesive energy. The cohesive energy can be calculated as

$$E_{\mathrm{coh}} = \frac{n_{\mathrm{B}}E_{\mathrm{B}} + n_{\mathrm{N}}E_{\mathrm{N}} + n_{\mathrm{C}}E_{\mathrm{C}} + n_{\mathrm{O}}E_{\mathrm{O}} - E_{\mathrm{tot}}}{N_{\mathrm{tot}}}, \tag{A.1}$$

with n_{B}, n_{N}, n_{C}, n_{O} the number of B, N, C, and O atoms in the unit cell, $E_{\mathrm{B}}, E_{\mathrm{N}}, E_{\mathrm{C}}, E_{\mathrm{O}}$ the respective total energies of the isolated atom, E_{tot} the total energy of the defective (fully relaxed) heterostructure, and N_{tot} the total number of atoms in the unit cell (54 in our simulations). Defects with the lowest cohesive energies (antisites, O substituting B) lead to strong distortions of the surrounding B and N atoms with considerable corrugations of partly more than 1 Å, which slightly buckles the graphene sheet above.

	prist.	C subs. B	C subs. N	O subs. B	O subs. N	B antis.	N antis.
E_{coh} (eV)	9.648	9.627	9.578	9.468	9.578	9.485	9.564

Table A.1: Cohesive energies of the pristine graphene/h-BN heterostructure, and with C, O, and antisite defects included.

A.2 Graphene/MoS_2

A.2.1 Computational method

The theoretical results obtained in this work were based on DFT calculations, which we performed using the Vienna ab initio simulations package (VASP) [164]. In Sec. 4.1.1.1 and in Ref. [119, 156, 282] it was shown that the local density approximation (LDA) to the exchange-correlation potential is better suited to describe van der Waals forces in weakly bound layered systems than generalized gradient (GGA) functionals. The simulations comprised large supercells of 50 C atoms, 32 S and 16 Mo atoms, and for simulations of impurities in the heterostructure, the atoms were replaced by a substituent or removed. In these simulations a k-mesh of 12x12x1 points and a plane-wave cutoff of 500 eV was employed.

For simulations of edge effects, computationally demanding calculations were performed of a graphene semi-plane, with one half of the graphene sheet covered by MoS_2. In this manner, a supercell of 8x1 unit cells as shown in Fig. 4.18 was constructed. In total, the unit cell contained 600 atoms, and we realized different edge configurations in the simulations. Furthermore, we considered the interplay of rhenium impurities and edge effects by including the same Re concentration as in Fig. 4.18, such that the impurities had a minimum distance to the MoS_2 edge of ~ 10 Å. For these calculations, we employed a 3x1x1 k-mesh and a plane-wave cutoff of 400 eV.

A.2.2 Sulfur vacancies and oxygen impurities in MoS_2

In Sec. 4.2, we proposed Re impurities in MoS_2 as a possible explanation for the electron-doping of graphene below MoS_2. To substantiate this, we exclude in the following other realistic impurities as a source of the doping. A natural candidate for a doping of graphene by MoS_2 could be sulfur vacancies in MoS_2. We checked the effect of S vacancies with the same setup as in the Re impurity

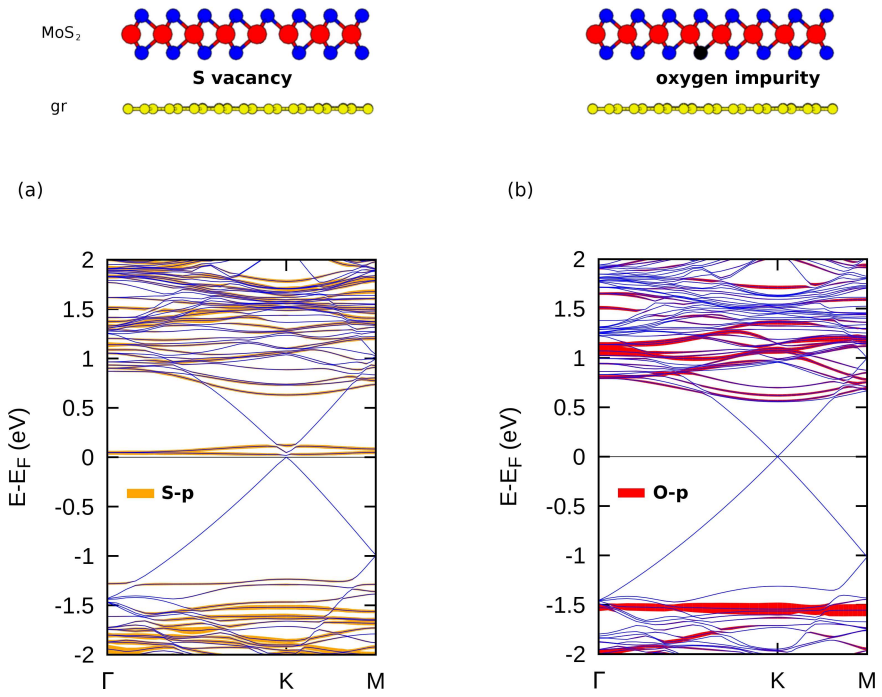

Figure A.1: Further defects in graphene/MoS_2. - (a) (top) Graphene-MoS_2 with sulfur defect from a side view. (yellow atoms: graphene, blue atoms: sulfur, red atoms molybdenum). The S defect is introduced by removing one S atom in the unit cell. (bottom) Band diagram (blue curves). p state contributions of S atoms next to the sulfur vacancy are depicted as orange fat bands. (b) The same for oxygen impurities. Red "fat bands" show p state contributions of the oxygen impurity.

simulations (see Fig. 4.18c). We simulated the vacancy by removing one of the 32 sulfur atoms between graphene and MoS_2, and relaxed the structure. The corresponding band structure can be found in Fig. A.1a. Obviously, there is no Fermi level shift, since the Dirac point lies on the Fermi level. Hence, there is no doping of graphene by S vacancies in MoS_2, even in this high impurity concentration. There are p states emerging above the Fermi level (orange "fat bands"), but these hole states do not significantly hybridize with graphene states, as can be seen from the intact Dirac cone.

XPS measurements performed by the group of K. Novoselov (U Manchester) exhibited a significant amount of oxygen in the samples. This indicates the presence of oxygen impurities, which substitute S atoms to form MoO_xS_{2-x} in the heterostructure. To exclude doping effects here, we did the same calculations as

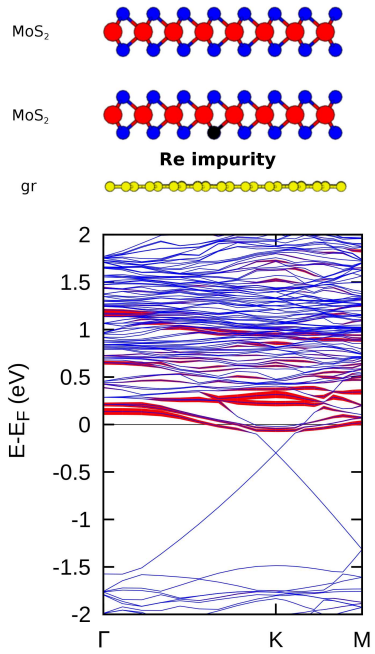

Figure A.2: Bilayer MoS_2 in graphene/MoS_2. - (a) (top) Side view on the system with two MoS_2 layers used (yellow atoms: graphene carbon, blue atoms: sulfur, red atoms: molybdenum). (bottom) Band structure (blue curves). The red "fat bands" visualize contributions of the Re d orbitals.

done for Re impurities and S vacancies, but this time with one S atom replaced by an oxygen atom, such that $x = 0.0625$ (Fig. A.1b). Compared to the pristine graphene/MoS_2 system, there are no crucial differences in the band diagram. This can be understood simply from the fact that sulfur and oxygen are both members of the chalcogen group in the periodic table. Hence, similar covalent bonds of S and O atoms with neighboring Mo atoms are formed. Overall, the band structure shows that oxygen p states (red colored "fat bands") in the system do not affect the electronic structure significantly.

A.2.3 MoS_2 thickness and temperature dependence of the doping

For measurements of the gate voltage response of the photocurrent, several layers of MoS_2 were deposited on graphene, which we neglected in our simulations of the system, where only one MoS_2 layer was considered. We tested explicitly the importance of multilayers in the calculations presented in Fig. 4.18. To do so, we added another MoS_2 layer to the system and recalculated the band structure.

The results are shown in Fig. A.2. There is only small difference in the Fermi level shift of approximately -15 meV and no qualitative differences to the band structure of the monolayer system shown in Fig. 4.18. Hence impurity doping in the interface is not sensitive to the thickness of the MoS_2 flake used in the experiment, and the modelled system can be directly compared to measurements on a heterostructure with a MoS_2 thickness of several layers.

Comparison to the experiment requires an understanding of the role of temperature effects. We checked the temperature effect on the Fermi level shift by weighting the calculated carrier density with the Fermi-Dirac distribution. The carrier density was exctracted from integrated projected densities of states. We find that measurements performed at room temperature (as in the photocurrent measurements) induce Fermi level shifts on the order of 10 meV, which is negligible. Thus, temperature-induced broadening does not play a role in the comparison between experiment and theory.

A.2.4 Charge reordering in graphene under different MoS_2 edge types

The charge redistribution effect in graphene below MoS_2 edges is discussed in Fig. 4.19, but restricted to the scenario of a $(\bar{1}010)$ edge. To secure our statements, we additionally investigated Mo-terminated $(10\bar{1}0)$ edges with additional S monomers and dimers adsorbed. Here the shape of the potential step in graphene below MoS_2 was found to deviate from the $(\bar{1}010)$ edge, which can be expected from the literature on isolated MoS_2 edges [196, 197]. However, for graphene below all considered edges, we find important similarities in the potential landscape. The shape of the potential barrier varies strongly, but its amplitude is always on the order of some hundred meV. Crucially here, the resulting electric field below any MoS_2 edge is directed such that redistributions move electrons to the uncovered side while holes reside in the MoS_2-covered part of graphene. Finally, we simulated an artificial edge structure, where we cut the MoS_2 flake laterally in both the zigzag and the armchair direction. This kind of edge is unlikely to occur in reality because of high formation energies. Furthermore, we did not saturate bonds or relax the geometry. An image of the simulated structure is given in Fig. A.3. The electronic states at armchair and zigzag states in MoS_2 nanoribbons are known to differ strongly [283], but the color map of the graphene p_z on-site energies in Fig. A.3 shows again a potential barrier similar to the realistic configurations discussed here and in Sec. 4.2.2. The on-site energies were calculated

by

$$E = \frac{\int_{-\infty}^{E_F} \epsilon \rho(\epsilon)\, d\epsilon}{\int_{-\infty}^{E_F} d\epsilon}, \tag{A.2}$$

with $\rho(\epsilon)$ the carbon p_z-DOS.

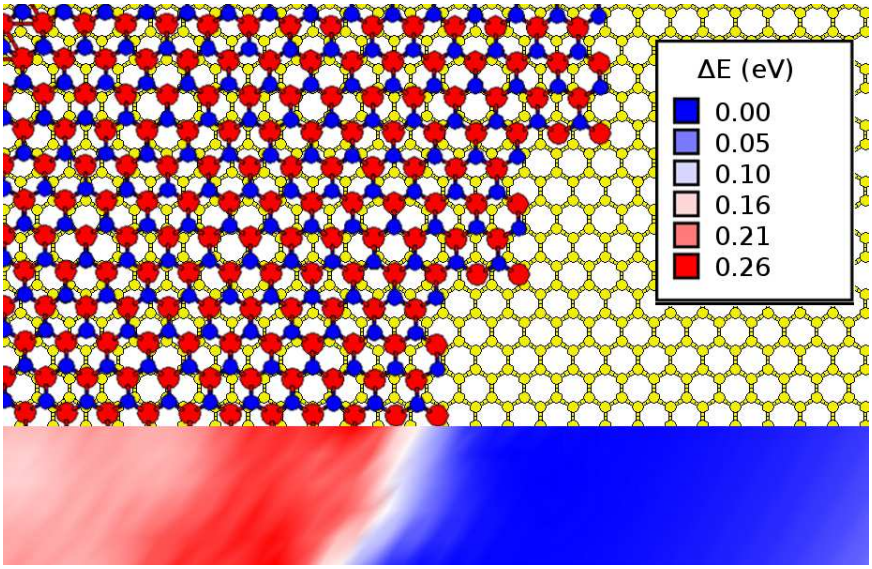

Figure A.3: Potential step of arbitrary shape. - Top view on the MoS_2-graphene heterostructure (yellow atoms indicate the graphene carbon atoms, blue atoms sulfur and red atoms molybdenum). The contour plot shows the on-site energy differences of graphene p_z orbitals.

To conclude this edge study, the potential landscape present below MoS_2 edges is manifold due to various different edge configurations that might occur in experiments. From transport experiments, we do not know the local subtleties of the potential landscape, but for our analysis of the photocurrent experiments, it is enough to know the rough amplitude of the barrier and the sign of the potential step, which is always the same for all investigated configurations. This allows for the conclusion that the photocurrent in the experiment is induced at the edge, where electron-hole pairs are sufficiently separated. This is supported by the symmetry in the photocurrent maps.

A.3 Graphene on metals

A.3.1 Graphene on Ir(111) - computational details

DFT calculations were carried out using VASP [164] and the PBE-GGA [32] to the exchange-correlation functional. To model the bare Ir (111) surface, a slab comprising 18 Ir layers was constructed with a lattice constant of 3.888 Å, and a large vacuum of 5.5 nm was employed. 15x15x1 k points were used for Brillouin zone sampling together with a kinetic energy cutoff of 400 eV.

For the graphene/Ir(111) system, the same unit cell was used with one side of the Ir slab coated by a graphene layer. Here, graphene was slightly stretched to match the Ir lattice constant. For band structure calculations, spin-orbit coupling was taken into account to ensure the Rashba splitting of Ir(111) surface states.

A.3.2 Graphene on Ni(111) - computational details

The VASP [164] package was utilized for DFT calculations and the PBE-GGA [32] functional was employed. Van der Waals interactions were considered by means of the DFT-D2 method [73]. Here, we used the experimental lattice constant of the bare Ni (111) surface, 2.49 Å, and the surface was constructed by a 15-layer Ni slab. Periodic images were separated by a vacuum of about 18 Å. For graphene on Ni(111), the surface was coated on one side of the Ni slab. The graphene lattice is known to conform to the Ni surface structure, thus, no moiré is formed. The geometries were optimized until forces were lower than 0.01 eV Å^{-1} and a k mesh of 36x36x1 points was employed for calculations of the LDOS.

STM images were simulated by calculating the spatially resolved LDOS, integrated in an energy window between -100 meV and 100 meV. For spin-polarized STS, empty spheres were placed in the vacuum at four different lateral positions and at a height of 3.6 Å over the bare Ni(111) surface or the graphene/Ni(111) surface. Thereby, the STM tip was assumed to be s-wave symmetric at the apex.

A problem of STS simulations is the presence of a tunneling barrier between the tip and the sample. The precise shape of the tunneling barrier is unknown and modified by an electric field between the tip and the surface [284]. A suitable approximation to the tunneling barrier shape is a trapezoidal form, leading to a modification of dI/dU spectra according to Ref. [285] as

$$\frac{dI}{dU} \sim \exp\left(-\int_0^s dz \left[\Phi + eU\frac{z}{s} - eU\right]^{-\frac{1}{2}}\right). \tag{A.3}$$

Thus, there is an additional dependence of the energy and the tip-height z (Φ is the work function and s the distance between the sample and the STM tip). This can be, expanded to first order in U, expressed as

$$\frac{dI}{dU} \sim c_0 \exp\left(-\frac{eU}{E_0}\right), \tag{A.4}$$

with c_0 and E_0 being material-specific constants, whereby E_0 depends on the distance between the sample and the tip. For comparison of simulated STS with experiments, we can therefore simply scale the vacuum LDOS by a factor $\exp(-E/E_0)$, whereby we optimize E_0 according to the experimental spectra. For the spectra plotted in Sec. 5.3, we find $E_0 = 2$ eV.

A.4 Ni adatoms and clusters on graphene - computational details

A.4.1 Ni on graphene

We performed a series of DFT calculations using two DFT codes, the VASP package [164] and WIEN2k [46]. We used the PBE-GGA exchange-correlation functional [32] and converged the spectra carefully with respect to the k mesh. The unit cell in the simulation was modeled by an impurity placed on a 3x3 graphene supercell comprising 18 carbon atoms. We employed 8 Å and 22 Å of vacuum between periodic images and relaxed the geometry within VASP. For XAS simulations, we employed the dipole correction and Fermi's golden rule. Tests of core hole effects showed little modification of the spectra. The tests were done by a forced ionization, i.e., by removing one electron from the core.

For Ni cluster calculations, monomers, dimers, and 4-atom oligomers were tested (all geometries were relaxed). We also considered the full coverage limit, for which a primitive graphene unit cell was employed.

DFT++ calculations were performed by means of an interface designed by M. Karolak and O. Peil, which is a general tool to connect the VASP code with impurity solvers for the purpose of DFT++ calculations. In this way, first-principles based Anderson impurity models can be carried out as well as quantum lattice models, which can be solved via DMFT.

The effective Anderson impurity model from the DMFT problem was solved by a CT-QMC (HYB) code in a segment picture. We used 2000 Matsubara frequen-

cies and Coulomb matrix parameters $U = 4$ eV with $J = 1$ eV (density-density interaction). The inverse temperature was chosen as $\beta = 20$ eV^{-1} (corresponding to 580 K). Ten DMFT self-consistency loops were performed for converged results. The double counting correction was included in the fully localized limit.

A.5 K_2CuF_4

A.5.1 Computational details

To simulate 2D and bulk K_2CuF_4 from first-principles, we performed DFT calculations with the VASP package [164].

A.5.2 Atomic structure

The LDA method was used to simulate the atomic structure of the system [23]. In test calculations for the bulk we found that the LDA perfectly reproduces Jahn-Teller distortions of the system, even in slightly better agreement with experiments than LDA+U [80]. We speculate that the reason for the performance of simple LDA lies in the cancellation of errors in the exchange and the correlation potential. We employed 8x8x1 (5x5x5) k points for the 2D layer (the bulk system) K_2CuF_4 together with a kinetic energy cutoff of 700 eV (single layer) and 500 eV (bulk). The lattice parameters were taken from the experiment (lattice constants $a = b = 5.8655$ Å [264]). To optimize the structure and to find the Jahn-Teller distortions, we relaxed atom positions in the unit cell until all forces on atoms were less than 0.02 eV/Å.

A.5.3 Cleavage energies

As we have discussed in Sec. 7.2, van der Waals interactions play an important role for the binding between K_2CuF_4 layers. GGA fails to estimate van der Waals interaction accurately. To obtain upper and lower boundaries for the interlayer binding energies, we performed calculations using LDA with and without van der Waals corrections within the DFT-D2 method of Grimme [73]. Furthermore, we found from LDA+U calculations that local Coulomb interactions are unimportant for the binding of K_2CuF_4 layers.

Binding energies of the bilayer and cleavage energies can differ in general from each other, due to the presence of many layers in the bulk near the cleavage

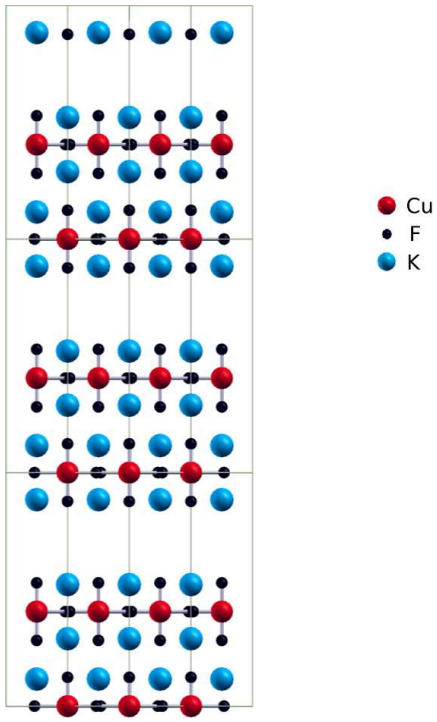

Figure A.4: Fracture in K_2CuF_4. - To simulate the cleavage fracture, a unit cell containing a bilayer with variable vacuum was constructed. Gray lines visualize the unit cell.

fracture. A bilayer system was simulated, for which we relaxed the atom positions in order to obtain the optimized bilayer binding energy. Subsequently, one of the layers was lifted far to the vacuum. The difference in total energies was then evaluated, which can be considered as the bilayer binding energy.

Afterwards, this energy was compared to the cleavage decohesion energy. To calculate the latter, a bulk unit cell as shown in Fig. A.4 was constructed. The layer number of only three per unit cell is justified because the distance between two fractures in such a geometry is more than 10 Å. To obtain the cleavage energy curves in Fig. 7.2, the fracture was varied by changing the c parameter of the cell.

Finally, we calculated the energetics of deformation, where we employed the LDA+U method. Here, an optimized lattice constant $a = b = 5.561$ Å was used, which differs by about 5% from the experimental value. This deviation had no important impact on the electronic structure and also reproduced the Jahn-Teller distortions and magnetic moments.

A.5.4 Magnetism and electronic structure

For band structure and DOS calculations, we employed the LDA+U method, which turned out to be well-suited to reproduce magnetic and electronic properties of the bulk. We employed the rotationally invariant formulation of LDA+U developed by Dudarev [286], where Hund's rule exchange J_{H} and the Hubbard Coulomb repulsion U enter into an effective Hubbard parameter $U_{\mathrm{eff}} = U - J_{\mathrm{H}}$. This avoids the problem of magnetic anisotropy dependence on the choice of J_{H} in LDA+U calculations [287]. For the spectra and band structures shown in the main text, we selected $U_{\mathrm{eff}} = 7.03$ eV, which had been used to simulate $KCuF_3$ [80]. For magneto-crystalline anisotropy (MCAE) calculations, a fine k-mesh (18x18x1) was employed and spin-orbit coupling was included. The MCAE parameter η was sensitive to the choice of the functional and structural properties. However, it enters only logarithmically in Eq. 7.3. We estimated explicitly that the MCAE ($\sim 10^{-4}$ eV) is clearly dominant over shape anisotropy contributions ($\sim 10^{-6}$ eV), therefore shape anisotropy effects are not relevant for the discussion.

References

[1] P. Avouris, Z. Chen, and V. Perebeinos. **Carbon-based electronics**. *Nature Nanotechnology*, **2**(10):605–615, 2007.

[2] K. S. Novoselov, A. K. Geim, S. V. Morozov, D. Jiang, Y. Zhang, S. V. Dubonos, I. V. Grigorieva, and A. A. Firsov. **Electric field effect in atomically thin carbon films**. *Science*, **306**(5696):666–669, 2004.

[3] K. S. Novoselov, A. K. Geim, S. V. Morozov, D. Jiang, M. I. Katsnelson, I. V. Grigorieva, S. V. Dubonos, and A. A. Firsov. **Two-dimensional gas of massless Dirac fermions in graphene.** *Nature*, **438**(7065):197–200, 2005.

[4] A. K. Geim and I. V. Grigorieva. **Van der Waals heterostructures**. *Nature*, **499**(7459):419–425, 2013.

[5] F. Bonaccorso, A. Lombardo, T. Hasan, Z. Sun, L. Colombo, and A. C. Ferrari. **Production and processing of graphene and 2d crystals**. *Materials Today*, **15**(12):564–589, 2012.

[6] J.-H. Lee, E. K. Lee, W.-J. Joo, Y. Jang, B.-S. Kim, J. Y. Lim, S.-H. Choi, S. J. Ahn, J. R. Ahn, M.-H. Park, et al. **Wafer-Scale Growth of Single-Crystal Monolayer Graphene on Reusable Hydrogen-Terminated Germanium.** *Science*, **344**(6181):286–289, 2014.

[7] L. Britnell, R. V. Gorbachev, R. Jalil, B. D. Belle, F. Schedin, A. Mishchenko, T. Georgiou, M. I. Katsnelson, L. Eaves, S. V. Morozov, N. M. R. Peres, J. Leist, A. K. Geim, K. S. Novoselov, and L. A. Ponomarenko. **Field effect tunneling transistor based**

on vertical graphene heterostructures. *Science*, **335**(6071):947–950, 2012.

[8] L. Britnell, R. M. Ribeiro, A. Eckmann, R. Jalil, B. D. Belle, A. Mishchenko, Y.-J. Kim, R. V. Gorbachev, T. Georgiou, S. V. Morozov, et al. **Strong light-matter interactions in heterostructures of atomically thin films**. *Science*, **340**(6138):1311–1314, 2013.

[9] P. Fulde. *Electron Correlations in Molecules and Solids*. Springer, 1995.

[10] R. M. Martin. *Electronic structure: basic theory and practical methods*. Cambridge University Press, 2004.

[11] R. G. Parr and W. Yang. *Density-functional theory of atoms and molecules*, **16**. Oxford university press, 1989.

[12] E. Pavarini, E. Koch, D. Vollhardt, and A. I. Lichtenstein. *The LDA+DMFT approach to strongly correlated materials*. Schriften des Forschungszentrums Jülich, 2011.

[13] R. O. Jones and O. Gunnarsson. **The density functional formalism, its applications and prospects**. *Reviews of Modern Physics*, **61**(3):689, 1989.

[14] E. Schrödinger. **Quantisierung als eigenwertproblem**. *Annalen der Physik*, **385**(13):437–490, 1926.

[15] M. Born and R. Oppenheimer. **Zur quantentheorie der molekeln**. *Annalen der Physik*, **389**(20):457–484, 1927.

[16] L. H. Thomas. **The calculation of atomic fields**. In *Mathematical Proceedings of the Cambridge Philosophical Society*, **23**, pages 542–548. Cambridge Univ Press, 1927.

[17] E. Fermi. **Eine statistische Methode zur Bestimmung einiger Eigenschaften des Atoms und ihre Anwendung auf die Theorie des periodischen Systems der Elemente**. *Zeitschrift für Physik*, **48**(1-2):73–79, 1928.

[18] P. A. M. Dirac. **Note on exchange phenomena in the Thomas atom**. In *Mathematical Proceedings of the Cambridge Philosophical Society*, **26**, pages 376–385. Cambridge Univ Press, 1930.

[19] P. Hohenberg and W. Kohn. **Inhomogeneous electron gas**. *Physical Review*, **136**(3B):B864, 1964.

[20] M. Levy. **Universal variational functionals of electron densities, first-order density matrices, and natural spin-orbitals and solution of the v-representability problem**. *Proceedings of the National Academy of Sciences*, **76**(12):6062–6065, 1979.

[21] E. H. Lieb. **Density functionals for coulomb systems**. *International Journal of Quantum Chemistry*, **24**:243–277, 1983.

[22] H. Englisch and R. Englisch. **Hohenberg-Kohn theorem and non-V-representable densities**. *Physica A: Statistical Mechanics and its Applications*, **121**(1):253–268, 1983.

[23] W. Kohn and L. J. Sham. **Self-consistent equations including exchange and correlation effects**. *Physical Review*, **140**(4A):A1133, 1965.

[24] J. C. Slater. **A simplification of the Hartree-Fock method**. *Physical Review*, **81**(3):385, 1951.

[25] D. M. Ceperley and B. J. Alder. **Ground State of the Electron Gas by a Stochastic Method**. *Physical Review Letters*, **45**(7):566, 1980.

[26] S. H. Vosko, L. Wilk, and M. Nusair. **Accurate spin-dependent electron liquid correlation energies for local spin density calculations: a critical analysis**. *Canadian Journal of Physics*, **58**(8):1200–1211, 1980.

[27] J. P. Perdew, A. Ruzsinszky, J. Tao, V. N. Staroverov, G. E. Scuseria, and G. I. Csonka. **Prescription for the design and selection of density functional approximations: More constraint satisfaction with fewer fits**. *The Journal of Chemical Physics*, **123**:062201, 2005.

[28] F. Herman, J. P. van Dyke, and I. B. Ortenburger. **Improved statistical exchange approximation for inhomogeneous many-electron systems**. *Physical Review Letters*, **22**(16):807–811, 1969.

[29] M. C. Gibson. *Implementation and Application of Advanced Density Functionals*. PhD thesis, University of Durham, 2006.

[30] J. P. Perdew. **Accurate density functional for the energy: Real-space cutoff of the gradient expansion for the exchange hole**. *Physical Review Letters*, **55**(16):1665, 1985.

[31] D. C. Langreth and M. J. Mehl. **Beyond the local-density approximation in calculations of ground-state electronic properties**. *Physical Review B*, **28**(4):1809, 1983.

[32] J. P. Perdew, K. Burke, and M. Ernzerhof. **Generalized gradient approximation made simple**. *Physical Review Letters*, **77**(18):3865–3868, 1996.

[33] J. P. Perdew and Y. Wang. **Accurate and simple analytic representation of the electron-gas correlation energy**. *Physical Review B*, **45**(23):13244, 1992.

[34] A. D. Becke. **Density-functional exchange-energy approximation with correct asymptotic behavior**. *Physical Review A*, **38**(6):3098, 1988.

[35] B. H. Hammer, L. B. Hansen, and J. K. Nørskov. **Improved adsorption energetics within density-functional theory using revised Perdew-Burke-Ernzerhof functionals**. *Physical Review B*, **59**(11):7413, 1999.

[36] E. I. Proynov, E. Ruiz, A. Vela, and D. R. Salahub. **Determining and extending the domain of exchange and correlation functionals**. *International Journal of Quantum Chemistry*, **56**(S29):61–78, 1995.

[37] A. D. Becke. **A new mixing of Hartree–Fock and local density-functional theories**. *The Journal of Chemical Physics*, **98**:1372, 1993.

[38] C. Lee, W. Yang, and R. G. Parr. **Development of the Colle-Salvetti correlation-energy formula into a functional of the electron density**. *Physical Review B*, **37**(2):785, 1988.

[39] P. E. Blöchl, C. J. Först, and J. Schimpl. **Projector augmented wave method: ab initio molecular dynamics with full wave functions**. *Bulletin of Materials Science*, **26**(1):33–41, 2003.

[40] J. C. Slater and G. F. Koster. **Simplified LCAO method for the periodic potential problem**. *Physical Review*, **94**(6):1498, 1954.

[41] F. Bloch. **Über die quantenmechanik der elektronen in kristallgittern**. *Zeitschrift für Physik*, **52**(7-8):555–600, 1929.

[42] J. C. Slater. **Wave functions in a periodic potential**. *Physical Review*, **51**(10):846, 1937.

[43] O. K. Andersen. **Linear methods in band theory**. *Physical Review B*, **12**(8):3060, 1975.

[44] K. Schwarz, P. Blaha, and G. K. H. Madsen. **Electronic structure calculations of solids using the WIEN2k package for material sciences**. *Computer Physics Communications*, **147**(1):71–76, 2002.

[45] L. Nordstrom and D. J. Singh. *Planewaves, Pseudopotentials, and the LAPW method*. Springer, 2006.

[46] P. Blaha, K. Schwarz, P. Sorantin, and S. B. Trickey. **Full-potential, linearized augmented plane wave programs for crystalline systems**. *Computer Physics Communications*, **59**(2):399–415, 1990.

[47] J. Korringa. **On the calculation of the energy of a Bloch wave in a metal**. *Physica*, **13**(6):392–400, 1947.

[48] W. Kohn and N. Rostoker. **Solution of the Schrödinger equation in periodic lattices with an application to metallic lithium**. *Physical Review*, **94**(5):1111, 1954.

[49] M. C. Payne, M. P. Teter, D. C. Allan, T. A. Arias, and J. D. Joannopoulos. **Iterative minimization techniques for ab initio total-energy calculations: molecular dynamics and conjugate gradients**. *Reviews of Modern Physics*, **64**(4):1045–1097, 1992.

[50] D. R. Hamann, M. Schlüter, and C. Chiang. **Norm-conserving pseudopotentials**. *Physical Review Letters*, **43**(20):1494–1497, 1979.

[51] R. Car and M. Parrinello. **Unified approach for molecular dynamics and density-functional theory**. *Physical Review Letters*, **55**(22):2471, 1985.

[52] S. G. Louie, S. Froyen, and M. L. Cohen. **Nonlinear ionic pseudopotentials in spin-density-functional calculations**. *Physical Review B*, **26**(4):1738, 1982.

[53] D. Vanderbilt. **Soft self-consistent pseudopotentials in a generalized eigenvalue formalism**. *Physical Review B*, **41**(11):7892, 1990.

[54] G. Kresse and D. Joubert. **From ultrasoft pseudopotentials to the projector augmented-wave method**. *Physical Review B*, **59**(3):1758, 1999.

[55] P. E. Blöchl. **Projector augmented-wave method**. *Physical Reviw B*, **50**(24):17953, 1994.

[56] J. Hafner. **Materials simulations using VASP - a quantum perspective to materials science**. *Computer Physics Communications*, **177**(1):6–13, 2007.

[57] G. Kresse and J. Furthmüller. **Efficient iterative schemes for ab initio total-energy calculations using a plane-wave basis set**. *Physical Review B*, **54**(16):11169, 1996.

[58] E. Sjöstedt, L. Nordström, and D.J Singh. **An alternative way of linearizing the augmented plane-wave method**. *Solid state communications*, **114**(1):15–20, 2000.

[59] P. Blaha, K. Schwarz, G. K. H. Madsen, D. Kvasnicka, and J. Luitz. **WIEN2k. Karlheinz Schwarz, Techn. Universitat Wien, Austria (2001)**. Technical report, ISBN 3-9501031-1-2, 2003.

[60] J. Harl and G. Kresse. **Accurate bulk properties from approximate many-body techniques**. *Physical Review Letters*, **103**(5):056401, 2009.

[61] J. Harl, L. Schimka, and G. Kresse. **Assessing the quality of the random phase approximation for lattice constants and atomization energies of solids**. *Physical Review B*, **81**(11):115126, 2010.

[62] L. Schimka, J. Harl, A. Stroppa, A. Grüneis, M. Marsman, F. Mittendorfer, and G. Kresse. **Accurate surface and adsorp-**

tion energies from many-body perturbation theory. *Nature Materials*, **9**(9):741–744, 2010.

[63] S. Lebegue, J. Harl, T. Gould, J. G. Ángyán, G. Kresse, and J. F. Dobson. **Cohesive properties and asymptotics of the dispersion interaction in graphite by the random phase approximation**. *Physical Review Letters*, **105**(19):196401, 2010.

[64] A. Marini, P. García-González, and A. Rubio. **First-principles description of correlation effects in layered materials**. *Physical Review Letters*, **96**(13):136404, 2006.

[65] J. Harl and G. Kresse. **Cohesive energy curves for noble gas solids calculated by adiabatic connection fluctuation-dissipation theory**. *Physical Review B*, **77**(4):045136, 2008.

[66] J. Harl. *The linear response function in density functional theory.* PhD thesis, Universität Wien, 2008.

[67] H. B. Callen and T. A. Welton. **Irreversibility and generalized noise**. *Physical Review*, **83**(1):34–40, 1951.

[68] M. Dion, H. Rydberg, E. Schröder, D. C. Langreth, and B. I. Lundqvist. **Van der Waals density functional for general geometries**. *Physical Review Letters*, **92**(24):246401, 2004.

[69] J. Klimeš, D. R. Bowler, and A. Michaelides. **Van der Waals density functionals applied to solids**. *Physical Review B*, **83**(19):195131, 2011.

[70] K. Lee, É. D. Murray, L. Kong, B. I. Lundqvist, and D. C. Langreth. **Higher-accuracy van der Waals density functional**. *Physical Review B*, **82**(8):081101, 2010.

[71] D. C. Langreth, B. I. Lundqvist, S. D. Chakarova-Käck, V. R. Cooper, M. Dion, P. Hyldgaard, A. Kelkkanen, J. Kleis, L. Kong, S. Li, et al. **A density functional for sparse matter**. *Journal of Physics: Condensed Matter*, **21**(8):084203, 2009.

[72] C. Douketis, G. Scoles, S. Marchetti, M. Zen, and A. J. Thakkar. **Intermolecular forces via hybrid Hartree–Fock–SCF plus damped dispersion (HFD) energy calculations. An improved spherical model**. *The Journal of Chemical Physics*, **76**(6):3057–3063, 1982.

[73] S. Grimme. **Semiempirical GGA-type density functional constructed with a long-range dispersion correction**. *Journal of computational chemistry*, **27**(15):1787–1799, 2006.

[74] A. D. Becke and E. R. Johnson. **Exchange-hole dipole moment and the dispersion interaction**. *The Journal of Chemical Physics*, **122**(15):154104, 2005.

[75] A. D. Becke and E. R. Johnson. **A density-functional model of the dispersion interaction**. *The Journal of Chemical Physics*, **123**(15):154101, 2005.

[76] A. Tkatchenko and M. Scheffler. **Accurate molecular van der Waals interactions from ground-state electron density and free-atom reference data**. *Physical Review Letters*, **102**(7):073005, 2009.

[77] A. Georges. **Strongly Correlated Electron Materials: Dynamical Mean-Field Theory and Electronic Structure**. In *LECTURES ON THE PHYSICS OF HIGHLY CORRELATED ELECTRON SYSTEMS VIII: Eighth Training Course in the Physics of Correlated Electron Systems and High-Tc Superconductors*, **715**, pages 3–74. AIP Publishing, 2004.

[78] G. A. Sawatzky and J. W. Allen. **Magnitude and origin of the band gap in NiO**. *Physical Review Letters*, **53**(24):2339, 1984.

[79] V. I. Anisimov, J. Zaanen, and O. K. Andersen. **Band theory and Mott insulators: Hubbard U instead of Stoner I**. *Physical Review B*, **44**(3):943, 1991.

[80] A. I. Liechtenstein, V. I. Anisimov, and J. Zaanen. **Density-functional theory and strong interactions: Orbital ordering in Mott-Hubbard insulators**. *Physical Review B*, **52**(8):R5467–R5470, 1995.

[81] V. I. Anisimov, F. Aryasetiawan, and A. I. Lichtenstein. **First-principles calculations of the electronic structure and spectra of strongly correlated systems: the LDA+U method**. *Journal of Physics: Condensed Matter*, **9**(4):767, 1997.

[82] L. Hedin. **New method for calculating the one-particle Green's function with application to the electron-gas problem**. *Physical Review*, **139**(3A):A796, 1965.

[83] F. Caruso, D. R. Rohr, M. Hellgren, X. Ren, P. Rinke, A. Rubio, and M. Scheffler. **Bond breaking and bond formation: how electron correlation is captured in many-body perturbation theory and density-functional theory**. *Physical Review Letters*, **110**(14):146403, 2013.

[84] O. Gunnarsson, O. K. Andersen, O. Jepsen, and J. Zaanen. **Density-functional calculation of the parameters in the Anderson model: Application to Mn in CdTe**. *Physical Review B*, **39**(3):1708, 1989.

[85] M. Karolak. *Electronic Correlation Effects in Transition Metal Systems: From Bulk Crystals to Nanostructures*. PhD thesis, Universität Hamburg, 2013.

[86] M. T. Czyżyk and G. A. Sawatzky. **Local-density functional and on-site correlations: the electronic structure of La_2CuO_4 and $LaCuO_3$**. *Physical Review B*, **49**(20):14211, 1994.

[87] A. C. Hewson. *The Kondo problem to heavy fermions*. Number 2. Cambridge university press, 1997.

[88] J. Hubbard. **Electron correlations in narrow energy bands**. *Proceedings of the Royal Society of London. Series A. Mathematical and Physical Sciences*, **276**(1365):238–257, 1963.

[89] M. C. Gutzwiller. **Effect of correlation on the ferromagnetism of transition metals**. *Physical Review Letters*, **10**(5):159, 1963.

[90] J. Kanamori. **Electron correlation and ferromagnetism of transition metals**. *Progress of Theoretical Physics*, **30**(3):275–289, 1963.

[91] A. Georges, G. Kotliar, W. Krauth, and M. J. Rozenberg. **Dynamical mean-field theory of strongly correlated fermion systems and the limit of infinite dimensions**. *Reviews of Modern Physics*, **68**(1):13, 1996.

[92] D. Vollhardt. **Dynamical Mean-Field Theory of Electronic Correlations in Models and Materials**. In *American Institute of Physics Conference Series*, **1297**, pages 339–403, 2010.

[93] P. W. Anderson. **Localized magnetic states in metals**. *Physical Review*, **124**(1):41, 1961.

[94] R. Bulla, T. A. Costi, and T. Pruschke. **Numerical renormalization group method for quantum impurity systems**. *Reviews of Modern Physics*, **80**(2):395, 2008.

[95] M. Caffarel and W. Krauth. **Exact diagonalization approach to correlated fermions in infinite dimensions: Mott transition and superconductivity**. *Physical Review Letters*, **72**(10):1545, 1994.

[96] E. Gull, A. J. Millis, A. I. Lichtenstein, A. N. Rubtsov, M. Troyer, and P. Werner. **Continuous-time Monte Carlo methods for quantum impurity models**. *Reviews of Modern Physics*, **83**(2):349, 2011.

[97] J. E. Hirsch and R. M. Fye. **Monte Carlo method for magnetic impurities in metals**. *Physical Review Letters*, **56**(23):2521–2524, 1986.

[98] K. Held, I. A. Nekrasov, N. Blümer, V. I. Anisimov, and D. Vollhardt. **Realistic modeling of strongly correlated electron systems: An introduction to the LDA+ DMFT approach**. *International Journal of Modern Physics B*, **15**(19n20):2611–2625, 2001.

[99] A. I. Lichtenstein and M. I. Katsnelson. **Ab initio calculations of quasiparticle band structure in correlated systems: LDA++ approach**. *Physical Review B*, **57**(12):6884, 1998.

[100] V. I. Anisimov, A. I. Poteryaev, M. A. Korotin, A. O. Anokhin, and G. Kotliar. **First-principles calculations of the electronic structure and spectra of strongly correlated systems: dynamical**

mean-field theory. *Journal of Physics: Condensed Matter*, **9**(35):7359, 1997.

[101] M. I. Katsnelson. *Graphene: Carbon in Two Dimensions*. Cambridge University Press, 2012.

[102] K. S. Novoselov, V. I. Falko, L. Colombo, P. R. Gellert, M. G. Schwab, K. Kim, et al. **A roadmap for graphene**. *Nature*, **490**(7419):192–200, 2012.

[103] A. H. Castro Neto, F. Guinea, N. M. R. Peres, K. S. Novoselov, and A. K. Geim. **The electronic properties of graphene**. *Reviews of Modern Physics*, **81**(1):109, 2009.

[104] P. R. Wallace. **The band theory of graphite**. *Physical Review*, **71**(9):622, 1947.

[105] J. Jung and A. H. MacDonald. **Tight-binding model for graphene π-bands from maximally localized Wannier functions**. *Physical Review B*, **87**(19):195450, 2013.

[106] A. K. Geim and K. S. Novoselov. **The rise of graphene**. *Nature Materials*, **6**(3):183–191, 2007.

[107] Y. Zhang, Y.-W. Tan, H. L. Stormer, and P. Kim. **Experimental observation of the quantum Hall effect and Berry's phase in graphene**. *Nature*, **438**(7065):201–204, 2005.

[108] K. S. Novoselov, E. McCann, S. V. Morozov, V. I. Falko, M. I. Katsnelson, U. Zeitler, D. Jiang, F. Schedin, and A. K. Geim. **Unconventional quantum Hall effect and Berrys phase of 2π in bilayer graphene**. *Nature Physics*, **2**(3):177–180, 2006.

[109] Mikhail I Katsnelson. **Graphene: carbon in two dimensions**. *Materials today*, **10**(1):20–27, 2007.

[110] E. V. Gorbar, V. P. Gusynin, V. A. Miransky, and I. A. Shovkovy. **Magnetic field driven metal-insulator phase transition in planar systems**. *Physical Review B*, **66**(4):045108, 2002.

[111] V. P. Gusynin and S. G. Sharapov. **Unconventional integer quantum Hall effect in graphene**. *Physical Review Letters*, **95**(14):146801, 2005.

[112] K. S. Novoselov, Z. Jiang, Y. Zhang, S. V. Morozov, H. L. Stormer, U. Zeitler, J. C. Maan, G. S. Boebinger, P. Kim, and A. K. Geim. **Room-temperature quantum Hall effect in graphene**. *Science*, **315**(5817):1379–1379, 2007.

[113] M. I. Katsnelson, K. S. Novoselov, and A. K. Geim. **Chiral tunnelling and the Klein paradox in graphene**. *Nature Physics*, **2**(9):620–625, 2006.

[114] S. V. Morozov, K. S. Novoselov, M. I. Katsnelson, F. Schedin, D. C. Elias, J. A. Jaszczak, and A. K. Geim. **Giant intrinsic carrier mobilities in graphene and its bilayer**. *Physical Review Letters*, **100**(1):016602, 2008.

[115] N. Stander, B. Huard, and D. Goldhaber-Gordon. **Evidence for Klein tunneling in graphene pn junctions**. *Physical Review Letters*, **102**(2):026807, 2009.

[116] A. F. Young and P. Kim. **Quantum interference and Klein tunnelling in graphene heterojunctions**. *Nature Physics*, **5**(3):222–226, 2009.

[117] T. Tudorovskiy, K. J. A. Reijnders, and M. I. Katsnelson. **Chiral tunneling in single-layer and bilayer graphene**. *Physica Scripta*, **2012**(T146):014010, 2012.

[118] X. Blase, A. Rubio, S. G. Louie, and M. L. Cohen. **Quasiparticle band structure of bulk hexagonal boron nitride and related systems**. *Physical Review B*, **51**(11):6868, 1995.

[119] B. Sachs, T. O. Wehling, M. I. Katsnelson, and A. I. Lichtenstein. **Adhesion and electronic structure of graphene on hexagonal boron nitride substrates**. *Physical Review B*, **84**(19):195414, 2011.

[120] K. Watanabe, T. Taniguchi, and H. Kanda. **Direct-bandgap properties and evidence for ultraviolet lasing of hexagonal boron nitride single crystal**. *Nature Materials*, **3**(6):404–409, 2004.

[121] C. R. Dean, A. F. Young, I. Meric, C. Lee, L. Wang, S. Sorgenfrei, K. Watanabe, T. Taniguchi, P. Kim, K. L. Shepard, and J. Hone. **Boron nitride substrates for high-quality graphene electronics**. *Nature Nanotechnology*, **5**(10):722–726, 2010.

[122] I. Meric, C. Dean, A. Young, J. Hone, P. Kim, and K. L. Shepard. **Graphene field-effect transistors based on boron nitride gate dielectrics**. In *Electron Devices Meeting (IEDM), 2010 IEEE International*, pages 23–2. IEEE, 2010.

[123] R. Decker, Y. Wang, V. W. Brar, W. Regan, H.-Z. Tsai, Q. Wu, W. Gannett, A. Zettl, and M. F. Crommie. **Local electronic properties of graphene on a BN substrate via scanning tunneling microscopy**. *Nano Letters*, **11**(6):2291–2295, 2011.

[124] Q. H. Wang, K. Kalantar-Zadeh, A. Kis, J. N. Coleman, and M. S. Strano. **Electronics and optoelectronics of two-dimensional transition metal dichalcogenides**. *Nature Nanotechnology*, **7**(11):699–712, 2012.

[125] M. Xu, T. Liang, M. Shi, and H. Chen. **Graphene-Like Two-Dimensional Materials**. *Chemical Reviews*, **113**(5):3766–3798, 2013.

[126] Z. Y. Zhu, Y. C. Cheng, and U. Schwingenschlögl. **Giant spin-orbit-induced spin splitting in two-dimensional transition-metal dichalcogenide semiconductors**. *Physical Review B*, **84**(15):153402, 2011.

[127] K. F. Mak, C. Lee, J. Hone, J. Shan, and T. F. Heinz. **Atomically Thin MoS_2: A New Direct-Gap Semiconductor**. *Physical Review Letters*, **105**(13):136805, 2010.

[128] A. Kuc, N. Zibouche, and T. Heine. **Influence of quantum confinement on the electronic structure of the transition metal sulfide TS_ {2}**. *Physical Review B*, **83**(24):245213, 2011.

[129] K. S. Novoselov, D. Jiang, F. Schedin, T. J. Booth, V. V. Khotkevich, S. V. Morozov, and A. K. Geim. **Two-dimensional atomic crystals**. *PNAS*, **102**(30):10451–10453, 2005.

[130] B. Radisavljevic, A. Radenovic, J. Brivio, V. Giacometti, and A. Kis. **Single-layer MoS2 transistors**. *Nature Nanotechnology*, **6**(3):147–150, 2011.

[131] H. Zeng, J. Dai, W. Yao, D. Xiao, and X. Cui. **Valley polarization in MoS2 monolayers by optical pumping**. *Nature Nanotechnology*, **7**(8):490–493, 2012.

[132] K. F. Mak, K. He, J. Shan, and T. F. Heinz. **Control of valley polarization in monolayer MoS2 by optical helicity**. *Nature Nanotechnology*, **7**(8):494–498, 2012.

[133] T. Cao, G. Wang, W. Han, H. Ye, C. Zhu, J. Shi, Q. Niu, P. Tan, E. Wang, B. Liu, et al. **Valley-selective circular dichroism of monolayer molybdenum disulphide**. *Nature Communications*, **3**:887, 2012.

[134] J. Isberg, M. Gabrysch, J. Hammersberg, S. Majdi, K. K. Kovi, and D. J. Twitchen. **Generation, transport and detection of valley-polarized electrons in diamond**. *Nature Materials*, **12**(8):760–764, 2013.

[135] D. C. Elias, R. R. Nair, T. M. G. Mohiuddin, S. V. Morozov, P. Blake, M. P. Halsall, A. C. Ferrari, D. W. Boukhvalov, M. I. Katsnelson, A. K. Geim, et al. **Control of graphene's properties by reversible hydrogenation: evidence for graphane**. *Science*, **323**(5914):610–613, 2009.

[136] K. Xu, P. Cao, and J. R. Heath. **Graphene visualizes the first water adlayers on mica at ambient conditions**. *Science*, **329**(5996):1188–1191, 2010.

[137] K. S. Novoselov and A. H. Castro Neto. **Two-dimensional crystals-based heterostructures: materials with tailored properties**. *Physica Scripta*, **2012**(T146):014006, 2012.

[138] J. Xue, J. Sanchez-Yamagishi, D. Bulmash, P. Jacquod, A. Deshpande, K. Watanabe, T. Taniguchi, P. Jarillo-Herrero, and B. J. LeRoy. **Scanning tunnelling microscopy and spectroscopy of ultra-flat graphene on hexagonal boron nitride**. *Nature Materials*, **10**(4):282–285, 2011.

[139] D. C. Elias, R. V. Gorbachev, A. S. Mayorov, S. V. Morozov, A. A. Zhukov, P. Blake, L. A. Ponomarenko, I. V. Grigorieva, K. S. Novoselov, F. Guinea, et al. **Dirac cones reshaped by interaction effects in suspended graphene**. *Nature Physics*, **7**(9):701–704, 2011.

[140] A. S. Mayorov, R. V. Gorbachev, S. V. Morozov, L. Britnell, R. Jalil, L. A. Ponomarenko, P. Blake, K. S. Novoselov, K. Watanabe, T. Taniguchi, et al. **Micrometer-scale ballistic transport in encapsulated graphene at room temperature**. *Nano Letters*, **11**(6):2396–2399, 2011.

[141] L. A. Ponomarenko, A. K. Geim, A. A. Zhukov, R. Jalil, S. V. Morozov, I. V. Grigorieva, K. S. Novoselov, E. H. Hill, V. V. Cheianov, V. I. Falko, K. Watanabe, T. Taniguchi, and R. V. Gorbachev. **Tunable metal-insulator transition in double-layer graphene heterostructures**. *Nature Physics*, **7**(12):958–961, 2011.

[142] S. J. Haigh, A. Gholinia, R. Jalil, S. Romani, L. Britnell, D. C. Elias, K. S. Novoselov, L. A. Ponomarenko, A. K. Geim, and R. Gorbachev. **Cross-sectional imaging of individual layers and buried interfaces of graphene-based heterostructures and superlattices**. *Nature Materials*, **11**(9):764–767, 2012.

[143] T. Georgiou, R. Jalil, B. D. Belle, L. Britnell, R. V. Gorbachev, S. V. Morozov, Y.-J. Kim, A. Gholinia, S. J. Haigh, O. Makarovsky, et al. **Vertical field-effect transistor based on graphene-WS2 heterostructures for flexible and transparent electronics**. *Nature Nanotechnology*, **8**(2):100–103, 2012.

[144] A. K. Geim. **Graphene: status and prospects**. *Science*, **324**(5934):1530–1534, 2009.

[145] B. Sachs, L. Britnell, T. O. Wehling, A. Eckmann, R. Jalil, B. D. Belle, A. I. Lichtenstein, M. I. Katsnelson, and K. S. Novoselov. **Doping mechanisms in graphene-MoS2 hybrids**. *Applied Physics Letters*, **103**(25):251607, 2013.

[146] W. Zhang, C.-P. Chuu, J.-K. Huang, C.-H. Chen, M.-L. Tsai, Y.-H. Chang, C.-T. Liang, Y.-Z. Chen, Y.-L. Chueh, J.-H. He, et al. **Ultrahigh-Gain Photodetectors Based on Atomically Thin Graphene-MoS2 Heterostructures**. *Scientific reports*, **4**(3826), 2014.

[147] R. V. Gorbachev, A. K. Geim, M. I. Katsnelson, K. S. Novoselov, T. Tudorovskiy, I. V. Grigorieva, A. H. MacDonald, S. V. Morozov, K. Watanabe, T. Taniguchi, et al. **Strong Coulomb drag and broken symmetry in double-layer graphene**. *Nature physics*, **8**(12):896–901, 2012.

[148] L. A. Ponomarenko, R. V. Gorbachev, G. L. Yu, D. C. Elias, R. Jalil, A. A. Patel, A. Mishchenko, A. S. Mayorov, C. R. Woods, J. R. Wallbank, et al. **Cloning of Dirac fermions in graphene superlattices**. *Nature*, **497**(7451):594–597, 2013.

[149] C. R. Dean, L. Wang, P. Maher, C. Forsythe, F. Ghahari, Y. Gao, J. Katoch, M. Ishigami, P. Moon, M. Koshino, et al. **Hofstadter's butterfly and the fractal quantum Hall effect in moire superlattices**. *Nature*, **497**(7451):598–602, 2013.

[150] B. Hunt, J. D. Sanchez-Yamagishi, A. F. Young, M. Yankowitz, B. J. LeRoy, K. Watanabe, T. Taniguchi, P. Moon, M. Koshino, P. Jarillo-Herrero, et al. **Massive Dirac fermions and Hofstadter butterfly in a van der Waals heterostructure**. *Science*, **340**(6139):1427–1430, 2013.

[151] G. Giovannetti, P. A. Khomyakov, G. Brocks, P. J. Kelly, and J. van den Brink. **Substrate-induced band gap in graphene on hexagonal boron nitride: Ab initio density functional calculations**. *Physical Review B*, **76**(7):073103, 2007.

[152] G. Constantinescu, A. Kuc, and T. Heine. **Stacking in Bulk and Bilayer Hexagonal Boron Nitride**. *Physical Review Letters*, **111**(3):036104, 2013.

[153] J. F. Dobson, A. White, and A. Rubio. **Asymptotics of the dispersion interaction: analytic benchmarks for van der Waals energy functionals**. *Physical Review Letters*, **96**(7):073201, 2006.

[154] J. P. Perdew, K. Burke, and Y. Wang. **Generalized gradient approximation for the exchange-correlation hole of a many-electron system**. *Physical Review B*, **54**(23):16533, 1996.

[155] T. Olsen, J. Yan, J. J. Mortensen, and K. S. Thygesen. **Dispersive and covalent interactions between graphene and metal surfaces from the random phase approximation**. *Physical Review Letters*, **107**(15):156401, 2011.

[156] M. Hasegawa and K. Nishidate. **Semiempirical approach to the energetics of interlayer binding in graphite**. *Physical Review B*, **70**(20):205431, 2004.

[157] M. Yankowitz, J. Xue, D. Cormode, J. D. Sanchez-Yamagishi, K. Watanabe, T. Taniguchi, P. Jarillo-Herrero, P. Jacquod, and B. J. LeRoy. **Emergence of superlattice Dirac points in graphene on hexagonal boron nitride**. *Nature Physics*, **8**(5):382–386, 2012.

[158] C. Lee, X. Wei, J. W. Kysar, and J. Hone. **Measurement of the elastic properties and intrinsic strength of monolayer graphene**. *Science*, **321**(5887):385, 2008.

[159] C. Gómez-Navarro, M. Burghard, and K. Kern. **Elastic properties of chemically derived single graphene sheets**. *Nano Letters*, **8**(7):2045–2049, 2008.

[160] S. Bera, A. Arnold, F. Evers, R. Narayanan, and P. Wölfle. **Elastic properties of graphene flakes: boundary effects and lattice vibrations**. *Physical Review B*, **82**(19):195445, 2010.

[161] L. D. Landau and E. M. Lifshitz. **Elasticity theory**. 1975.

[162] P. M. Chaikin and T. C. Lubensky. *Principles of condensed matter physics, p.338*. Cambridge Univ Press, 2000.

[163] K. V. Zakharchenko, M. I. Katsnelson, and A. Fasolino. **Finite temperature lattice properties of graphene beyond the quasiharmonic approximation**. *Physical Review Letters*, **102**(4):046808, 2009.

[164] G. Kresse and J. Hafner. **Norm-conserving and ultrasoft pseudopotentials for first-row and transition elements**. *Journal of Physics: Condensed Matter*, **6**(40):8245, 1994.

[165] K. N. Kudin, G. E. Scuseria, and B. I. Yakobson. **C_2 F, BN, and C nanoshell elasticity from ab initio computations**. *Physical Review B*, **64**(23):235406, 2001.

[166] C. R. Woods, L. Britnell, A. Eckmann, G. L. Yu, R. V. Gorbachev, A. V. Kretinin, J. Park, L. A. Ponomarenko, M. I. Katsnelson, Y. N. Gornostyrev, et al. **Commensurate-incommensurate transition for graphene on hexagonal boron nitride**. *arXiv preprint arXiv:1401.2637*, 2014.

[167] J. Sławińska, I. Zasada, and Z. Klusek. **Energy gap tuning in graphene on hexagonal boron nitride bilayer system**. *Physical Review B*, **81**(15):155433, 2010.

[168] G. Trambly De Laissardière, D. Mayou, and L. Magaud. **Localization of Dirac Electrons in Rotated Graphene Bilayers**. *Nano Letters*, **10**(3):804–808, 2010.

[169] I. Pletikosić, M. Kralj, P. Pervan, R. Brako, J. Coraux, A. T. N'diaye, C. Busse, and T. Michely. **Dirac cones and minigaps for graphene on Ir (111).** *Physical Review Letters*, **102**(5):056808–056808, 2009.

[170] T. Michely, J. Fujii, and I. Vobornik. **Graphene on Ir (111) characterized by angle-resolved photoemission**. *Physical Review B*, **84**(7):075427, 2011.

[171] B. Büttner, C. X. Liu, G. Tkachov, E. G. Novik, C. Brüne, H. Buhmann, E. M. Hankiewicz, P. Recher, B. Trauzettel, S. C.

Zhang, and L. W. Molenkamp. **Single valley Dirac fermions in zero-gap HgTe quantum wells**. *Nature Physics*, **7**(5):418–422, 2011.

[172] P. J. Zomer, S. P. Dash, N. Tombros, and B. J. van Wees. **A transfer technique for high mobility graphene devices on commercially available hexagonal boron nitride**. *Applied Physics Letters*, **99**(23):232104–232104, 2011.

[173] J. C. W. Song, A. V. Shytov, and L. S. Levitov. **Electron Interactions and Gap Opening in Graphene Superlattices**. *Physical Review Letters*, **111**(26):266801, 2013.

[174] C. Lee, X. Wei, Q. Li, R. Carpick, J. W. Kysar, and J. Hone. **Elastic and frictional properties of graphene**. *physica status solidi (b)*, **246**(11-12):2562–2567, 2009.

[175] J.-U. Lee, D. Yoon, and H. Cheong. **Estimation of Young's modulus of graphene by Raman spectroscopy**. *Nano Letters*, **12**(9):4444–4448, 2012.

[176] K. H. Michel and B. Verberck. **Theory of the elastic constants of graphite and graphene**. *physica status solidi (b)*, **245**(10):2177–2180, 2008.

[177] S. B. Petersen, G. P. Gajula, and M. T. Neves-Petersen. **Subpicometer structural information of graphene hidden in a 50pm resolved image**. *Nanoscale*, **5**(19):8874–8878, 2013.

[178] T. O. Wehling, A. V. Balatsky, M. I. Katsnelson, A. I. Lichtenstein, K. Scharnberg, and R. Wiesendanger. **Local electronic signatures of impurity states in graphene**. *Physical Review B*, **75**(12):125425, 2007.

[179] T. O. Wehling, K. S. Novoselov, S. V. Morozov, E. E. Vdovin, M. I. Katsnelson, A. K. Geim, and A. I. Lichtenstein. **Molecular doping of graphene**. *Nano Letters*, **8**(1):173–177, 2008.

[180] T. O. Wehling, S. Yuan, A. I. Lichtenstein, A. K. Geim, and M. I. Katsnelson. **Resonant scattering by realistic impurities in graphene**. *Physical Review Letters*, **105**(5):056802, 2010.

[181] T. O. Wehling, A. I. Lichtenstein, and M. I. Katsnelson. **Transition-metal adatoms on graphene: Influence of local Coulomb interactions on chemical bonding and magnetic moments**. *Physical Review B*, **84**(23):235110, 2011.

[182] B. Sachs, T. O. Wehling, A. I. Lichtenstein, and M. I. Katsnelson. **Theory of Doping: Monovalent Adsorbates**. *Physics and Applications of Graphene-Theory*, pages 29–44.

[183] L. Ju, J. Velasco Jr, E. Huang, S. Kahn, C. Nosiglia, H.-Z. Tsai, W. Yang, T. Taniguchi, K. Watanabe, Y. Zhang, et al. **Photoinduced doping in heterostructures of graphene and boron nitride**. *Nature Nanotechnology*, **9**(5):348–352, 2014.

[184] Sohee Park, Changwon Park, and Gunn Kim. **Interlayer coupling enhancement in graphene/hexagonal boron nitride heterostructures by intercalated defects or vacancies**. *The Journal of chemical physics*, **140**(13):134706, 2014.

[185] M. I. Katsnelson. *private communication*, 2013.

[186] O. Jepsen and O. K. Andersen. **Calculated electronic structure of the sandwich d^1 metals LaI_2 and CeI_2: Application of new LMTO techniques**. *Zeitschrift für Physik B Condensed Matter*, **97**(1):35–47, 1995.

[187] T. O. Wehling, A. I. Lichtenstein, and M. I. Katsnelson. **First-principles studies of water adsorption on graphene: The role of the substrate**. *Applied Physics Letters*, **93**(20):202110, 2008.

[188] M. Bokdam, P. A. Khomyakov, G. Brocks, Z. Zhong, and P. J. Kelly. **Electrostatic doping of graphene through ultrathin hexagonal boron nitride films**. *Nano Letters*, **11**(11):4631–4635, 2011.

[189] S. Bertolazzi, D. Krasnozhon, and A. Kis. **Nonvolatile Memory Cells Based on MoS2/Graphene Heterostructures**. *ACS Nano*, **7**(4):3246–3252, 2013.

[190] M. S. Choi, G.-H. Lee, Y.-J. Yu, D.-Y. Lee, S. H. Lee, P. Kim, J. Hone, and W. J. Yoo. **Controlled charge trapping by molybde-**

num disulphide and graphene in ultrathin heterostructured memory devices. *Nature Communications*, **4**:1624, 2013.

[191] Y. Ma, Y. Dai, M. Guo, C. Niu, and B. Huang. **Graphene adhesion on MoS2 monolayer: An ab initio study**. *Nanoscale*, **3**(9):3883–3887, 2011.

[192] J. Ristein, S. Mammadov, and T. Seyller. **Origin of Doping in Quasi-Free-Standing Graphene on Silicon Carbide**. *Physical Review Letters*, **108**(24):246104, 2012.

[193] S. Kim, J. Ihm, H. J. Choi, and Y.-W. Son. **Origin of anomalous electronic structures of epitaxial graphene on silicon carbide**. *Physical Review Letters*, **100**(17):176802, 2008.

[194] J. M. Stellman. *Encyclopaedia of occupational health and safety.* Intl Labour Organisation, 1998.

[195] N. N. Greenwood and A. Earnshaw. *Chemistry of the Elements (2nd ed.).* Butterworth-Heinemann, 1997.

[196] M. V. Bollinger, J. V. Lauritsen, K. W. Jacobsen, J. K. Nørskov, S. Helveg, and F. Besenbacher. **One-Dimensional Metallic Edge States in** MoS_2. *Physical Review Letters*, **87**(19):196803, 2001.

[197] M. V. Bollinger, K. W. Jacobsen, and J. K. Nørskov. **Atomic and electronic structure of** MoS_2 **nanoparticles**. *Physical Review B*, **67**(8):085410, 2003.

[198] P. A. Khomyakov, A. A. Starikov, G. Brocks, and P. J. Kelly. **Nonlinear screening of charges induced in graphene by metal contacts**. *Physical Review B*, **82**(11):115437, 2010.

[199] J. Park, Y. H. Ahn, and C. Ruiz-Vargas. **Imaging of photocurrent generation and collection in single-layer graphene**. *Nano Letters*, **9**(5):1742–1746, 2009.

[200] F. Xia, T. Mueller, R. Golizadeh-Mojarad, M. Freitag, Y. Lin, J. Tsang, V. Perebeinos, and P. Avouris. **Photocurrent imaging**

and efficient photon detection in a graphene transistor. *Nano Letters*, **9**(3):1039–1044, 2009.

[201] T. J. Echtermeyer, L. Britnell, P. K. Jasnos, A. Lombardo, R. V. Gorbachev, A. N. Grigorenko, A. K. Geim, A. C. Ferrari, and K. S. Novoselov. **Strong plasmonic enhancement of photovoltage in graphene**. *Nature Communications*, **2**(1464):458–462, 2011.

[202] E. J. H. Lee, K. Balasubramanian, R. T. Weitz, M. Burghard, and K. Kern. **Contact and edge effects in graphene devices**. *Nature Nanotechnology*, **3**(8):486–490, 2008.

[203] N. M. Gabor, J. C. W. Song, Q. Ma, N. L. Nair, T. Taychatanapat, K. Watanabe, T. Taniguchi, L. S. Levitov, and P. Jarillo-Herrero. **Hot carrier-assisted intrinsic photoresponse in graphene**. *Science*, **334**(6056):648–652, 2011.

[204] X. Xu, N. M. Gabor, J. S. Alden, A. M. van der Zande, and P. L. McEuen. **Photo-thermoelectric effect at a graphene interface junction**. *Nano Letters*, **10**(2):562–566, 2009.

[205] M. Buscema, M. Barkelid, V. Zwiller, H. S. J. van der Zant, G. A. Steele, and A. Castellanos-Gomez. **Large and Tunable Photothermoelectric Effect in Single-Layer MoS2**. *Nano Letters*, **13**(2):358–363, 2013.

[206] J. Xia, F. Chen, J. Li, and N. Tao. **Measurement of the quantum capacitance of graphene**. *Nature Nanotechnology*, **4**(8):505–509, 2009.

[207] L. V. Dzemiantsova, M. Karolak, F. Lofink, A. Kubetzka, B. Sachs, K. von Bergmann, S. Hankemeier, T. O. Wehling, R. Frömter, H. P. Oepen, et al. **Multiscale magnetic study of Ni (111) and graphene on Ni (111)**. *Physical Review B*, **84**(20):205431, 2011.

[208] S. J. Altenburg, J. Kröger, T. O. Wehling, B. Sachs, A. I. Lichtenstein, and R. Berndt. **Local Gating of an Ir (111) Surface Resonance by Graphene Islands**. *Physical Review Letters*, **108**(20):206805, 2012.

[209] M. Eizenberg and J. M. Blakely. **Carbon monolayer phase condensation on Ni (111)**. *Surface Science*, **82**(1):228–236, 1979.

[210] C. Mattevi, H. Kim, and M. Chhowalla. **A review of chemical vapour deposition of graphene on copper**. *Journal of Materials Chemistry*, **21**(10):3324–3334, 2011.

[211] T. A. Land, T. Michely, R. J. Behm, J. C. Hemminger, and G. Comsa. **STM investigation of single layer graphite structures produced on Pt (111) by hydrocarbon decomposition**. *Surface Science*, **264**(3):261–270, 1992.

[212] S. Marchini, S. Günther, and J. Wintterlin. **Scanning tunneling microscopy of graphene on Ru (0001)**. *Physical Review B*, **76**(7):075429, 2007.

[213] M. Sicot, P. Leicht, A. Zusan, S. Bouvron, O. Zander, M. Weser, Y. S. Dedkov, K. Horn, and M. Fonin. **Size-selected epitaxial nanoislands underneath graphene Moiré on Rh (111)**. *ACS Nano*, **6**(1):151–158, 2012.

[214] J. Coraux, M. Engler, C. Busse, D. Wall, N. Buckanie, F.-J. Meyer zu Heringdorf, R. van Gastel, B. Poelsema, T. Michely, et al. **Growth of graphene on Ir (111)**. *New Journal of Physics*, **11**(2):023006, 2009.

[215] J. Wintterlin and M.-L. Bocquet. **Graphene on metal surfaces**. *Surface Science*, **603**(10):1841–1852, 2009.

[216] E. Y. Andrei, G. Li, and X. Du. **Electronic properties of graphene: a perspective from scanning tunneling microscopy and magnetotransport**. *Reports on Progress in Physics*, **75**(5):056501, 2012.

[217] P. A. Khomyakov, G. Giovannetti, P. C. Rusu, G. Brocks, J. van den Brink, and P. J. Kelly. **First-principles study of the interaction and charge transfer between graphene and metals**. *Physical Review B*, **79**(19):195425, 2009.

[218] E. N. Voloshina, E. Fertitta, A. Garhofer, F. Mittendorfer, M. Fonin, A. Thissen, and Y. S. Dedkov. **Electronic structure and**

imaging contrast of graphene moire on metals. *Scientific Reports*, **3**(1072), 2013.

[219] J. Bardeen. **Tunnelling from a Many-Particle Point of View**. *Physical Review Letters*, **6**(2):57, 1961.

[220] J. Tersoff and D. R. Hamann. **Theory and Application for the Scanning Tunneling Microscope**. *Physical Review Letters*, **50**(25):1998–2001, 1983.

[221] J. Tersoff and D. R. Hamann. **Theory of the scanning tunneling microscope**. *Physical Review B*, **31**(2):805–813, 1985.

[222] I. Pletikosić, M. Kralj, D. Šokčević, R. Brako, P. Lazić, and P. Pervan. **Photoemission and density functional theory study of Ir (111); energy band gap mapping**. *Journal of Physics: Condensed Matter*, **22**(13):135006, 2010.

[223] J. Coraux, T. N. Plasa, C. Busse, T. Michely, et al. **Structure of epitaxial graphene on Ir (111)**. *New Journal of Physics*, **10**(4):043033, 2008.

[224] E. Starodub, A. Bostwick, L. Moreschini, S. Nie, F. El Gabaly, K. F. McCarty, and E. Rotenberg. **In-plane orientation effects on the electronic structure, stability, and Raman scattering of monolayer graphene on Ir (111)**. *Physical Review B*, **83**(12):125428, 2011.

[225] C. Busse, P. Lazić, R. Djemour, J. Coraux, T. Gerber, N. Atodiresei, V. Caciuc, R.n Brako, S. Blügel, J. Zegenhagen, et al. **Graphene on Ir (111): physisorption with chemical modulation**. *Physical Review Letters*, **107**(3):036101, 2011.

[226] M. Kralj, I. Pletikosić, M. Petrović, P. Pervan, M. Milun, C. Busse, T. Michely, J. Fujii, I. Vobornik, et al. **Graphene on Ir (111) characterized by angle-resolved photoemission**. *Physical Review B*, **84**(7):075427, 2011.

[227] O. Hod. **Graphite and hexagonal boron-nitride have the same interlayer distance. Why?** *Journal of Chemical Theory and Computation*, **8**(4):1360–1369, 2012.

[228] T. O. Wehling. *Impurities and Inhomogeneities in Nanoelectronic Systems*. PhD thesis, Universität Hamburg, 2009.

[229] S. K. Hämäläinen, Z. Sun, M. P. Boneschanscher, A. Uppstu, M. Ijäs, A. Harju, D. Vanmaekelbergh, and P. Liljeroth. **Quantum-confined electronic states in atomically well-defined graphene nanostructures**. *Physical Review Letters*, **107**(23):236803, 2011.

[230] S. J. Phark, J. Borme, A. L. Vanegas, M. Corbetta, D. Sander, and J. Kirschner. **Direct Observation of Electron Confinement in Epitaxial Graphene Nanoislands**. *ACS Nano*, **5**(10):8162–8166, 2011.

[231] D. Subramaniam, F. Libisch, Y. Li, C. Pauly, V. Geringer, R. Reiter, T. Mashoff, M. Liebmann, J. Burgdörfer, C. Busse, et al. **Wave-function mapping of graphene quantum dots with soft confinement**. *Physical Review Letters*, **108**(4):046801, 2012.

[232] A. Varykhalov, D. Marchenko, M. R. Scholz, E. D. L. Rienks, T. K. Kim, G. Bihlmayer, J. Sánchez-Barriga, and O. Rader. **Ir (111) surface state with giant Rashba splitting persists under graphene in air**. *Physical Review Letters*, **108**(6):066804, 2012.

[233] R. Rosei, M. De Crescenzi, F. Sette, C. Quaresima, A. Savoia, and P. Perfetti. **Structure of graphitic carbon on Ni (111): A surface extended-energy-loss fine-structure study**. *Physical Review B*, **28**(2):1161, 1983.

[234] C. Klink, I. Stensgaard, F. Besenbacher, and E. Lægsgaard. **An STM study of carbon-induced structures on Ni (111): evidence for a carbidic-phase clock reconstruction**. *Surface Science*, **342**(1):250–260, 1995.

[235] Yi Zhang, Luyao Zhang, and Chongwu Zhou. **Review of chemical vapor deposition of graphene and related applications**. *Accounts of chemical research*, **46**(10):2329–2339, 2013.

[236] A. N. Obraztsov. **Chemical vapour deposition: making graphene on a large scale**. *Nature Nanotechnology*, **4**(4):212–213, 2009.

[237] S. Grandthyll, S. Gsell, M. Weinl, M. Schreck, S. Hüfner, and F. Müller. **Epitaxial growth of graphene on transition metal surfaces: chemical vapor deposition versus liquid phase deposition**. *Journal of Physics: Condensed Matter*, **24**(31):314204, 2012.

[238] G. Bertoni, L. Calmels, A. Altibelli, and V. Serin. **First-principles calculation of the electronic structure and EELS spectra at the graphene/Ni (111) interface**. *Physical Review B*, **71**(7):075402, 2005.

[239] Y. Gamo, A. Nagashima, M. Wakabayashi, M. Terai, and C. Oshima. **Atomic structure of monolayer graphite formed on Ni (111)**. *Surface Science*, **374**(1):61–64, 1997.

[240] M. Fuentes-Cabrera, M. I Baskes, A. V. Melechko, and M. L. Simpson. **Bridge structure for the graphene/Ni (111) system: A first principles study**. *Physical Review B*, **77**(3):035405, 2008.

[241] S. M. Kozlov, F. Viñes, and A. Görling. **Bonding mechanisms of graphene on metal surfaces**. *The Journal of Physical Chemistry C*, **116**(13):7360–7366, 2012.

[242] W. Zhao, S. M. Kozlov, O. Höfert, K. Gotterbarm, M. P. A. Lorenz, F. Viñes, C. Papp, A. Görling, and H.-P. Steinrück. **Graphene on Ni (111): Coexistence of different surface structures**. *The Journal of Physical Chemistry Letters*, **2**(7):759–764, 2011.

[243] C. S. Wang and J. Callaway. **Band structure of nickel: Spin-orbit coupling, the Fermi surface, and the optical conductivity**. *Physical Review B*, **9**(11):4897, 1974.

[244] I. Yang, S. Y. Savrasov, and G. Kotliar. **Importance of correlation effects on magnetic anisotropy in Fe and Ni**. *Physical Review Letters*, **87**(21):216405, 2001.

[245] J. Braun and M. Donath. **Contest between surface resonances and surface states at 3d ferromagnets**. *EPL (Europhysics Letters)*, **59**(4):592, 2002.

[246] K. Doll. **Density functional study of Ni bulk, surfaces and the adsorbate systems Ni (111)(3× 3) R30–Cl, and Ni (111)(2× 2)–K**. *Surface science*, **544**(1):103–120, 2003.

[247] L. Magaud, A. Pasturel, P. Mallet, S. Pons, and J.-Y. Veuillen. **Spin-polarized Shockley state at Ni (111) free surface and at Ni-Cu–based structures on Cu (111) surface**. *EPL (Europhysics Letters)*, **67**(1):90, 2004.

[248] T. Ohwaki, D. Wortmann, H. Ishida, S. Blügel, and K. Terakura. **Spin-polarized field emission from Ni (001) and Ni (111) surfaces**. *Physical Review B*, **73**(23):235424, 2006.

[249] M. Weser, E. N. Voloshina, K. Horn, and Y. S. Dedkov. **Electronic structure and magnetic properties of the graphene/Fe/Ni (111) intercalation-like system**. *Physical Chemistry Chemical Physics*, **13**(16):7534–7539, 2011.

[250] D. Tománek, S. G. Louie, H. J. Mamin, D. W. Abraham, R. E. Thomson, E. Ganz, and J. Clarke. **Theory and observation of highly asymmetric atomic structure in scanning-tunneling-microscopy images of graphite**. *Physical Review B*, **35**(14):7790, 1987.

[251] C. Cao, M. Wu, J. Jiang, and H.-P. Cheng. **Transition metal adatom and dimer adsorbed on graphene: Induced magnetization and electronic structures**. *Physical Review B*, **81**(20):205424, 2010.

[252] M. Gyamfi, T. Eelbo, M. Waśniowska, T. O. Wehling, S. Forti, U. Starke, A. I. Lichtenstein, M. I. Katsnelson, and R. Wiesendanger. **Orbital selective coupling between Ni adatoms and graphene Dirac electrons**. *Physical Review B*, **85**(16):161406, 2012.

[253] T. Eelbo, M. Waśniowska, P. Thakur, M. Gyamfi, B. Sachs, T. O. Wehling, S. Forti, U. Starke, C. Tieg, A. I. Lichtenstein, et al. **Adatoms and clusters of 3d transition metals on**

graphene: Electronic and magnetic configurations. *Physical Review Letters*, **110**(13):136804, 2013.

[254] J. J. Rehr and R. C. Albers. **Theoretical approaches to x-ray absorption fine structure**. *Reviews of Modern Physics*, **72**(3):621, 2000.

[255] R. D. Leapman and L. A. Grunes. **Anomalous L_3/L_2 White-Line Ratios in the 3d Transition Metals**. *Physical Review Letters*, **45**(5):397, 1980.

[256] M. Martins, K. Godehusen, T. Richter, P. Wernet, and P. Zimmermann. **Open shells and multi-electron interactions: core level photoionization of the 3d metal atoms**. *Journal of Physics B: Atomic, Molecular and Optical Physics*, **39**(5):R79, 2006.

[257] H. Ebert and G. Schütz. *Spin-Orbit-Influenced Spectroscopies of Magnetic Solids*. Springer Verlag, 1996.

[258] T. O Wehling, A. V. Balatsky, M. I. Katsnelson, A. I. Lichtenstein, and A. Rosch. **Orbitally controlled Kondo effect of Co adatoms on graphene**. *Physical Review B*, **81**(11):115427, 2010.

[259] M. Karolak, T. O. Wehling, F. Lechermann, and A. I. Lichtenstein. **General DFT++ method implemented with projector augmented waves: Electronic structure of $SrVO_3$ and the Mott Transition in $Ca_{2-x}Sr_xRuO_4$**. *Journal of Physics: Condensed Matter*, **23**(8):085601, 2011.

[260] B. Amadon, F. Lechermann, A. Georges, F. Jollet, T. O. Wehling, and A. I. Lichtenstein. **Plane-wave based electronic structure calculations for correlated materials using dynamical mean-field theory and projected local orbitals**. *Physical Review B*, **77**(20):205112, 2008.

[261] M. Jarrell and J. E. Gubernatis. **Bayesian inference and the analytic continuation of imaginary-time quantum Monte Carlo data**. *Physics Reports*, **269**(3):133–195, 1996.

[262] A. I. Lichtenstein, M. I. Katsnelson, and G. Kotliar. **Finite-Temperature Magnetism of Transition Metals: An ab initio Dy-**

namical Mean-Field Theory. *Physical Review Letters*, **87**(6):067205, 2001.

[263] B. Sachs, T. O. Wehling, K. S. Novoselov, A. I. Lichtenstein, and M. I. Katsnelson. **Ferromagnetic two-dimensional crystals: Single layers of K_2CuF_4**. *Physical Review B (Rapid Communications)*, **88**(20):201402, 2013.

[264] M. Hidaka, K. Inoue, I. Yamada, and P. J. Walker. **X-ray diffraction study of the crystal structures of K_2CuF_4 and $K_2Cu_xZn_{1-x}F_4$**. *Physica B+C*, **121**(3):343 – 350, 1983.

[265] K. Hirakawa and H. Ikeda. **Investigations of Two-Dimensional Ferromagnet K_2CuF_4 by Neutron Scattering**. *Journal of the Physical Society of Japan*, **35**(5):1328–1336, 1973.

[266] D. I. Khomskii and K. I. Kugel. **Orbital and magnetic structure of two-dimensional ferromagnets with Jahn-Teller ions**. *Solid State Communications*, **13**(7):763–766, 1973.

[267] V. Eyert and K.-H. Hock. **Electronic structure, itinerant magnetism and orbital ordering of K_2NiF_4-type compounds**. *Journal of Physics: Condensed Matter*, **5**(18):2987, 1993.

[268] N. I. Medvedeva, O. N. Mryasov, Y. N. Gornostyrev, D. L. Novikov, and A. J. Freeman. **First-principles total-energy calculations for planar shear and cleavage decohesion processes in B2-ordered NiAl and FeAl**. *Physical Review B*, **54**(19):13506, 1996.

[269] Z. Liu, J. Z. Liu, Y. Cheng, Z. Li, L. Wang, and Q. Zheng. **Interlayer binding energy of graphite: A mesoscopic determination from deformation**. *Physical Review B*, **85**(20):205418, 2012.

[270] L. Seixas, L. B. Abdalla, T. M. Schmidt, A. Fazzio, and R. H. Miwa. **Topological states ruled by stacking faults in Bi_2Se_3 and Bi_2Te_3**. *Journal of Applied Physics*, **113**(2):023705–023705, 2013.

[271] T. J. Booth, P. Blake, R. R. Nair, D. Jiang, E. W. Hill, U. Bangert, A. Bleloch, M. Gass, K. S. Novoselov, M. I. Kat-

snelson, et al. **Macroscopic graphene membranes and their extraordinary stiffness**. *Nano Letters*, **8**(8):2442–2446, 2008.

[272] M. Farle and K. Baberschke. **Ferromagnetic order and the critical exponent γ for a Gd monolayer: An electron-spin-resonance study**. *Physical Review Letters*, **58**(5):511, 1987.

[273] F. Huang, G. J. Mankey, M. T. Kief, and R. F. Willis. **Finite-size scaling behavior of ferromagnetic thin films**. *Journal of Applied Physics*, **73**(10):6760–6762, 1993.

[274] C. Waldfried, D. Welipitiya, T. McAvoy, P. A. Dowben, and E. Vescovo. **Finite size scaling in the thin film limit**. *Journal of Applied Physics*, **83**(11):7246–7248, 1998.

[275] N. D. Mermin and H. Wagner. **Absence of ferromagnetism or antiferromagnetism in one-or two-dimensional isotropic Heisenberg models**. *Physical Review Letters*, **17**(22):1133–1136, 1966.

[276] Y. Zhou, Z. Wang, P. Yang, X. Zu, L. Yang, X. Sun, and F. Gao. **Tensile Strain Switched Ferromagnetism in Layered NbS2 and NbSe2**. *ACS Nano*, **6**(11):9727–9736, 2012.

[277] H. Yamazaki, Y. Morishige, and M. Chikamatsu. **In-Plane Anisotropy of Ferromagnetic Resonance and Spin-Wave Relaxation in K_2CuF_4**. *Journal of the Physical Society of Japan*, **50**(9):2872–2875, 1981.

[278] V. Y. Irkhin and A. A. Katanin. **Kosterlitz-Thouless and magnetic transition temperatures in layered magnets with a weak easy-plane anisotropy**. *Physical Review B*, **60**(5):2990, 1999.

[279] M. I. Katsnelson, F. Guinea, and M. A. H. Vozmediano. **In-plane magnetic textures at the surface of topological insulators**. *EPL (Europhysics Letters)*, **104**(1):17001, 2013.

[280] K. Hirakawa. **Kosterlitz-Thouless transition in two-dimensional planar ferromagnet K_2CuF_4**. *Journal of Applied Physics*, **53**(3):1893–1898, 1982.

[281] R. S. Pease. **Crystal structure of boron nitride**. *Nature*, **165**(4201):722, 1950.

[282] F. Tran, R. Laskowski, P. Blaha, and K. Schwarz. **Performance on molecules, surfaces, and solids of the Wu-Cohen GGA exchange-correlation energy functional**. *Physical Review B*, **75**(11):115131, 2007.

[283] E. Erdogan, I. H. Popov, A. N. Enyashin, and G. Seifert. **Transport properties of MoS2 nanoribbons: edge priority**. *The European Physical Journal B*, **85**(1):1–4, 2012.

[284] L. Olesen, M. Brandbyge, M. R. Sørensen, K. W. Jacobsen, E. Lægsgaard, I. Stensgaard, and F. Besenbacher. **Apparent barrier height in scanning tunneling microscopy revisited**. *Physical Review Letters*, **76**(9):1485, 1996.

[285] J. J. W. M. Rosink, M. A. Blauw, L. J. Geerligs, E. van der Drift, and S. Radelaar. **Tunneling spectroscopy study and modeling of electron transport in small conjugated azomethine molecules**. *Physical Review B*, **62**(15):10459, 2000.

[286] S. L. Dudarev, G. A. Botton, S. Y. Savrasov, C. J. Humphreys, and A. P. Sutton. **Electron-energy-loss spectra and the structural stability of nickel oxide: An LSDA+U study**. *Physical Review B*, **57**(3):1505–1509, 1998.

[287] E. Bousquet and N. Spaldin. **J dependence in the LSDA+U treatment of noncollinear magnets**. *Physical Review B*, **82**(22):220402, 2010.

Glossary

ACFDT Adiabatic connection fluctuation-dissipation theorem

AIM Anderson impurity model

APW Augmented plane wave method

B3LYP 3-parameter hybrid functional by Becke, Lee, Yang, Parr

B88 GGA functional version by Becke (1988)

BCS theory Bardeen-Cooper-Schrieffer theory

CT-QMC Continuous-time quantum Monte Carlo

DF Density functional

DFT Density functional theory

DFT+U Density functional theory with Hubbard U correction

DFT++ Density functional theory combined with methods for correlation treatment

DFT-D Density functional theory with semi-empirical van der Waals correction

DMFT Dynamical mean-field theory

DOS Density of states

ED Exact diagonalization

Eq. Equation

Fig. Figure

GEA Generalized expansion approximation

GGA Generalized gradient approximation

GW A Green's function method

h-BN Hexagonal boron nitride

KKR Korringa-Krohn-Rostoker method

KS Kohn-Sham

LAPW Linearized augmented plane wave method

LCAO Linear combination of atomic orbitals

LDA Local density approximation

LDOS Local density of states

LMTO Linear muffin-tin orbital method

LSDA Local spin density approximation

PAW Projector augmented wave method

PBE-GGA GGA functional version by Perdew, Burke, Ernzerhof

PDE Partial differential equation

PW91-GGA GGA functional version by Perdew and Wang (1991)

QMC Quantum Monte Carlo

Ref. Reference

RPA Random phase approximation

rPBE-GGA GGA functional version revised by Perdew, Burke, Ernzerhof

STM Scanning tunneling microscopy

STS Scanning tunneling spectroscopy

TMDC Transition metal dichalcogenide

VASP Vienna *ab initio* Simulation Package

vdW Van der Waals

XAS X-ray absorption spectroscopy

XMCD X-ray magnetic circular dichroism

XPS X-ray photoelectron spectroscopy

Danksagung

Viele Leute haben zu dieser Arbeit beigetragen, denen ich hier im Folgenden danken möchte.

Prof. Alexander Lichtenstein möchte ich danken für das mir entgegengebrachte Vertrauen und die Möglichkeit, in seiner Arbeitsgruppe eine Doktorarbeit anzufertigen. Dabei habe ich durchgehend von der angenehmen Arbeitsatmosphäre und dem unkomplizierten Umgang miteinander profitiert. Sehr dankbar bin ich auch für die stets interessanten Projekte und die enge Zusammenarbeit mit Experimentatoren. Bedanken möchte ich mich auch für die Teilnahme an zahlreichen Konferenzen und internationalen Kooperationen während meiner Doktorandenzeit.

I am grateful to Prof. Mikhail Katsnelson for acting as the second referee of this thesis. Furthermore, I am very thankful for many projects he brought to Hamburg, lots of fruitful discussions, ideas, and his continuous input, which was crucial for the completion of this thesis.

Ein großer Dank geht auch nach Bremen an Prof. Tim Wehling für die enge Kooperation und die gemeinsame Zeit in Hamburg. Er hat ebenfalls durch das Anstoßen und Betreuen zahlreicher Projekte ermöglicht, dass diese Arbeit erfolgreich zu Ende gebracht werden konnte. Weiterhin danke ich für das Zweitgutachten meiner Disputation.

Bei Prof. Wiesendanger und insbesondere seinen Mitarbeitern Thomas Eelbo und Liudmila Dzemiantsova bedanke ich mich für die erfolgreichen Projekte rundum Nickel und Graphene. Ein Dankeschön auch der Kieler STM-Gruppe um Prof. Richard Berndt und Simon Altenburg für ein ebenfalls erfolgreiches STM-Projekt. Many thanks to Prof. Konstantin Novoselov for the fruitful collaboration on 2D ferromagnets and graphene/MoS_2 hybrids together with Liam Britnell and others.

Großer Dank an die gesamte Gruppe “th1-li” für das angenehme Arbeitsklima. Insbesondere sind meine (ehemaligen) Bürokollegen zu erwähnen. Michael Karolak gilt ein besonderer Dank für die gute Zeit im Raum 224, die Zusammenarbeit im Graphen/Ni-Projekt und für das Bereitstellen einiger Codes rund um DFT++ inklusive Einweisung und Betreuung. Ebenfalls danke ich Arthur Huber, Friedrich Krien und Malte Harland, die sich nahtlos eingefügt haben in die Riege netter Kollegen. Auch außerhalb des Büros war ich immer von angenehmen und hilfsbereiten Kollegen umgeben, zu nennen sind da Aljoscha Wilhelm, Masha Valentyuk, Igor Krivenko und Daniel Hirschmeier.

Nicht unerwähnt bleiben dürfen die Administratoren des PHYSnet, Bodo Krause-Kyora und Michael Vedmedenko, die mir stets freundlich und kompetent bei technischen Problemen und Schwierigkeiten zur Seite standen. Michael danke ich nochmals besonders für die unzähligen Arbeitsstunden, in denen er mir bei der Kompilation widerspenstiger Codes entscheidend

geholfen hat.

Meinen Studienkollegen und Freunden Cornelius Bausch, Edna Castillo, Jochen Kerbst, Christian Swoboda und Martin Waleczek danke ich für die schöne Zeit in der Jungiusstraße außerhalb des Büros.

Ein besonders großer Dank gilt meiner Familie, insbesondere meinen Eltern, meinem Bruder und meinen Großeltern für den fortwährenden Rückhalt und die Unterstützung.

Schließlich gilt mein größter Dank meiner Ehefrau Yu für die stetige liebevolle Unterstützung, die mich in meiner gesamten Zeit an der Universität begleitet hat.